A PRINCIPLE OF CORRESPONDING STATES FOR TWO-COMPONENT, SELF-GRAVITATING FLUIDS

R. Caimmi

Dipartimento di Astronomia, Università di Padova
Vicolo Osservatorio 2, I-35122 Padova, Italy

E–mail: *roberto.caimmi@unipd.it*

SUMMARY: Macrogases are defined as two-component, large-scale celestial objects where the subsystems interact only via gravitation. The macrogas equation of state is formulated and compared to the van der Waals (VDW) equation of state for ordinary gases. By analogy, it is assumed that real macroisothermal curves in macrogases occur as real isothermal curves in ordinary gases, where a phase transition (vapour-liquid observed in ordinary gases and gas-stars assumed in macrogases) takes place along a horizontal line in the macrovolume-macropressure $(O\mathcal{X}_V\mathcal{X}_p)$ plane. The intersections between real and theoretical (deduced from the equation of state) macroisothermal curves, make two regions of equal surface as for ordinary gases obeying the VDW equation of state. A numerical algorithm is developed for determining the following points of a selected theoretical macroisothermal curve on the $(O\mathcal{X}_V\mathcal{X}_p)$ plane: the three intersections with the related real macroisothermal curve, and the two extremum points (one maximum and one minimum). Different kinds of macrogases are studied in detail: UU, where U density profiles are flat, to be conceived as a simple guidance case; HH, where H density profiles obey the Hernquist (1990) law, which satisfactorily fits the observed spheroidal components of galaxies; HN/NH, where N density profiles obey the Navarro-Frenk-White (1995, 1996, 1997) law, which satisfactorily fits the simulated nonbaryonic dark matter haloes. A different trend is shown by theoretical macroisothermal curves on the $(O\mathcal{X}_V\mathcal{X}_p)$ plane, according to whether density profiles are sufficiently mild (UU) or sufficiently steep (HH, HN/NH). In the former alternative, no critical macroisothermal curve exists, below or above which the trend is monotonous. In the latter alternative, a critical macroisothermal curve exists, as shown by VDW gases, where the critical point may be defined as the horizontal inflexion point. In any case, by analogy with VDW gases, the first quadrant of the $(O\mathcal{X}_V\mathcal{X}_p)$ plane may be divided into three parts: (i) The G region, where only gas exists; (ii) The S region, where only stars exist; (iii) The GS region, where both gas and stars, exist. With regard to HH and HN/NH macrogases, an application is made to a subsample $(N = 16)$ of elliptical galaxies extracted from larger samples $(N = 25, \ N = 48)$ of early type galaxies investigated within the SAURON project (Cappellari et al. 2006, 2007). Under the simplifying assumption of universal mass ratio of the two subsystems, m, different models characterized by different scaled truncation radii, i.e. concentrations, Ξ_i, Ξ_j, are considered and the related position of sample objects on the $(O\mathcal{X}_V\mathcal{X}_p)$ plane is determined. Macrogases fitting to elliptical galaxies are expected to lie within the S region or slightly outside the boundary between the S and the GS region at most. Accordingly, models where sample objects lie outside the S region and far from its boundary, or cannot be positioned on the $(O\mathcal{X}_V\mathcal{X}_p)$ plane, are rejected. For each macrogas, twenty models are considered for different values of (Ξ_i, Ξ_j, m), namely $\Xi_i, \Xi_j = 5, \ 10, \ 20, \ +\infty$ $(\Xi_i, \Xi_j,$ both either finite or infinite), and $m = 10, \ 20$. Acceptable models are $(10, 10, 20), (10, 20, 20), (20, 10, 20),$ $(20, 20, 20),$ for HH macrogases, and $(10, 5, 10), (10, 10, 20), (20, 10, 20),$ for HN/NH macrogases. Tipically, fast rotators are found to lie within the S region, while slow rotators are close (from both sides) to the boundary between the S and the GS region. The net effect of the uncertainty affecting observed quantities, on the position of sample objects on the $(O\mathcal{X}_V\mathcal{X}_p)$ plane, is also investigated. Finally, a principle of corresponding states is formulated for macrogases with assigned density profiles and scaled truncation radii.

Key words. Galaxies: evolution – Galaxies: halos – dark matter

19

1. INTRODUCTION

Tidal interactions between neighbouring objects span across the whole admissible range of lenghts in nature: from, say, atoms to cluster of galaxies i.e. from micro to macrocosmos. The role of tidal interactions is of basic importance in driving a wide variety of physical phenomena. In dealing with microcosmos, tidal forces between molecules are responsible for the occurrence of the liquid and solid phase, and the presence of a triple point where the gas, liquid, and solid phase coexist, for an assigned homogeneous substance (e.g. Landau and Lifchitz 1967, Chaps. VII-VIII, hereafter quoted as LL67). In dealing with ordinary cosmos, the tidal action of a white dwarf star on a sufficiently close (filling the whole volume enclosed by the Roche equipotential surface) red giant companion, makes mass transfer into the white dwarf until a critical mass is attained and the star ends its life into a catastrophic SnIa supernova explosion (e.g. Burrows 2000). In dealing with macrocosmos, the tidal action induced by massive haloes on hosted galaxies affects their formation and evolution process, due to a larger depth of the potential well, resulting in a different correlation of observables with respect to galaxies in absence of massive halos (e.g. D'Onofrio et al. 2006).

Ordinary fluids are collisional, which makes the stress tensor isotropic and the velocity distribution to obey the Maxwell law. Tidal interactions therein act between colliding particles (e.g. LL67, Chap. VII, §74). Astrophysical fluids (leaving aside extremely dense environments such as galactic nuclei) are collisionless, which makes the stress tensor anisotropic and the velocity distribution do not obey the Maxwell law. Tidal interactions therein act between a single particle and the system as a whole.

Given that tidal interactions are at work in both collisional and collisionless fluids, the existence of an analogy between the two may be the subject of a legitimate question. To this respect, an investigation must necessarily be restricted to theoretical considerations, as astrophysical fluids (conceived as macrogases) cannot be tested in laboratory. More specifically, a macrogas equation of state has to be formulated in terms of three variables (macrovolume, macropressure, macrotemperature), and the related macroisothermal curves (i.e. the macropressure as a function of the macrovolume for selected constant macrotemperatures) has to be compared with their counterparts deduced from the van der Waals (hereafter quoted as VDW) equation of state for ordinary gases. If some analogy exists, it can be extended to (undetectable) real macroisothermal curves as a working hypothesis. Finally, an application can be made to galaxies or clusters of galaxies.

The VDW equation of state can be expressed in (dimensionless) reduced volume, reduced pressure, and reduced temperature. Similarly to the Lane-Emden equation for polytropes (e.g. Chandrasekhar 1939, Chap. IV, §4; Caimmi 1986), the reduced VDW

equation holds for a class of fluids instead of a single fluid. In general, the states of two systems with equal values of the reduced variables, are defined as corresponding states. According to the principle of corresponding states, two fluids which obey the reduced VDW equation of state and exhibit equal values of two among three reduced variables, necessarily exhibit equal values of the remaining reduced variable. For further details refer to classical textbooks (e.g. LL67, Chap. VIII, §85).

In the light of an analogy between ordinary gases and macrogases, the formulation of a principle of corresponding states in the latter case could be highly rewarding. A macrogas equation of state was formulated in earlier attempts (Caimmi and Secco 1990, hereafter quoted as CS90, Caimmi and Valentinuzzi 2008, hereafter quoted as CV08), where the analogy between macrogases and VDW gases was only mentioned, and isofractional mass ($m = $ const) curves were plotted for a few selected density profiles. The current paper aims to establish a closer analogy, where the macrovolume is related to the fractional radius, y, the macropressure to the fractional mass, m, and the macrotemperature to the fractional energy, ϕ. The basic assumptions and the formalism remain unchanged with respect to the last parent paper (CV08).

The present investigation is mainly devoted to the following points: (i) Expression of an equation of state for two-component astrophysical fluids, conceived as macrogases; (ii) Comparison between macroisothermal curves and isothermal curves related to VDW gases, with regard to a simple guidance case and two cases which satisfactorily fit to observations or simulations; (iii) Application to a subsample ($N = 16$) of elliptical galaxies (CV08), extracted from larger samples ($N = 25$, $N = 48$) of early-type galaxies investigated within the SAURON project (Cappellari et al. 2006, 2007, hereafter quoted as S IV, S X, respectively).

The work is organized as follows: The equation of state of ideal and VDW gases are reviewed, and related isothermal curves are shown, in Section 2. A macrogas equation of state is formulated in terms of macrovolume, macropressure, macrotemperature, and related macroisothermal curves are shown for flat and steep density profiles, in Section 3. An application to elliptical galaxies for which masses, radii, and rms velocities can be determined, is performed in Section 4 where the selection of acceptable models is made and an interpretation of the results is outlined. The conclusion is drawn in Section 5. Further details on two specific points are reported in the Appendix.

2. ORDINARY FLUIDS[1]

Let ordinary fluids be conceived as fluids where the effects of gravitation on the equation of state may safely be neglected e.g. on the surface of the Earth. The simplest description is provided by the theory of ideal gas.

---

[1]A more extended version of this Section can be found on the arxiv site, at arxiv:0907.1018.

The equation of state of ideal gases may be written under the form (e.g. LL67, Chap. IV, §42):

$$pV = kNT \quad ; \qquad (1)$$

where p is the pressure, V the volume, T the temperature, N the particle number, and k the Boltzmann constant. The product, pV, has the dimensions of an energy and, in fact, the mean kinetic energy per degree of freedom equals the product, $(1/2)kNT$, and the mean kinetic energy of motions along the X_{p} axis reads:

$$\overline{(E_{\mathrm{kin}})_{pp}} = \frac{1}{2}N\overline{m}\sigma_{pp}^2 = \frac{1}{2}kNT \quad ; \qquad (2a)$$

$$\overline{m}\sigma_{pp}^2 = kT \quad ; \qquad (2b)$$

where $\overline{m}$ is the mean particle mass and σ_{pp} the rms velocity component along the X_{p} axis. In the light of the theory of ideal gases, Eqs. (1) and (2) disclose the meaning of the Boltzmann constant: for fixed pressure, volume, and particle number, the mean kinetic energy remains unchanged, regardless of the nature of the gas.

In getting a better description of real gases, the interactions between particles are taken into consideration. The VDW generalization of the equation of state of ideal gases, Eq. (1), reads (van der Waals 1873):

$$\left(p + A\frac{N^2}{V^2}\right)(V - NB) = kNT \quad ; \qquad (3)$$

where A and B are constants which depend on the nature of the particles. For further details refer to specific textbooks (e.g. LL67, Chap. VII, §74).

The isothermal ($T = \mathrm{const}$) curves for ideal gases are hyperbolas with axes, $p = \mp V$, conformly to Eq. (1). In VDW theory of real gases, the isothermal curves exhibit two extremum points, which reduce to a single horizontal inflexion point when a critical temperature is attained, as shown in Fig. 1.
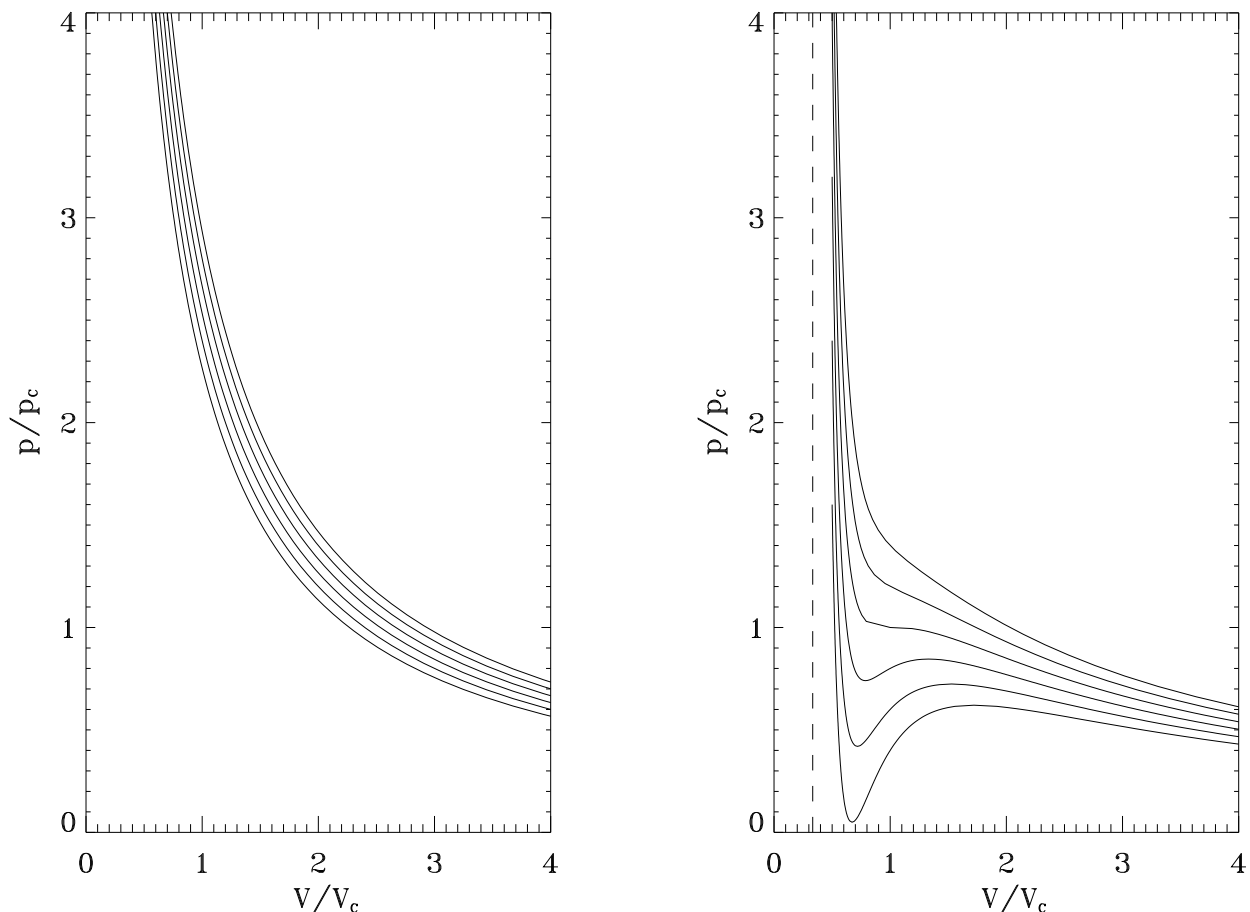

Fig. 1. *Isothermal curves related to ideal (left panel) and VDW (right panel) gases, respectively. Isothermal curves (from bottom to top) correspond to $T/T_{\mathrm{c}} = 0.85$, 0.90, 0.95, 1.00, 1.05, 1.10. No extremum point exists above the critical isothermal curve, $T/T_{\mathrm{c}} = 1$.*
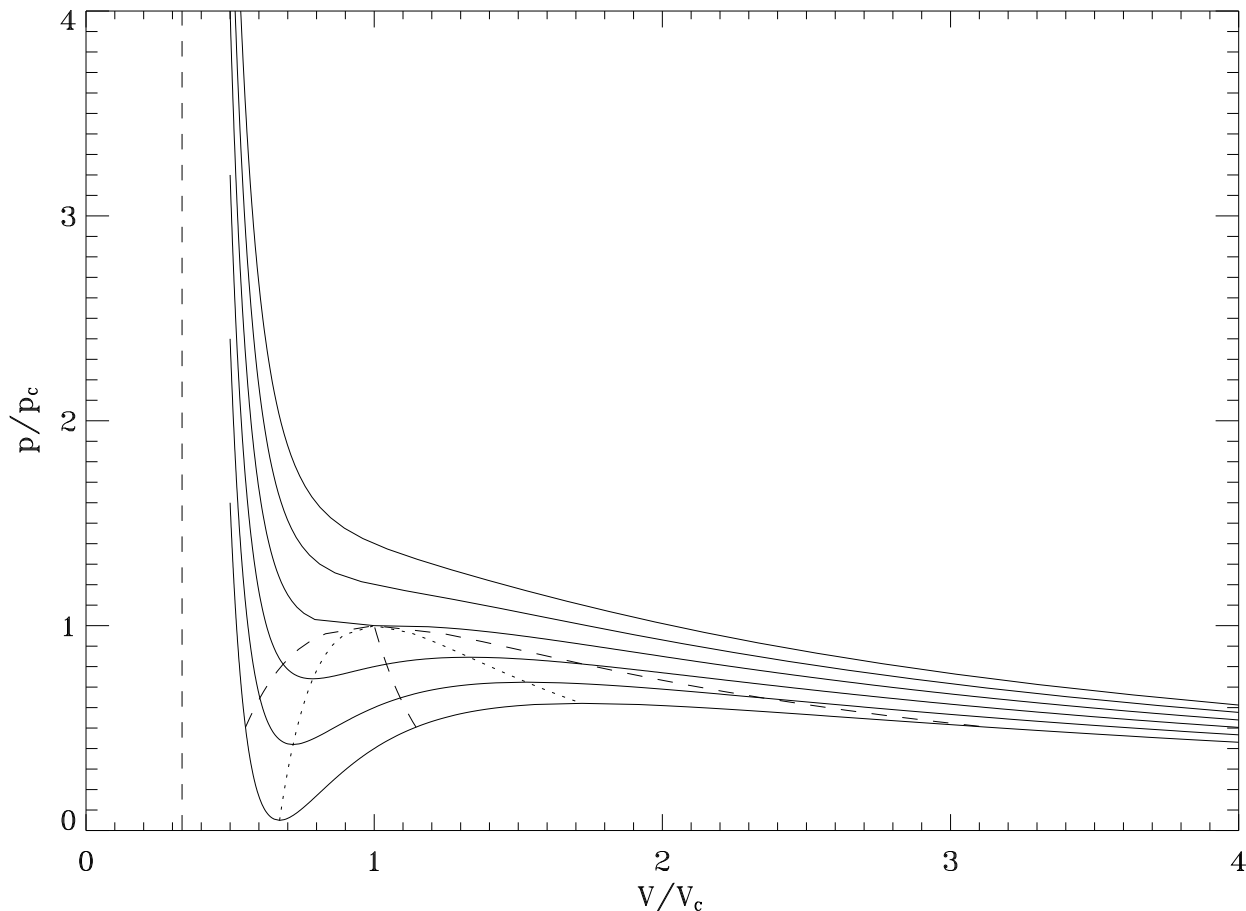
Fig. 2. *Same as in Fig. 1 (right panel), where the occurrence (within the bell-shaped area bounded by the dashed curve) of saturated vapour is considered. The dashed curve (including the central branch) is the locus of intersection between VDW and real isothermal curves, the latter being related to constant pressure where liquid and vapour phases coexist. The dotted curve is the locus of VDW isothermal extremum points. For further details refer to the text.*

Well above the critical isothermal curve, $T \gg T_c$, the trends exhibited by ideal and VDW gases look very similar. Below the critical isothermal curve, $T < T_c$, the behaviour of VDW gases is different with respect to ideal gases and, in addition, the related isothermal curves provide a wrong description within a specific region where saturated vapour and liquid phases coexist. Further details are shown in Fig. 2.

Above the critical isothermal curve ($T = T_c$) the trend is similar with respect to ideal gases. Below the critical isothermal curve and on the right of the dashed curve, the supersaturated vapour still behaves as an ideal gas. Below the critical isothermal curve and on the left of the dashed curve, the liquid shows little change in volume as the pressure

rises. Within the bell-shaped area bounded by the dashed curve, the liquid phase is in equilibrium with the saturated vapour phase. A reduced volume implies smaller saturated vapour fraction and larger liquid fraction at constant pressure, and vice versa. The VDW equation of state is no longer valid in this region. The dashed curve (including the central branch) is the locus of intersections between VDW and real isothermal curves, the latter being related to constant pressure where liquid and vapour phases coexist. The dotted curve is the locus of VDW isothermal extremum points.

A specific ($T/T_c = 0.85$) VDW and corresponding real isothermal curve, are represented in Fig. 3.
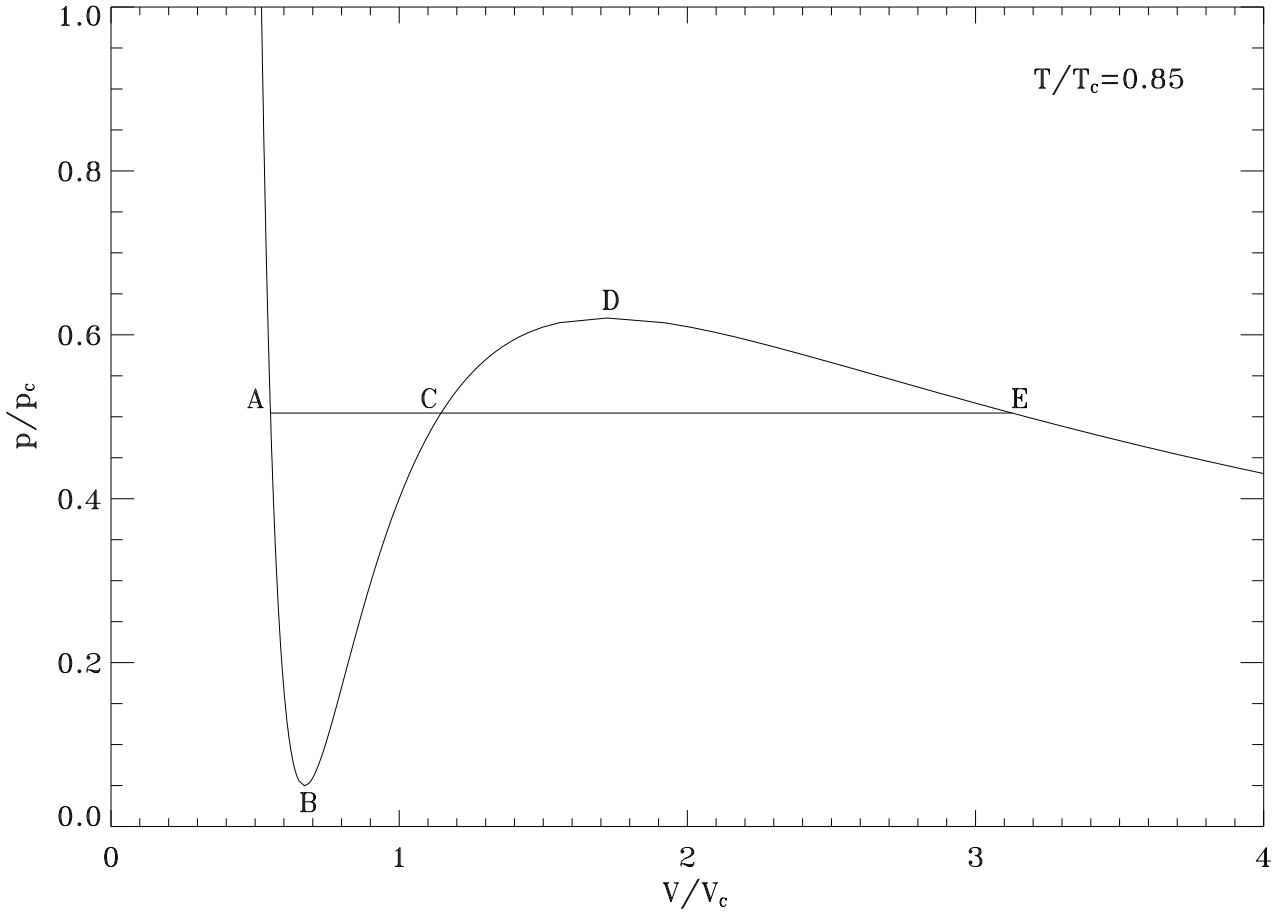
Fig. 3. *A specific* $(T/T_{\rm c} = 0.85)$ *VDW and corresponding real isothermal curve. The above mentioned curves coincide within the range* $V \leq V_{\rm A}$ *and* $V \geq V_{\rm E}$. *The regions* ABC *and* CDE *have equal area. For further details refer to the text.*

The VDW isothermal curve and the real isothermal curve coincide within the range $V \leq V_{\rm A}$ and $V \geq V_{\rm E}$. The VDW isothermal curve exhibits two extremum points: a minimum, B, and a maximum, D, while the real isothermal curve is flat, within the range, $V_{\rm A} \leq V \leq V_{\rm E}$. Configurations related to the VDW isothermal curve within the ranges $V_{\rm A} \leq V \leq V_{\rm B}$ (due to tension forces acting on the particles yielding superheated liquid) and $V_{\rm D} \leq V \leq V_{\rm E}$ (due to the occurrence of undercooled vapour), may be obtained under special conditions, while configurations within the range $V_{\rm B} \leq V \leq V_{\rm D}$ are always unstable. The volumes $V_{\rm A}$ and $V_{\rm E}$ correspond to the maximum value in presence of the sole liquid phase and the minimum value in presence of the sole vapour phase, respectively.

The surfaces ABC and CDE are equal, as first inferred by Maxwell (e.g. Rostagni 1957, Chap. XII, §19). For further details refer to specific textbooks (e.g. LL67, Chap. VIII, §85).

In order to simplify both notation and calculations, it is convenient to deal with (dimensionless) re-

duced variables (e.g. Rostagni 1957, Chap. XII, §16; LL67, Chap. VIII, §85). To this aim, the first step is the knowledge of the parameters related to the critical point $(V_{\rm c}, p_{\rm c}, T_{\rm c})$ which may be determined as the solution of a system of three equations, namely the VDW equation particularized to the critical point, $(\partial p/\partial V)_{V_{\rm c}, T_{\rm c}} = 0$, and $(\partial^2 p/\partial V^2)_{V_{\rm c}, T_{\rm c}} = 0$, keeping in mind that the critical point is a horizontal inflexion point. The result is:

$$V_{\rm c} = 3NB \quad , \tag{4}$$

$$T_{\rm c} = \frac{8}{27} \frac{A}{B} \frac{1}{k} \quad , \tag{5}$$

$$p_{\rm c} = \frac{1}{27} \frac{A}{B^2} \quad , \tag{6}$$

$$Z_c = \frac{p_{\rm c} V_{\rm c}}{kNT_{\rm c}} = \frac{3}{8} \quad , \tag{7}$$

where, in general, the compressibility factor $Z = pV/(kNT)$ defines the degree of departure from the behaviour of ideal gases, for which $Z = 1$ according

23

to Eq. (1). For further details refer to specific textbooks (e.g. Rostagni 1957, Chap. XII, §20; LL67, Chap. VIII, §85).

With regard to the reduced variables:

$$\mathcal{V} = \frac{V}{V_c} \quad , \qquad \mathcal{p} = \frac{p}{p_c} \quad , \qquad \mathcal{T} = \frac{T}{T_c} \quad , \quad (8)$$

the ideal gas equation of state, Eq. (1), and the VDW equation of state, Eq. (3), read:

$$\mathcal{p}\mathcal{V} = \frac{8}{3}\mathcal{T} \quad , \tag{9}$$

$$\left(\mathcal{p} + \frac{3}{\mathcal{V}^2}\right)\left(\mathcal{V} - \frac{1}{3}\right) = \frac{8}{3}\mathcal{T} \quad , \qquad \mathcal{V} > \frac{1}{3} \quad , \tag{10}$$

and a further analysis of the third-degree equation in $\mathcal{V}$, associated to $(\partial \mathcal{p}/\partial \mathcal{V})_{\mathcal{V},\mathcal{T}} = 0$, shows that, in general, the extremum points of VDW isothermal curves ($\mathcal{T} \leq 1$) occur at $\mathcal{V} = \mathcal{V}_B$ (minimum) and $\mathcal{V} = \mathcal{V}_D$ (maximum), $\mathcal{V}_B \leq \mathcal{V}_D$. As $\mathcal{T} \to 0$, $\mathcal{V}_B \to 1/3$, $\mathcal{V}_D \to +\infty$, where, in all cases, $1/3 < \mathcal{V}_B \leq 1 \leq \mathcal{V}_D$.

The two areas defined by the intersection of a generic VDW isothermal curve ($\mathcal{T} \leq 1$) and related real isothermal curves (see Fig. 3), are expressed as:

$$W_1 = \int_{V_A}^{V_C} p_C \, dV - \int_{V_A}^{V_C} p \, dV$$

$$= p_C V_C \left[\mathcal{p}_C(\mathcal{V}_C - \mathcal{V}_A) - \int_{\mathcal{V}_A}^{\mathcal{V}_C} \mathcal{p} \, d\mathcal{V} \right] , \quad (11a)$$

$$W_2 = \int_{V_C}^{V_E} p \, dV - \int_{V_C}^{V_E} p_C \, dV$$

$$= p_C V_C \left[\int_{\mathcal{V}_C}^{\mathcal{V}_E} \mathcal{p} \, d\mathcal{V} - \mathcal{p}_C(\mathcal{V}_E - \mathcal{V}_C) \right] , \quad (11b)$$

and the substitution of Eq. (10) into Eq. (11) allows explicit expressions for the integrals. The result is:

$$\frac{W_1}{p_C V_C} = \mathcal{p}_C(\mathcal{V}_C - \mathcal{V}_A) - \frac{8}{3}\mathcal{T} \ln \frac{3\mathcal{V}_C - 1}{3\mathcal{V}_A - 1}$$
$$+ \frac{3(\mathcal{V}_C - \mathcal{V}_A)}{\mathcal{V}_A \mathcal{V}_C} \quad , \tag{12a}$$

$$\frac{W_2}{p_C V_C} = \frac{8}{3}\mathcal{T} \ln \frac{3\mathcal{V}_E - 1}{3\mathcal{V}_C - 1} - \frac{3(\mathcal{V}_E - \mathcal{V}_C)}{\mathcal{V}_C \mathcal{V}_E}$$
$$- \mathcal{p}_C(\mathcal{V}_E - \mathcal{V}_C) \quad , \tag{12b}$$

and the condition $W_1 = W_2$ after some algebra reads:

$$\mathcal{p}_C = \frac{8}{3}\frac{\mathcal{T}}{\mathcal{V}_E - \mathcal{V}_A} \ln \frac{3\mathcal{V}_E - 1}{3\mathcal{V}_A - 1} - \frac{3}{\mathcal{V}_A \mathcal{V}_E} \tag{13}$$

where, for a selected isothermal curve, the unknowns are $\mathcal{p}_C = \mathcal{p}_A = \mathcal{p}_E$, $\mathcal{V}_A$, and $\mathcal{V}_E$.

The reduced volumes, $\mathcal{V}_A$, $\mathcal{V}_C$, $\mathcal{V}_E$, see Fig. 3, may be considered as intersections between a VDW isothermal curve ($\mathcal{T} < 1$) and a horizontal straight line $\mathcal{p} = \mathcal{p}_C$ in the $(O\mathcal{V}\mathcal{p})$ plane. In other words, $\mathcal{V}_A$, $\mathcal{V}_C$, $\mathcal{V}_E$, are the real solutions of the third-degree equation:

$$\mathcal{V}^3 - \left(\frac{1}{3} + \frac{8}{3}\frac{\mathcal{T}}{\mathcal{p}_C}\right)\mathcal{V}^2 + \frac{3}{\mathcal{p}_C}\mathcal{V} - \frac{1}{\mathcal{p}_C} = 0 \tag{14}$$

which has been deduced from Eq. (10) particularized to $\mathcal{p} = \mathcal{p}_C$. The last unknown, $\mathcal{p}_C$, is determined from Eq. (13).

An inspection of Fig. 3 shows that the points A and E are located on the left of the minimum B and on the right of the maximum D, respectively. Keeping in mind the above results, the following inequality holds: $\mathcal{V}_A \leq \mathcal{V}_B \leq 1 \leq \mathcal{V}_D \leq \mathcal{V}_E$, which implies further investigation on the special case $\mathcal{V}_C = 1$.

It can be seen that the abscissa of the intersection point C between a selected VDW isothermal curve and related real isothermal curve (see Fig. 3) cannot occur at $\mathcal{V}_C = 1$ unless the critical isothermal curve is considered. Then, the third-degree equation Eq. (14) must be solved in the general case.

The locus of the intersections between VDW and real isothermal curves is represented in Fig. 2 as a trifid curve, where the left, the right, and the middle branch correspond to $\mathcal{V}_A$, $\mathcal{V}_E$, and $\mathcal{V}_C$, respectively. The common starting point coincides with the critical point. The locus of the VDW isothermal curve extremum points is represented in Fig. 2 as a dotted curve starting from the critical point where the left and the right branch correspond to minimum and maximum points, respectively.

A fluid state can be represented in reduced variables as ($\mathcal{V}$, $\mathcal{p}$, $\mathcal{T}$), where one variable may be expressed as a function of the remaining two, by use of the reduced ideal gas equation of state, Eq. (9), or the reduced VDW equation of state, Eq. (10). The formulation in terms of reduced variables, Eqs. (8), makes the related equation of state universal i.e. it holds for any fluid. Similarly, the Lane-Emden equation expressed in polytropic (dimensionless) variables, describes the whole class of polytropic gas spheres with assigned polytropic index, in hydrostatic equilibrium (e.g. Chandrasekhar 1939, Chap. IV, §4).

The states of two fluids with the same ($\mathcal{V}$, $\mathcal{p}$, $\mathcal{T}$) are defined as corresponding states. The mere existence of an equation of state yields the following result:

Law of corresponding states. Given two fluids, the equality between two out of three reduced variables $\mathcal{V}$, $\mathcal{p}$, $\mathcal{T}$ implies the equality between the remaining related reduced variables i.e. the two fluids are in corresponding states.

The law was first formulated by van der Waals in 1880. For further details refer to specific textbooks (e.g. LL67, Chap. VIII, §85).

3. ASTROPHYSICAL FLUIDS

Let macrogases be defined as two-component fluids that interact only gravitationally. The virial theorem for subsystems reads (Caimmi et al. 1984, Caimmi and Secco 1992, CV08):

$$2(E_u)_{\rm kin} + (E_{uv})_{\rm vir} = 0 \ , \quad u = i, j \ , \quad v = j, i \ , \ (15{\rm a})$$

$$(E_{uv})_{\rm vir} = (E_u)_{\rm sel} + (E_{uv})_{\rm tid} \ , \tag{15b}$$

where i and j denote the inner and outer subsystem, respectively, $E_{\rm kin}$ is the kinetic energy, $E_{\rm sel}$, $E_{\rm tid}$, and $E_{\rm vir}$, are the self, tidal, and virial potential energy respectively. The related definitions are:

$$(E_u)_{\rm kin} = \frac{1}{2} \int_{S_u} \rho_u(x_1, x_2, x_3) \sum_{s=1}^{3} (v_u)_s^2 \, d^3 S_u \ , \ (16)$$

$$(E_u)_{\rm sel} = \int_{S_u} \rho_u(x_1, x_2, x_3) \sum_{s=1}^{3} x_s \frac{\partial \mathcal{V}_u}{\partial x_s} \, d^3 S_u$$

$$= -\frac{1}{2} \int_{S_u} \rho_u(x_1, x_2, x_3) \mathcal{V}_u(x_1, x_2, x_3) \, d^3 S_u \ , \tag{17}$$

$$(E_{uv})_{\rm tid} = \int_{S_u} \rho_u(x_1, x_2, x_3) \sum_{s=1}^{3} x_s \frac{\partial \mathcal{V}_v}{\partial x_s} \, d^3 S_u \ , \ (18)$$

where ρ is the density, v_s is the velocity component, S is the volume, and $\mathcal{V}$ is the gravitational potential.

The virial theorem makes a necessary (but not sufficient) condition for dynamical or hydrostatic equilibrium, which implies that the parameters of the virialized configuration must be considered as averaged over a sufficiently long time. For further details refer to specific textbooks (e.g. Landau and Lifchitz 1966, Chap. II, §10) and to an earlier paper (Caimmi 2007). On the other hand, general trends exhibited by virialized configurations hold, in particular, for self-consistent density profiles implying nonnegative distribution functions. Accordingly, density profiles shall be chosen regardless of their self-consistency, aiming to investigate general trends instead of local properties. To avoid the determination of the gravitational potential, which is the most difficult step towards an explicit formulation of potential energies, future considerations shall be restricted to homeoidally striated ellipsoids (Roberts 1962). The following results are taken from earlier attempts (CV08, and further references therein), to which an interested reader is addressed to.

The isopycnic (i.e. constant density) surfaces are defined by the following law:

$$\rho_u = \rho_u^\dagger f_u(\xi_u) \ , \quad f_u(1) = 1 \ , \quad u = i, j \ , \tag{19a}$$

$$\xi_u = \frac{r_u}{r_u^\dagger} \ , \quad 0 \le \xi_u \le \Xi_u \ , \quad \Xi_u = \frac{R_u}{r_u^\dagger} \ , \tag{19b}$$

where the dagger denotes a selected reference isopycnic surface, r is the radial coordinate along a selected direction, R is the related truncation radius, ξ is a related scaled radial coordinate, and Ξ is the related scaled truncation radius.

The mass and the self potential energy read:

$$M_u = (\nu_u)_{\rm mas} M_u^\dagger \ , \tag{20a}$$

$$M_u^\dagger = \frac{4\pi}{3} \rho_u^\dagger (a_u)_1^\dagger (a_u)_2^\dagger (a_u)_3^\dagger \ , \tag{20b}$$

$$(\nu_u)_{\rm mas} = \frac{3}{2} \int_0^{\Xi_u} F_u(\xi_u) \, d\xi_u \ , \tag{20c}$$

$$F_u(\xi_u) = 2 \int_{\xi_u}^{\Xi_u} f_u(\xi_u) \xi_u \, d\xi_u \ , \tag{20d}$$

$$(E_u)_{\rm sel} = -(\nu_u)_{\rm sel} \frac{G(M_u^\dagger)^2}{(a_u^\dagger)_1} B_u \ , \tag{21a}$$

$$(\nu_u)_{\rm sel} = \frac{9}{16} \int_0^{\Xi_u} F_u^2(\xi_u) \, d\xi_u \ , \tag{21b}$$

where $a_\ell^\dagger$ are semiaxes of the reference isopycnic surface, $\nu_{\rm mas}$ and $\nu_{\rm sel}$ are profile factors which depend only on the mass distribution, and B is a shape factor. For homogeneous configurations, $\nu_{\rm mas} = \Xi^3$ and $\nu_{\rm sel} = (3/10)\,\Xi^5$. For spherical shapes, $B = 2$.

Under the further restriction of similar and similarly placed boundaries, the following relations hold:

$$\xi_i = y^\dagger \xi_j \ , \quad \frac{\Xi_j}{\Xi_i} = \frac{y}{y^\dagger} \ , \quad \frac{(\nu_j)_{\rm mas}}{(\nu_i)_{\rm mas}} = \frac{m}{m^\dagger} \ , \tag{22a}$$

$$y = \frac{R_j}{R_i} \ , \quad y^\dagger = \frac{r_j^\dagger}{r_i^\dagger} \ , \quad m = \frac{M_j}{M_i} \ , \quad m^\dagger = \frac{M_j^\dagger}{M_i^\dagger} \ , (22{\rm b})$$

which makes tidal and virial potential energy reduce to:

$$(E_{uv})_{\rm xxx} = -\frac{G(M_u^\dagger)^2}{(a_u^\dagger)_1} (\nu_{uv})_{\rm xxx} B \ , \tag{23a}$$

$$u = i, j \ , \quad v = j, i \ , \quad {\rm xxx} = {\rm tid, vir} \ , \tag{23b}$$

and the explicit expressions of the profile factors read:

$$(\nu_{ij})_{\rm tid} = -\frac{9}{8} m^\dagger w^{\rm (ext)}(\eta) \ , \tag{24a}$$

$$(\nu_{ji})_{\rm tid} = -\frac{9}{8} \frac{y^\dagger}{m^\dagger} w^{\rm (int)}(\eta) \ , \tag{24b}$$

$$(\nu_{uv})_{\rm vir} = (\nu_u)_{\rm sel} + (\nu_{uv})_{\rm tid} \ , \tag{24c}$$

$$\eta = \frac{\Xi_i}{y^\dagger} = \frac{\Xi_j}{y} \ , \qquad y \ge 1 \ , \tag{24d}$$

where $u = i, j$; $v = j, i$; and the functions $w^{\rm (int)}$ $w^{\rm (ext)}$ are defined as:

$$w^{\rm (int)}(\eta) = \int_0^\eta F_j(\xi_j) \frac{dF_i}{d\xi_j} \xi_j \, d\xi_j \ , \tag{25a}$$

$$w^{\rm (ext)}(\eta) = \int_0^\eta F_i(\xi_i) \frac{dF_j}{d\xi_j} \xi_j \, d\xi_j \ . \tag{25b}$$

For further details refer to Appendix A1. In conclusion, Eqs. (19)-(25) allow the calculation of the virial potential energy for homeoidally striated ellipsoids related to similar and similarly placed boundaries.

The fractional virial potential energy reads:

$$\phi = \frac{(E_{ji})_{\text{vir}}}{(E_{ij})_{\text{vir}}} = \frac{(m^\dagger)^2}{y^\dagger} \frac{(\nu_{ji})_{\text{vir}}}{(\nu_{ij})_{\text{vir}}}$$

$$= \frac{m^2}{y} \frac{\Xi_j}{\Xi_i} \left[\frac{(\nu_i)_{\text{mas}}}{(\nu_j)_{\text{mas}}}\right]^2 \frac{(\nu_{ji})_{\text{vir}}}{(\nu_{ij})_{\text{vir}}} \ , (26)$$

which, for assigned density profiles, depends on either the reference fractional mass $m^\dagger$ and the fractional scaling radius $y^\dagger$ or the fractional mass m and the fractional truncation radius y.

Strictly speaking, Eq. (26) is valid provided the indices i and j denote the embedded and the embedding subsystem respectively, which implies $y \geq 1$. If the role of the two subsystems is reversed, $0 \leq y \leq 1$, it has to be kept in mind that the inner and the outer component are denoted by the indices j and i respectively. Then, the quantities of interest must be calculated according to substitutions, $m \to m^{-1}$, $m^\dagger \to (m^\dagger)^{-1}$, $y \to y^{-1}$, $y^\dagger \to (y^\dagger)^{-1}$, $i \leftrightarrow j$, which yields $\phi = (E_{ij})_{vir}/(E_{ji})_{\text{vir}}$ in the domain $y \geq 1$. Following the above mentioned procedure where, in addition, $\phi \to \phi^{-1}$, allows the explicit expression of the fractional virial energy, $\phi = (E_{ji})_{\text{vir}}/(E_{ij})_{\text{vir}}$, in the domain $0 \leq y \leq 1$ which extends the whole domain to $0 \leq y < +\infty$.

In absence of truncation radius, $\Xi \to +\infty$, $\eta \to +\infty$, the reversion occurs when the density drops to zero and nothing changes except in infinitesimal terms of higher order and infinite terms of lower order. Accordingly, there is no need to perform the reversion in this case.

The combination of Eq. (24) and Eq. (26) yields:

$$\phi = \frac{(m^\dagger)^2}{y^\dagger} \frac{(\nu_j)_{\text{sel}} - \frac{9}{8}\frac{y^\dagger}{m^\dagger}w^{(\text{int})}(\eta)}{(\nu_i)_{\text{sel}} - \frac{9}{8}m^\dagger w^{(\text{ext})}(\eta)} \ , \qquad (27a)$$

$$\phi = \frac{\Xi_j}{\Xi_i}\left[\frac{(\nu_i)_{\text{mas}}}{(\nu_j)_{\text{mas}}}\right]^2 \frac{m^2}{y}$$

$$\times \frac{(\nu_j)_{\text{sel}} - \frac{9}{8}\frac{\Xi_i}{\Xi_j}\frac{(\nu_j)_{\text{mas}}}{(\nu_i)_{\text{mas}}}\frac{y}{m}w^{(\text{int})}(\eta)}{(\nu_i)_{\text{sel}} - \frac{9}{8}\frac{(\nu_i)_{\text{mas}}}{(\nu_j)_{\text{mas}}}m w^{(\text{ext})}(\eta)} \ ; (27b)$$

where, for assigned scaled truncation radii Ξ_i and Ξ_j, the independent variables are $m^\dagger$, $y^\dagger$, or m, y. In terms of a second-degree equation in $m^\dagger$ or m, Eqs. (27) read:

$$\hat{A}x^2 + \hat{B}x + \hat{C} = 0 \ , \qquad (28a)$$

$$\hat{A} = k_A(\nu_j)_{\text{sel}} \ ; \ k_A = 1, \ \frac{\Xi_j}{\Xi_i}\left[\frac{(\nu_i)_{\text{mas}}}{(\nu_j)_{\text{mas}}}\right]^2 \ , \ (28b)$$

$$\hat{B} = -\frac{9}{8}k_B\left[w^{(\text{int})}(\eta) - \phi w^{(\text{ext})}(\eta)\right] \ ,$$

$$k_B = y^\dagger, \ \frac{(\nu_i)_{\text{mas}}}{(\nu_j)_{\text{mas}}}y \ , \qquad (28c)$$

$$\hat{C} = -k_C(\nu_i)_{\text{sel}}\phi \ , \qquad k_C = y^\dagger, \ y \ , \qquad (28d)$$

where the positive solution is:

$$x = \frac{\sqrt{\hat{B}^2 - 4\hat{A}\hat{C}} - \hat{B}}{2\hat{A}} \ ; \qquad x = m^\dagger, \ m \ , \quad (29)$$

while the negative solution has been disregarded due to the lack of physical meaning.

In the special case of coinciding density profiles, $f_i = f_j$, $F_i = F_j$, and scaled truncation radii, $\Xi_i = \Xi_j$, fractional masses and truncation radii also coincide, $m^\dagger = m$, $y^\dagger = y$, via Eqs. (22), and the same holds for the profile factors $(\nu_i)_{\text{mas}} = (\nu_j)_{\text{mas}}$, $(\nu_i)_{\text{sel}} = (\nu_j)_{\text{sel}}$, which depend on the scaled truncation radii. Accordingly, Eqs. (27a), (27b) also coincide.

To get a closer analogy with real gases, let Eqs. (27) be rewritten after a change of variables, as:

$$X_{\text{p}}^\dagger X_{\text{V}}^\dagger \frac{1 - \frac{9}{8}\frac{1}{(\nu_j)_{\text{sel}}}\frac{w^{(\text{int})}(\eta)}{(X_{\text{p}}^\dagger)^{1/2}X_{\text{V}}^\dagger}}{1 - \frac{9}{8}\frac{1}{(\nu_i)_{\text{sel}}}(X_{\text{p}}^\dagger)^{1/2}w^{(\text{ext})}(\eta)} = K^\dagger X_{\text{T}}^\dagger, (30a)$$

$$X_{\text{p}}X_{\text{V}} \frac{1 - \frac{9}{8}\frac{\Xi_i}{\Xi_j}\frac{(\nu_j)_{\text{mas}}}{(\nu_i)_{\text{mas}}}\frac{1}{(\nu_j)_{\text{sel}}}\frac{w^{(\text{int})}(\eta)}{X_{\text{p}}^{1/2}X_{\text{V}}}}{1 - \frac{9}{8}\frac{1}{(\nu_i)_{\text{sel}}}X_{\text{p}}^{1/2}w^{(\text{ext})}(\eta)}$$

$$= KX_{\text{T}} \ , \qquad (30b)$$

$$\eta = \Xi_i X_{\text{V}}^\dagger = \Xi_j X_{\text{V}} \ , \qquad y \geq 1 \ , \qquad (30c)$$

$$X_{\text{p}}^\dagger = (m^\dagger)^2 \ , \quad X_{\text{V}}^\dagger = \frac{1}{y^\dagger} \ , \quad X_{\text{T}}^\dagger = \phi \ , \qquad (30d)$$

$$X_{\text{p}} = m^2 \ , \quad X_{\text{V}} = \frac{1}{y} \ , \quad X_{\text{T}} = \phi \ , \qquad (30e)$$

$$K^\dagger = K^\dagger(\Xi_i, \Xi_j) = \frac{(\nu_i)_{\text{sel}}}{(\nu_j)_{\text{sel}}} \ , \qquad (30f)$$

$$K = K(\Xi_i, \Xi_j) = \frac{\Xi_i}{\Xi_j}\left[\frac{(\nu_j)_{\text{mas}}}{(\nu_i)_{\text{mas}}}\right]^2 \frac{(\nu_i)_{\text{sel}}}{(\nu_j)_{\text{sel}}} \ , \qquad (30g)$$

which can be conceived as an equation of state for macrogases. The variables X_{V}, X_{p}, X_{T} play a similar role as the volume, pressure, and temperature for ordinary gases. Accordingly, X_{V}, X_{p}, X_{T}, shall be defined as macrovolume, macropressure, and macrotemperature respectively.

The combination of Eq. (22), Eq. (30d), and Eq. (30e) yields:

$$\frac{X_{\text{V}}^\dagger}{X_{\text{V}}} = \frac{\Xi_i}{\Xi_j} \ , \quad \frac{X_{\text{p}}^\dagger}{X_{\text{p}}} = \left[\frac{(\nu_i)_{\text{mas}}}{(\nu_j)_{\text{mas}}}\right]^2 \ , \quad \frac{X_{\text{T}}^\dagger}{X_{\text{T}}} = 1 \ , \quad (31)$$

which links the variables $(X_V^\dagger, X_p^\dagger, X_T^\dagger)$ to their counterparts (X_V, X_p, X_T) and vice versa.

Strictly speaking, the macrogas equation of state should be deduced from dimensional (instead of dimensionless) virial equations for an assigned subsystem as outlined in Appendix A2. On the other hand, a description in terms of dimensionless variables turns out to be more useful.

If the interaction terms are omitted, $w^{(\text{int})} = w^{(\text{ext})} = 0$, Eq. (30a) and Eq. (30b) reduce to:

$$X_p^\dagger X_V^\dagger = K^\dagger(\Xi_i, \Xi_j) X_T^\dagger \quad , \qquad (32a)$$

$$X_p X_V = K(\Xi_i, \Xi_j) X_T \quad , \qquad (32b)$$

which may be considered as the equation of state of ideal macrogases where "ideal" means "the interaction terms are omitted".

The parameters $K^\dagger$ and K appearing in either macrogas equation of state, depend on the scaled truncation radii Ξ_i and Ξ_j and on the selected density profiles. In other words, the macrogas equation of state is not universal but takes a different form for different density profiles. A restricted number of special cases shall be studied below, grounding on earlier results (CV08), to which an interested reader is addressed for further details. In any case, the following method shall be used: (i) Select two density profiles; (ii) Fix related scaled truncation radii, Ξ_i and Ξ_j; (iii) Choose a macrotemperature, ϕ; (iv) Plot related macroisothermal curves by solving Eq. (30a) or Eq. (30b).

3.1. UU macrogases

The related density profiles are uniform, which is equivalent to polytropes with index $n = 0$ (e.g. Chandrasekhar 1939, Chap. IV, §4; Caimmi 1986) but implies negative distribution functions for stellar fluids (Vandervoort, 1980). The particularization of the general expressions to the case under discussion yields for the quantities of interest (CV08):

$$f_u(\xi_u) = 1 \ , \quad 0 \le \xi_u \le \Xi_u \ , \quad u = i, j \ , \quad (33)$$

$$F_u(\xi_u) = \Xi_u^2 - \xi_u^2 \ , \qquad u = i, j \ , \quad (34)$$

$$(\nu_u)_{\text{mas}} = \Xi_u^3 \ , \qquad u = i, j \ , \quad (35)$$

$$(\nu_u)_{\text{sel}} = \frac{3}{10} \Xi_u^5 \ , \qquad u = i, j \ , \quad (36)$$

$$w^{(\text{int})}(\eta) = -\frac{4}{15} \Xi_i^2 \eta^3 \left(\frac{5}{2} y^2 - \frac{3}{2}\right) \ , \quad (37)$$

$$w^{(\text{ext})}(\eta) = -\frac{4}{15} \Xi_i^2 \eta^3 \ , \quad (38)$$

where Eq. (37) and Eq. (38) hold under the additional restriction of similar and similarly placed boundaries (CV08).

In the case under consideration of uniform density profiles, without loss of generality, it can be assumed a scaled truncation radius $\Xi_u = R_u/r_u^\dagger = 1$, which implies $y = y^\dagger$, $m = m^\dagger$, due to Eq. (22) and

Eq. (35). Accordingly, Eq. (26) reduces to (CV08):

$$\phi = \frac{(m^\dagger)^2}{y^\dagger} \left(\frac{y}{y^\dagger}\right)^5 \frac{1 + \dfrac{(y^\dagger)^3}{m^\dagger} \dfrac{1}{y^5} \left(\dfrac{5}{2} y^2 - \dfrac{3}{2}\right)}{1 + \dfrac{m^\dagger}{(y^\dagger)^3}} \ ,$$
$$y \ge 1 \ , \qquad (39a)$$

$$\phi = \left(\frac{y}{y^\dagger}\right)^5 \frac{m^\dagger (y^\dagger)^2 \left[1 + \dfrac{m^\dagger}{(y^\dagger)^3}\right]}{1 + m^\dagger \left(\dfrac{y}{y^\dagger}\right)^3 \left(\dfrac{5}{2} - \dfrac{3}{2} y^2\right)} \ ,$$
$$0 \le y \le 1 \ , \qquad (39b)$$

where y is the outer to inner ellipsoid axis ratio R_j/R_i according to Eq. (22b). In addition, Eq. (28) and Eq. (29) reduce to:

$$m = \sqrt{\beta^2 + y\phi} - \beta \ , \quad (40a)$$

$$\beta = \frac{1}{2} \frac{1}{y^2} \left(\frac{5}{2} y^2 - \frac{3}{2} - \phi\right) \ , \qquad y \ge 1 \ , \quad (40b)$$

$$\beta = \frac{1}{2} y^3 \left[1 - \left(\frac{5}{2} \frac{1}{y^2} - \frac{3}{2}\right) \phi\right] \ , \quad 0 \le y \le 1 \ , (40c)$$

$$A = \frac{3}{10} \ , \qquad C = -\frac{3}{10} y\phi \ , \qquad B = \frac{3}{5}\beta \ , \quad (40d)$$

where the negative solution is not considered due to the lack of physical meaning.

The explicit expression of the square fractional mass m^2 extracted from Eq. (40a) in dimensionless variables, $X_p = X_p^\dagger = m^2 = (m^\dagger)^2$, $X_V = X_V^\dagger = 1/y = 1/y^\dagger$, $X_T = X_T^\dagger = \phi$, Eq. (30d), Eq. (30e), reads:

$$X_p = 2\beta^2 + \frac{X_T}{X_V} - 2\beta \sqrt{\beta^2 + \frac{X_T}{X_V}} \ , \quad (41a)$$

$$2\beta = X_V^2 \left(\frac{5}{2} \frac{1}{X_V^2} - \frac{3}{2} - X_T\right) ; \ 0 < X_V \le 1, \ (41b)$$

$$2\beta = \frac{1}{X_V^3} \left[1 - \left(\frac{5}{2} X_V^2 - \frac{3}{2}\right) X_T\right] ; \ X_V \ge 1, \ (41c)$$

or more explicitly:

$$X_p = 2\frac{1}{4} X_V^4 \left(\frac{5}{2} \frac{1}{X_V^2} - \frac{3}{2} - X_T\right)^2 + \frac{X_T}{X_V}$$
$$- X_V^2 \left(\frac{5}{2} \frac{1}{X_V^2} - \frac{3}{2} - X_T\right)$$
$$\times \left[\frac{1}{4} X_V^4 \left(\frac{5}{2} \frac{1}{X_V^2} - \frac{3}{2} - X_T\right)^2 + \frac{X_T}{X_V}\right]^{1/2} ;$$
$$0 < X_V \le 1 \ ; \qquad (42a)$$

27

$$X_{\mathrm{p}} = 2\frac{1}{4}\frac{1}{X_{\mathrm{V}}^6}\left[1 - \left(\frac{5}{2}X_{\mathrm{V}}^2 - \frac{3}{2}\right)X_{\mathrm{T}}\right]^2 + \frac{X_{\mathrm{T}}}{X_{\mathrm{V}}}$$

$$- \frac{1}{X_{\mathrm{V}}^3}\left[1 - \left(\frac{5}{2}X_{\mathrm{V}}^2 - \frac{3}{2}\right)X_{\mathrm{T}}\right]$$

$$\times \left\{\frac{1}{4}\frac{1}{X_{\mathrm{V}}^6}\left[1 - \left(\frac{5}{2}X_{\mathrm{V}}^2 - \frac{3}{2}\right)X_{\mathrm{T}}\right]^2 + \frac{X_{\mathrm{T}}}{X_{\mathrm{V}}}\right\}^{1/2} ;$$

$$X_{\mathrm{V}} \geq 1 \quad , \tag{42b}$$

which is the actual UU (AUU) macrogas equation of state.

The ideal UU (IUU) macrogas equation of state is obtained by the combination of Eq. (30e), Eq. (32b), Eq. (35), and Eq. (36). The result is:

$$X_{\mathrm{p}} = \frac{X_{\mathrm{T}}}{X_{\mathrm{V}}} \quad , \tag{43}$$

which represents a hyperbola with equal axes for fixed X_{T}.

Macroisothermal curves related to IUU (tidal potential energy excluded) and AUU (tidal potential energy included) macrogases are plotted in Fig. 4, left and right panel, respectively, for values of the macrotemperature $X_{\mathrm{T}} = 0.85$, 0.90, 0.95, 1.00, 1.05, 1.10 from bottom to top. The coordinates $X_{\mathrm{V}} = X_{\mathrm{V}}^\dagger$, $X_{\mathrm{p}} = X_{\mathrm{p}}^\dagger$, $X_{\mathrm{T}} = X_{\mathrm{T}}^\dagger$ may be conceived as normalized to their fictitious critical counterparts $X_{V_{\mathrm{c}}} = X_{V_{\mathrm{c}}}^\dagger = 1$, $X_{p_{\mathrm{c}}} = X_{p_{\mathrm{c}}}^\dagger = 1$, $X_{T_{\mathrm{c}}} = X_{T_{\mathrm{c}}}^\dagger = 1$ as $\phi = m = m^\dagger$ for $y = y^\dagger = 1$, according to Eq. (39) or Eq. (104), which implies $\phi = 1$ for $m = m^\dagger = 1$. The comparison with ideal and VDW gases, plotted in Fig. 1, shows a similar trend, except the absence of a critical macroisothermal curve, above which the extremum points disappear.
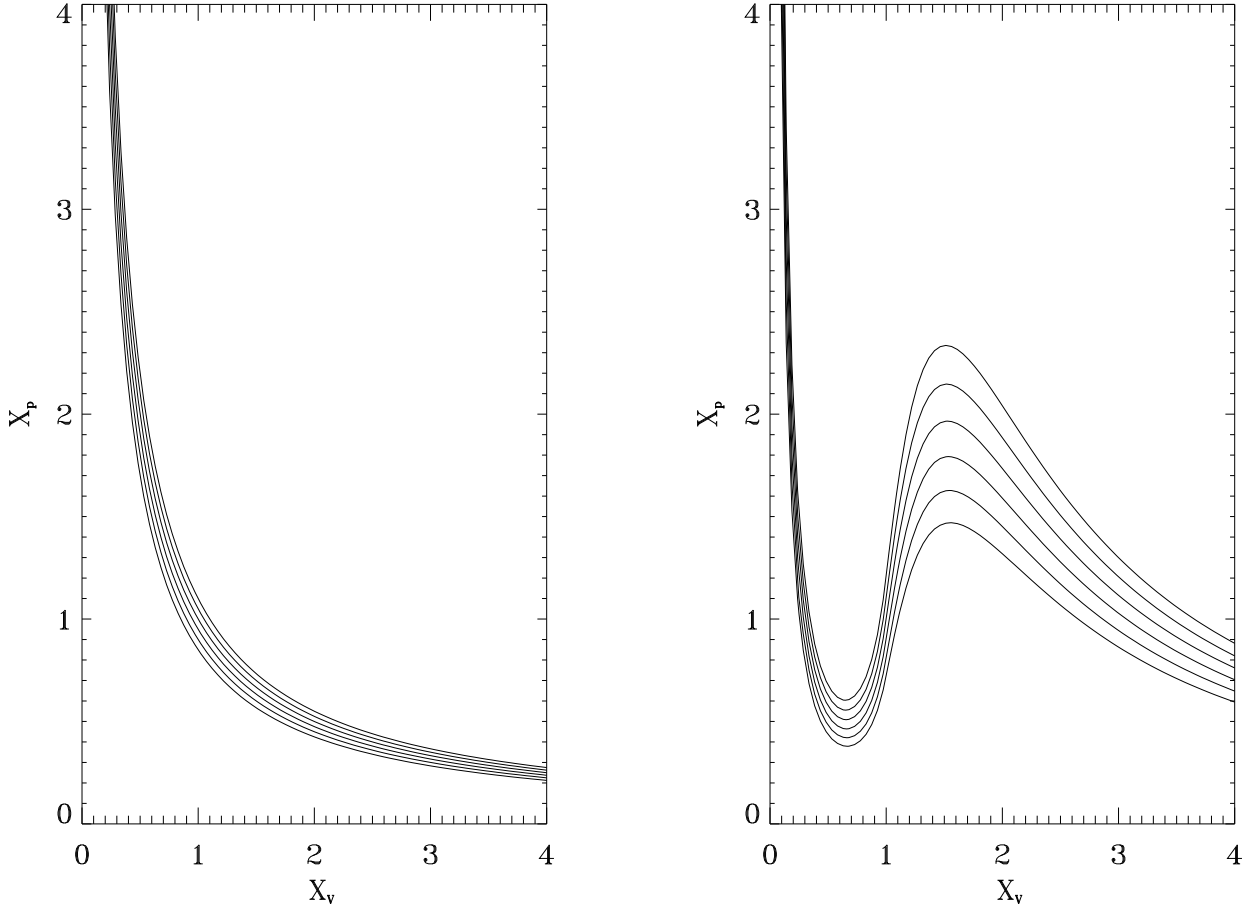

Fig. 4. *Macroisothermal curves related to IUU (left panel) and AUU (right panel) macrogases respectively. Macroisothermal curves (from bottom to top) correspond to $X_{\mathrm{T}} = 0.85$, 0.90, 0.95, 1.00, 1.05, 1.10. No critical macroisothermal curve exists above or below which the extremum points disappear. The coordinates, $X_{\mathrm{V}} = X_{\mathrm{V}}^\dagger$, $X_{\mathrm{p}} = X_{\mathrm{p}}^\dagger$, $X_{\mathrm{T}} = X_{\mathrm{T}}^\dagger$ may be conceived as normalized to their fictitious critical counterparts $X_{V_{\mathrm{c}}} = X_{V_{\mathrm{c}}}^\dagger = 1$, $X_{p_{\mathrm{c}}} = X_{p_{\mathrm{c}}}^\dagger = 1$, $X_{T_{\mathrm{c}}} = X_{T_{\mathrm{c}}}^\dagger = 1$.*
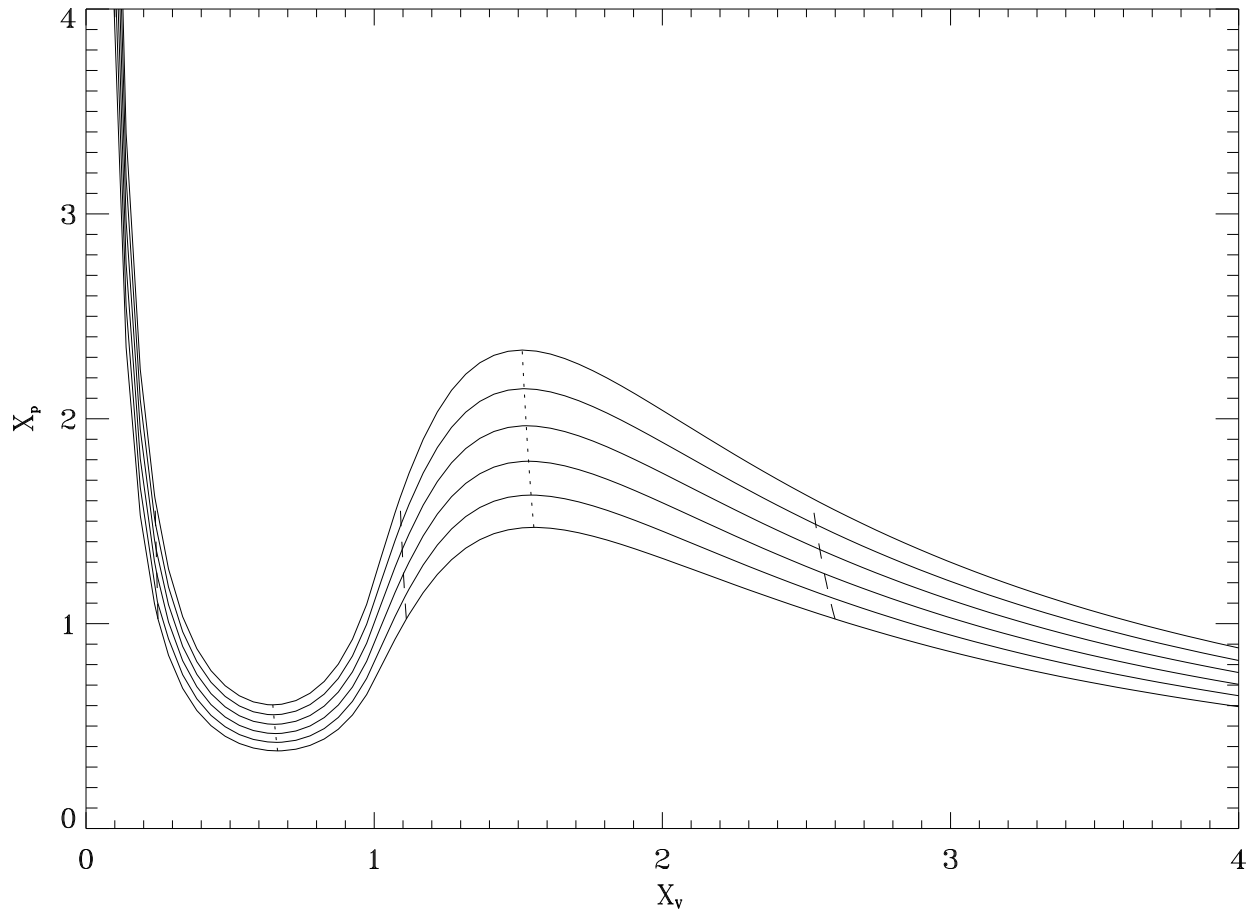
Fig. 5. *Same as in Fig. 4 (right panel). The loci of the extremum points are represented as dotted lines. The loci of the intersections between actual and real macroisothermal curves are represented as dashed lines. The absence of the critical macroisothermal curve makes a band-like instead of a bell-shaped region exist on the plane.*

Contrary to ordinary gases, no experiment can be performed on macrogases to ascertain the existence of a phase transition moving along a selected macroisothermal curve where the path is a horizontal line instead of a curve including the extremum points. Then the existence of the above mentioned phase transition and flat real macroisothermal curves must necessarily be assumed as a working hypothesis by analogy with VDW isothermal curves (below the critical one). The loci of extremum points of AUU macroisothermal curves plotted in Fig. 4 (right panel) are represented as dotted lines in Fig. 5.

Unlike the VDW equation of state Eq. (10) the AUU macrogas equation of state Eq. (42) is not analytically integrable. Then, the procedure used for determining a selected macroisothermal curve must be numerically performed. The main steps are (i) Calculate the intersections X_{V_A}, X_{V_C}, X_{V_E}, $X_{V_A} < X_{V_C} < X_{V_E}$, between the generic horizon-

tal line in the $(OX_V X_p)$ plane, $X_p = $ const, and the AUU macrogas equation of state within the range $X_{p_B} < X_p < X_{p_D}$ where B and D denote the extremum points of minimum and maximum, respectively; (ii) Calculate the area of the regions ABC and CDE; (iii) Find the special value $X_p = X_{p_0}$, which makes the two areas equal; (iv) Trace the real UU (RUU) macroisothermal curve as a horizontal line connecting the points (X_{V_A}, X_{p_A}), (X_{V_C}, X_{p_C}), (X_{V_E}, X_{p_E}), $X_{p_A} = X_{p_C} = X_{p_E} = X_{p_0}$.

The loci of the intersections between AUU and RUU macroisothermal curves are represented as dashed lines in Fig. 5. The absence of a critical macroisothermal curve makes a band-like instead of a bell-shaped region exist on the $(OX_V X_p)$ plane as shown by comparison with Fig. 2. The AUU and RUU macroisothermal curves are plotted in Fig. 6 with regard to the special case $X_T = 0.85$.
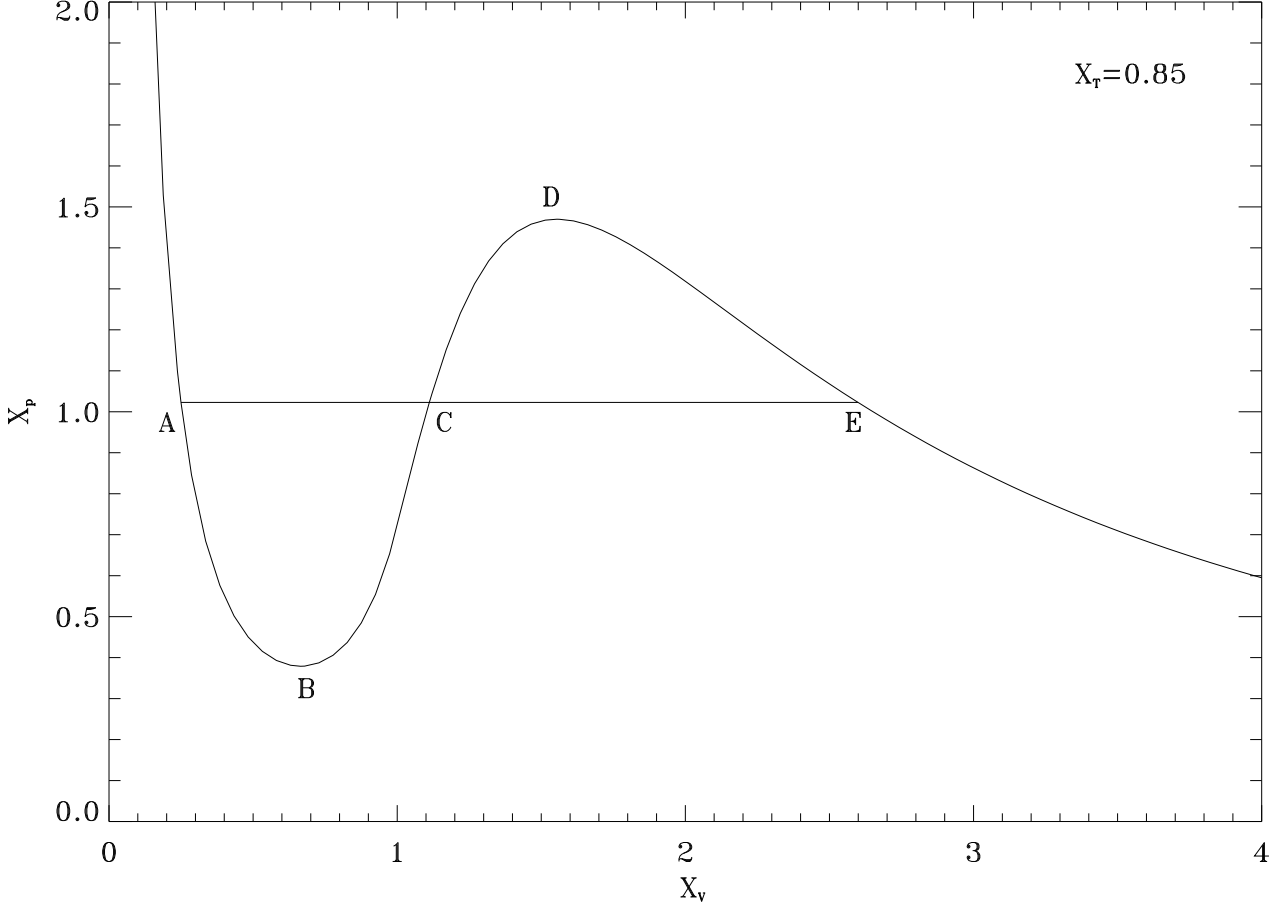
Fig. 6. *A specific ($X_{\mathrm{T}} = 0.85$) AUU and corresponding RUU macroisothermal curve. The above mentioned curves coincide within the range, $X_{\mathrm{V}} \leq X_{V_{\mathrm{A}}}$, $X_{\mathrm{V}} \geq X_{V_{\mathrm{E}}}$. The regions* ABC *and* CDE *have equal areas. For further details refer to the text.*

3.2. HH macrogases

The related density profiles exhibit a central cusp and null value at infinite distances (Hernquist 1990), and have been proved to be consistent with nonnegative distribution functions in an acceptable parameter range (Ciotti 1996). The particularization of the general expressions to the case under discussion yields for the quantities of interest (CV08):

$$f_u(\xi_u) = \frac{8}{\xi_u(1 + \xi_u)^3} \; ; \; 0 \leq \xi_u \leq \Xi_u \; ; \; u = i, j \; , \quad (44)$$

$$F_u(\xi_u) = \frac{8}{(1 + \xi_u)^2} - \frac{8}{(1 + \Xi_u)^2} \; ; \quad u = i, j \; , \quad (45)$$

$$(\nu_u)_{\mathrm{mas}} = \frac{12\Xi_u^2}{(1 + \Xi_u)^2} \; ; \qquad u = i, j \; , \quad (46)$$

$$(\nu_u)_{\mathrm{sel}} = \frac{12\Xi_u^3(4 + \Xi_u)}{(1 + \Xi_u)^4} \; ; \qquad u = i, j \; , \quad (47)$$

$$
\begin{aligned}
w^{(\mathrm{int})}(\eta) = -128y^\dagger \Bigg\{ &\frac{1}{2} \frac{1}{(y^\dagger - 1)^4} \Bigg[-\frac{(y^\dagger - 1)^2 y^\dagger \eta}{(y^\dagger \eta + 1)^2} \\
&+ \frac{2(y^\dagger - 1)\eta}{1 + \eta} + \frac{(y^\dagger - 1)(y^\dagger + 3)y^\dagger \eta}{y^\dagger \eta + 1} \\
&+ 2(2y^\dagger + 1)\ln\frac{\eta + 1}{y^\dagger \eta + 1} \Bigg] - \frac{1}{2}\frac{1}{(1 + \Xi_j)^2} \\
&\times \frac{1}{(y^\dagger)^2}\Bigg[1 - \frac{2y^\dagger \eta + 1}{(y^\dagger \eta + 1)^2} \Bigg] \Bigg\} \; , \\
&y^\dagger \neq 1 \; ; \quad\quad\quad\quad\quad\quad (48a)
\end{aligned}
$$

$$
\begin{aligned}
w^{(\mathrm{int})}(\eta) = -128 \Bigg\{ &\frac{1}{12}\Bigg[-\frac{4\eta + 1}{(\eta + 1)^4} + 1 \Bigg] \\
&- \frac{1}{2}\frac{1}{(1 + \Xi_j)^2}\frac{\eta^2}{(\eta + 1)^2} \Bigg\} \; ; \\
&y^\dagger = 1 \; , \quad\quad\quad\quad\quad\quad (48b)
\end{aligned}
$$

$$w^{(\text{ext})}(\eta) = -128\left\{-\frac{1}{2}\frac{1}{(y^\dagger-1)^4}\left[\frac{(y^\dagger-1)^2\eta}{(\eta+1)^2}\right.\right.$$

$$+\frac{2(y^\dagger)^2(y^\dagger-1)\eta}{1+y^\dagger\eta}+\frac{(y^\dagger-1)(3y^\dagger+1)\eta}{\eta+1}$$

$$\left.-2y^\dagger(y^\dagger+2)\ln\frac{y^\dagger\eta+1}{\eta+1}\right]-\frac{1}{2}\frac{1}{(1+\Xi_i)^2}$$

$$\times\frac{\eta^2}{(\eta+1)^2}\right\}\quad;\qquad y^\dagger\neq 1\quad,\qquad(49a)$$

$$w^{(\text{ext})}(\eta) = 128\left\{\frac{1}{12}\left[\frac{4\eta+1}{(\eta+1)^4}-1\right]+\frac{1}{2}\frac{1}{(1+\Xi_i)^2}\right.$$

$$\left.\times\frac{\eta^2}{(\eta+1)^2}\right\}\quad;\qquad y^\dagger=1\quad,\qquad(49b)$$

using Eq. (24) and Eqs. (46)-(49), the actual HH (AHH) macrogas equation of state is obtained from the particularization of Eqs. (30) to the case of interest for the domain $y\geq 1$. The extension to the domain $0\leq y\leq 1$ can be done following the procedure outlined above in dealing with Eq. (26).

In absence of truncation radius, $\Xi\to+\infty$, $\eta\to+\infty$, and Eqs. (45)-(49) reduce to (CV08):

$$\lim_{\Xi_u\to+\infty}F_u(\xi_u)=\frac{8}{(1+\xi_u)^2}\quad;\qquad u=i,j\quad,\quad(50)$$

$$\lim_{\Xi_u\to+\infty}(\nu_u)_{\text{mas}}=12\quad;\qquad u=i,j\quad,\qquad(51)$$

$$\lim_{\Xi_u\to+\infty}(\nu_u)_{\text{sel}}=12\quad;\qquad u=i,j\quad,\qquad(52)$$

$$\lim_{\eta\to+\infty}w^{(\text{int})}(\eta)=-\frac{64y^\dagger}{(y^\dagger-1)^4}\left[-2(2y^\dagger+1)\ln y^\dagger\right.$$

$$\left.+(y^\dagger-1)(y^\dagger+5)\right];y^\dagger\neq 1,\ (53a)$$

$$\lim_{\eta\to+\infty}w^{(\text{int})}(\eta)=-\frac{32}{3}\quad;\qquad y^\dagger=1\quad,\qquad(53b)$$
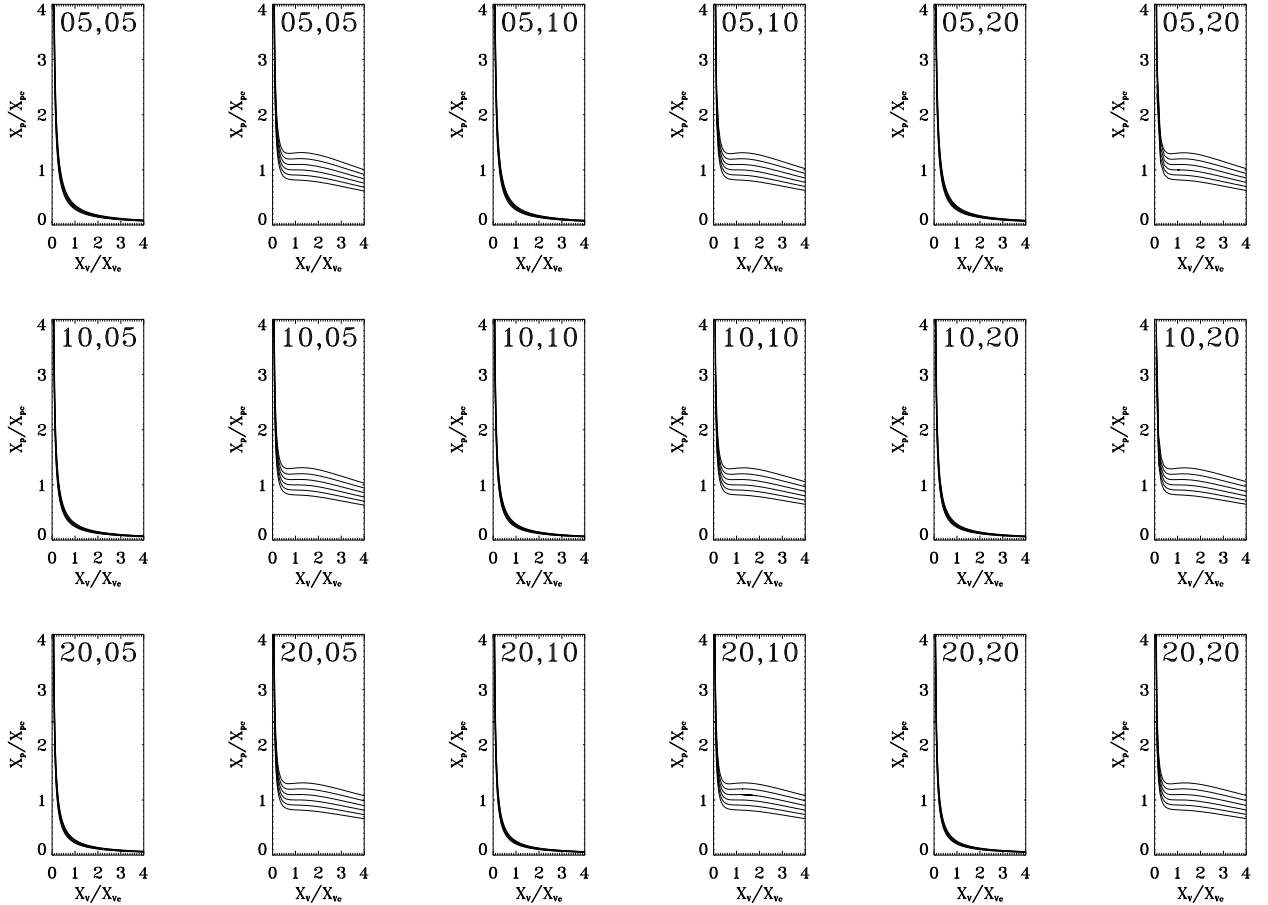
Fig. 7. *Macroisothermal curves ($\mathcal{X}_{\text{p}}=X_{\text{p}}/X_{p_c}$ vs. $\mathcal{X}_{\text{V}}=X_{\text{V}}/X_{V_c}$) related to IHH (left panels) and AHH (right panels) macrogases respectively, for different values of scaled truncation radii (Ξ_i,Ξ_j) labelled on each panel. Macroisothermal curves (from bottom to top) correspond to $\mathcal{X}_{\text{T}}=X_{\text{T}}/X_{T_c}=0.90,\ 0.95,\ 1.00,\ 1.05,\ 1.10,\ 1.15$. The limit, ($\Xi_i,\Xi_j$)$\to(+\infty,+\infty)$, makes only little changes.*

$$\lim_{\eta \to +\infty} w^{(\text{ext})}(\eta) = -\frac{64}{(y^\dagger - 1)^4} \left[2y^\dagger(y^\dagger + 2) \ln y^\dagger \right.$$
$$\left. -(y^\dagger - 1)(5y^\dagger + 1) \right] ; y^\dagger \neq 1, \text{(54a)}$$

$$\lim_{\eta \to +\infty} w^{(\text{ext})}(\eta) = -\frac{32}{3} \quad ; \qquad y^\dagger = 1 \quad , \tag{54b}$$

using Eq. (24) and Eqs. (51)-(54), the AHH macrogas equation of state in the special situation under discussion, is obtained from the particularization of Eqs. (30) to the case of interest.

The ideal situation where the interaction terms are omitted is obtained using Eqs. (32) instead of Eqs. (30). More specifically, the ideal HH (IHH) macrogas equation of state is derived by the combination of Eq. (30e), Eq. (32b), Eq. (46), and Eq. (47).

The result is:

$$X_{\text{p}} = \frac{4 + \Xi_i}{4 + \Xi_j} \frac{X_{\text{T}}}{X_{\text{V}}} \quad , \tag{55}$$

which represents a hyperbola with different axes (unless $\Xi_i = \Xi_j$) for fixed X_{T}.

Macroisothermal curves ($\mathcal{X}_{\text{p}} = X_{\text{p}}/X_{p_c}$ vs. $\mathcal{X}_{\text{V}} = X_{\text{V}}/X_{V_c}$) related to IHH (tidal potential energy excluded) and AHH (tidal potential energy included) macrogases are plotted in Fig. 7, left and right panels, for different values of scaled truncation radii, (Ξ_i, Ξ_j), labelled on each panel, and same values of the reduced macrotemperature: $\mathcal{X}_{\text{T}} = X_{\text{T}}/X_{T_c} = 0.90, 0.95, 1.00, 1.05, 1.10, 1.15$, from bottom to top.
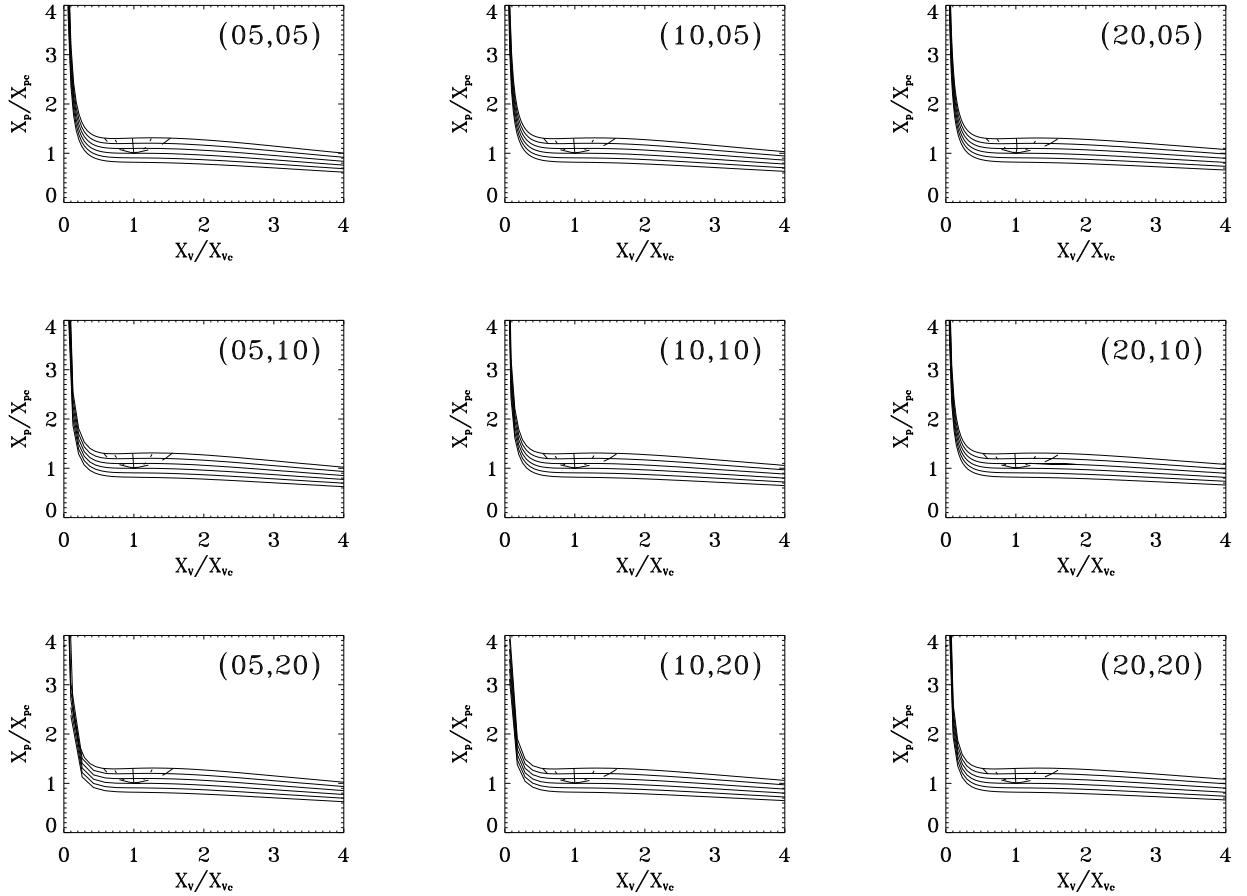

Fig. 8. *AHH macroisothermal curves ($\mathcal{X}_{\text{p}} = X_{\text{p}}/X_{p_c}$ vs. $\mathcal{X}_{\text{V}} = X_{\text{V}}/X_{V_c}$) for different choices of scaled truncation radii (Ξ_i, Ξ_j) labelled on each panel. Macroisothermal curves (from bottom to top) correspond to $\mathcal{X}_{\text{T}} = X_{\text{T}}/X_{T_c} = 0.90, 0.95, 1.00, 1.05, 1.10, 1.15$. The limit ($\Xi_i, \Xi_j$) $\to$ ($+\infty, +\infty$) makes only little changes. RHH macroisothermal curves, when different from their AHH counterparts, lie within the larger reversed bell-shaped region in each panel. The loci of intersections between AHH and RHH macroisothermal curves are represented as trifid curves where the left branch corresponds to $\mathcal{X}_{V_A}$, the right branch to $\mathcal{X}_{V_E}$, and the middle branch to $\mathcal{X}_{V_C}$. The critical point is the common origin. The loci of AHH macroisothermal curve extremum points are represented as dotted curves starting from the critical point where the left branch corresponds to minimum points and the right branch to maximum points.*

The limit $(\Xi_i, \Xi_j) \to (+\infty, +\infty)$, makes only little changes. Owing to Eq. (22a) and Eq. (31), $X_V^\dagger = X_V y^\dagger / y$ and $X_p^\dagger = X_p (m^\dagger / m)^2$, which implies $\cancel{X}_V^\dagger = \cancel{X}_V$ and $\cancel{X}_p^\dagger = \cancel{X}_p$. The comparison with ideal and VDW gases, plotted in Fig. 1, shows a similar but reversed trend. More specifically, extremum points occur above instead of below the critical macroisothermal curve. A complete analogy can be obtained using the transformations $X_V \to 1/X_V$, $X_p \to 1/X_p$, $X_T \to 1/X_T$.

The existence of a phase transition moving along a selected macroisothermal curve where the path is a horizontal line instead of a curve including the extremum points, must necessarily be assumed as a working hypothesis due to the analogy between VDW isothermal curves and AHH macroisothermal curves. As in the case of UU macrogases, AHH macroisothermal curves must be numerically determined following the same procedure outlined in Subsection 3.1. Characteristic loci of AHH macroisothermal curves plotted in Fig. 7 (right panels) are represented in Fig. 8.

The loci of intersections between AHH and real HH (RHH) macroisothermal curves, are represented in Fig. 8 as trifid curves, where the left branch corresponds to $\cancel{X}_{V_A}$, the right branch to $\cancel{X}_{V_E}$, and the middle branch to $\cancel{X}_{V_C}$. The critical point is the common starting point. The loci of AHH macroisothermal curve extremum points are represented in Fig. 8 as dotted curves starting from the critical point, where the left branch corresponds to minimum points and the right branch to maximum points. The RHH macroisothermal curves, when different from their AHH counterparts, lie within the larger bell-shaped regions. The limit $(\Xi_i, \Xi_j) \to (+\infty, +\infty)$ makes only little changes. Values of parameters $\cancel{X}_T$, $\cancel{X}_{V_A}$, $\cancel{X}_{V_B}$, $\cancel{X}_{V_C}$, $\cancel{X}_{V_D}$, $\cancel{X}_{V_E}$, $\cancel{X}_{p_B}$, $\cancel{X}_{p_C}$, $\cancel{X}_{p_D}$ are listed in Table 1 within the range $1.00 < \cancel{X}_T \leq 1.15$ using a step $\Delta \cancel{X}_T = 0.01$ in the limit $(\Xi_i, \Xi_j) \to (+\infty, +\infty)$. The AHH macroisothermal curves are plotted in Fig. 9 for scaled truncation radii (Ξ_i, Ξ_j) as in Fig. 8 with regard to the special case $\cancel{X}_T = 1.15$. The limit $(\Xi_i, \Xi_j) \to (+\infty, +\infty)$ makes only little changes as shown by comparison with the dashed curve.

Fig. 9. *AHH macroisothermal curves for scaled truncation radii (Ξ_i, Ξ_j) as in Fig. 8 with regard to the special case $\cancel{X}_T = X_T/X_{T_c} = 1.15$. The limit, $(\Xi_i, \Xi_j) \to (+\infty, +\infty)$ makes only little changes as shown by comparison with the dashed curve.*
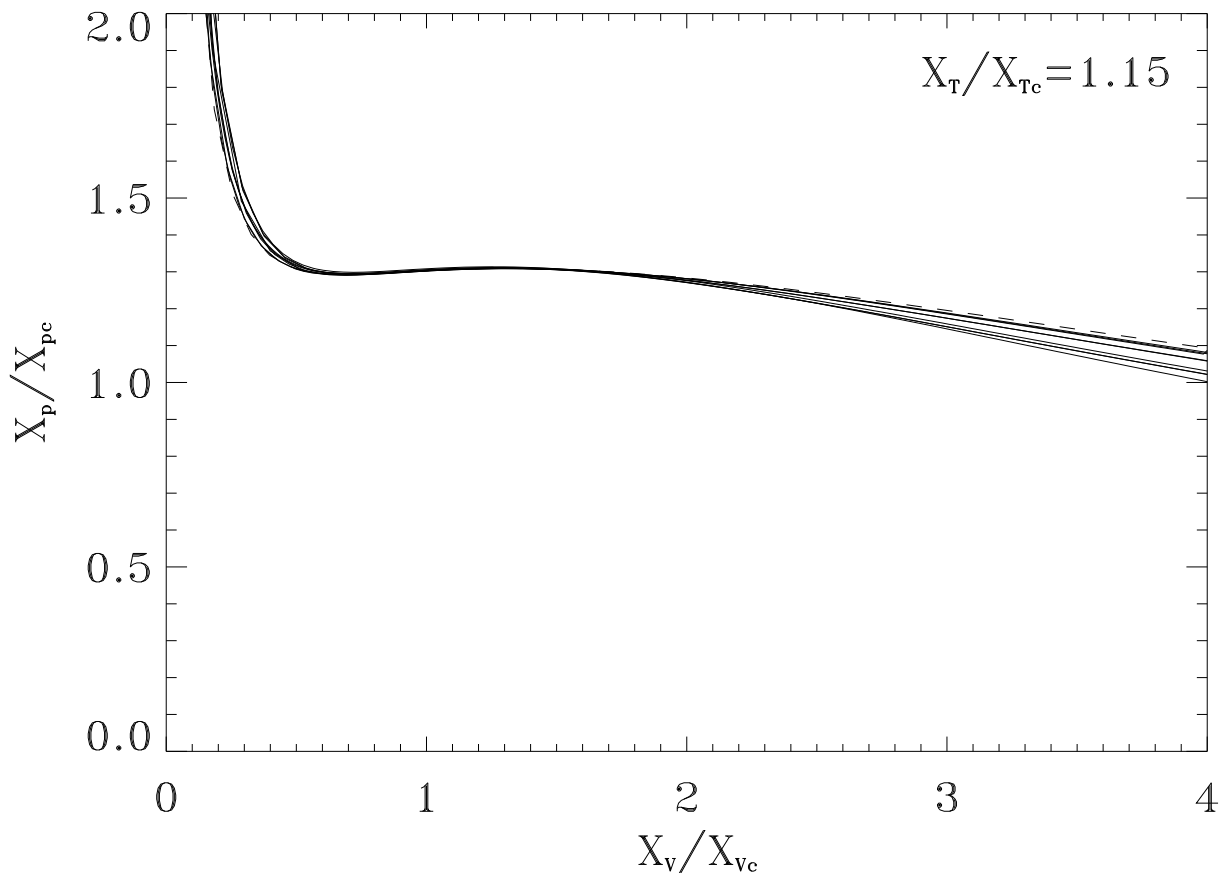
Table 1. Values of parameters $\bar{X}_T$, $\bar{X}_{V_A}$, $\bar{X}_{V_B}$, $\bar{X}_{V_C}$, $\bar{X}_{V_D}$, $\bar{X}_{V_E}$, $\bar{X}_{p_B}$, $\bar{X}_{p_C}$, $\bar{X}_{p_D}$ within the range $1.00 < \bar{X}_T \leq 1.15$ using a step $\Delta \bar{X}_T = 0.01$ except near the critical point where convergence was not attained. All values equal unity at the critical point. Results are related to infinitely extended configurations $(\Xi_i, \Xi_j) \to (+\infty, +\infty)$. Index captions: A, C, E - intersections between AHH and RHH macroisothermal curves; B - extremum point of minimum; D - extremum point of maximum. Extremum points are related to AHH macroisothermal curves, while their RHH counterparts are flat within the range $\bar{X}_{V_A} \leq \bar{X}_V \leq \bar{X}_{V_E}$. For aesthetical reasons, 01 on head columns stands for unity.

$\bar{X}_T$	$10\bar{X}_{V_A}$	$10\bar{X}_{V_B}$	$10\bar{X}_{V_C}$	$01\bar{X}_{V_D}$	$01\bar{X}_{V_E}$	$01\bar{X}_{p_B}$	$01\bar{X}_{p_C}$	$01\bar{X}_{p_D}$
1.014	8.3150	8.9774	9.9858	1.1016	1.1854	1.0264	1.0266	1.0268
1.015	8.2595	8.9420	9.9849	1.1051	1.1921	1.0283	1.0285	1.0287
1.02	8.0099	8.7810	9.9803	1.1211	1.2231	1.0378	1.0381	1.0384
1.03	7.6038	8.5136	9.9711	1.1475	1.2756	1.0568	1.0575	1.0580
1.04	7.2739	8.2912	9.9620	1.1694	1.3203	1.0759	1.0770	1.0778
1.05	6.9927	8.0979	9.9533	1.1884	1.3600	1.0951	1.0966	1.0978
1.06	6.7463	7.9255	9.9446	1.2054	1.3961	1.1144	1.1165	1.1181
1.07	6.5262	7.7690	9.9359	1.2207	1.4293	1.1338	1.1365	1.1385
1.08	6.3269	7.6252	9.9277	1.2348	1.4604	1.1533	1.1566	1.1591
1.09	6.1447	7.4920	9.9192	1.2478	1.4895	1.1730	1.1770	1.1799
1.10	5.9767	7.3676	9.9112	1.2600	1.5171	1.1927	1.1975	1.2009
1.11	5.8209	7.2508	9.9031	1.2714	1.5434	1.2126	1.2182	1.2222
1.12	5.6755	7.1406	9.8950	1.2821	1.5685	1.2325	1.2391	1.2436
1.13	5.5393	7.0362	9.8872	1.2923	1.5925	1.2526	1.2601	1.2652
1.14	5.4111	6.9370	9.8796	1.3019	1.6155	1.2728	1.2813	1.2870
1.15	5.2902	6.8425	9.8720	1.3111	1.6378	1.2931	1.3027	1.3090

Table 2. Values of the scaling fractional mass $m^\dagger$ the fractional mass m the scaling fractional radius $y^\dagger$ the fractional truncation radius y and the fractional energy ϕ related to the critical point i.e. the horizontal inflexion point on the critical macroisothermal curve for selected scaled truncation radii (Ξ_i, Ξ_j) of HH density profiles. In absence of truncation radius $(\Xi_i, \Xi_j) \to (+\infty, +\infty)$ the results are independent of $y/y^\dagger = \Xi_j/\Xi_i$.

(Ξ_i,Ξ_j)	$m^\dagger$	m	$y^\dagger$	y	φ
(05,05)	07.10	07.10	2.32	2.32	06.86
(05,10)	07.72	09.18	2.43	4.86	08.17
(05,20)	07.90	10.31	2.46	9.83	08.62
(10,05)	11.15	09.37	3.18	1.59	09.44
(10,10)	11.88	11.88	3.30	3.30	11.03
(10,20)	12.10	13.28	3.33	6.67	11.57
(20,05)	15.06	11.53	4.00	1.00	12.09
(20,10)	15.83	14.42	3.88	1.94	13.94
(20,20)	16.08	16.08	3.92	3.92	14.59
(∞,∞)	20.22	20.22	4.26	...	18.15

Values of parameters, $m^\dagger$, m, $y^\dagger$, y, ϕ, related to the critical macroisothermal curve, for selected scaled truncation radii (Ξ_i, Ξ_j) are listed in Table 2.

A better method has been used with respect to an earlier attempt (CV08) yielding improved results.

3.3. HN/NH macrogases

A description of H density profiles has been provided in Subsection 3.2. The remaining N density profiles also exhibit a central cusp and null values at infinite distances (Navarro et al. 1995, 1996, 1997). Mass distributions defined by an inner H and outer N density profile were found to be self-consistent in an acceptable parameter range with regard to the non negativity of the distribution function (Lowenstein and White 1999) using a theorem stated in an earlier attempt (Ciotti and Pellegrini 1992). The particularization of the general expressions to N density profiles and HN macrogases yields for the quantities of interest (CV08):

$$f_u(\xi_u) = \frac{4}{\xi_u(1+\xi_u)^2} \; ; \quad 0 \le \xi_u \le \Xi_u \; ; \quad u = N \; , \quad (56)$$

$$F_u(\xi_u) = \frac{8}{1+\xi_u} - \frac{8}{1+\Xi_u} \; ; \quad u = N \; , \quad (57)$$

$$(\nu_u)_{\mathrm{mas}} = 12 \left[\ln(1+\Xi_u) - \frac{\Xi_u}{1+\Xi_u} \right] ; \; u = N \; , \quad (58)$$

$$(\nu_u)_{\mathrm{sel}} = 36 \frac{\Xi_u(2+\Xi_u) - 2(1+\Xi_u)\ln(1+\Xi_u)}{(1+\Xi_u)^2} , \quad (59)$$

$$w^{(\mathrm{int})}(\eta) = -\frac{64 y^\dagger}{(y^\dagger-1)^3} \left[-\frac{(y^\dagger-1)^2}{y^\dagger} \frac{y^\dagger \eta(y^\dagger \eta + 2)}{(y^\dagger \eta + 1)^2} \right.$$
$$+ \frac{2 y^\dagger \eta(y^\dagger - 1)}{y^\dagger \eta + 1} + 2 \ln \frac{\eta+1}{y^\dagger \eta + 1}$$
$$\left. - \frac{(y^\dagger-1)^3}{1+\Xi_j} \frac{\eta^2}{(y^\dagger \eta + 1)^2} \right] \; ;$$
$$y^\dagger \ne 1 \; ; \quad i = H \; ; \quad j = N \; , \quad (60\mathrm{a})$$

$$w^{(\mathrm{int})}(\eta) = -\frac{64 \eta^2}{(\eta+1)^2} \left[\frac{\eta+3}{3(\eta+1)} - \frac{1}{1+\Xi_j} \right] \; ;$$
$$y^\dagger = 1 \; ; \quad i = H \; ; \quad j = N \; , \quad (60\mathrm{b})$$

$$w^{(\mathrm{ext})}(\eta) = -\frac{64}{(y^\dagger-1)^2} \left\{ -\frac{\eta}{\eta+1} - \frac{y^\dagger \eta}{y^\dagger \eta + 1} \right.$$
$$- \frac{y^\dagger + 1}{y^\dagger - 1} \ln \frac{\eta+1}{y^\dagger \eta + 1} - \frac{(y^\dagger-1)^2}{(1+\Xi_i)^2}$$
$$\left. \times \left[-\frac{\eta}{\eta+1} + \ln(\eta+1) \right] \right\} \; ;$$
$$y^\dagger \ne 1 \; ; \quad i = H \; ; \quad j = N \; ; \quad (61\mathrm{a})$$

$$w^{(\mathrm{ext})}(\eta) = -64 \left\{ \frac{1}{6} \frac{\eta^2(\eta+3)}{(\eta+1)^3} - \frac{1}{(1+\Xi_i)^2} \right.$$
$$\left. \times \left[-\frac{\eta}{\eta+1} + \ln(\eta+1) \right] \right\} \; ;$$
$$y^\dagger = 1 \; ; \quad i = H \; ; \quad j = N \; , \quad (61\mathrm{b})$$

using Eq. (24), Eq. (46), Eq. (47), and Eqs. (58)-(61) the HN macrogas equation of state is obtained from the particularization of Eqs. (30) to the case of interest for the domain $y \ge 1$. The extension to the domain $0 \le y \le 1$ can be done following the procedure outlined above in dealing with Eq. (26).

To this aim, the counterparts of Eqs. (60)-(61), related to NH macrogases ($i = N$, $j = H$), are needed. The particularization of Eqs. (25) to the case under discussion, yields:

$$w^{(\mathrm{int})}(\eta) = -\frac{64 y^\dagger}{(y^\dagger-1)^2} \left\{ -\frac{\eta}{1+\eta} - \frac{\Xi_i}{1+\Xi_i} - \frac{y^\dagger+1}{y^\dagger-1} \right.$$
$$\left. \times \ln \frac{1+\eta}{1+\Xi_i} - \frac{(y^\dagger-1)^2}{(y^\dagger)^2} \frac{1}{(1+\Xi_j)^2} \right.$$

$$\times \left[\ln(1+\Xi_i) - \frac{\Xi_i}{1+\Xi_i} \right] \right\} \; ;$$
$$y^\dagger \ne 1 \; ; \quad i = N \; ; \quad j = H \; , \quad (62\mathrm{a})$$

$$w^{(\mathrm{int})}(\eta) = -64 \left\{ \frac{1}{6} \frac{\eta^2(3+\eta)}{(1+\eta)^3} - \frac{1}{(1+\Xi_j)^2} \right.$$
$$\left. \times \left[\ln(1+\eta) - \frac{\eta}{1+\eta} \right] \right\} \; ;$$
$$y^\dagger = 1 \; ; \quad i = N \; ; \quad j = H \; , \quad (62\mathrm{b})$$

$$w^{(\mathrm{ext})}(\eta) = -\frac{64}{(y^\dagger-1)^3} \left[2(y^\dagger-1) \frac{\eta}{1+\eta} \right.$$
$$+ (y^\dagger-1)^2 \frac{\eta(2+\eta)}{(1+\eta)^2} + 2 y^\dagger \ln \frac{1+\eta}{1+\Xi_i}$$
$$\left. - \frac{(y^\dagger-1)^3}{1+\Xi_i} \frac{\eta^2}{(1+\eta)^2} \right] \; ;$$
$$y^\dagger \ne 1 \; ; \quad i = N \; ; \quad j = H \; , \quad (63\mathrm{a})$$

$$w^{(\mathrm{ext})}(\eta) = -64 \left[\frac{1}{3} \frac{\eta^2(3+\eta)}{(1+\eta)^3} - \frac{1}{1+\Xi_i} \frac{\eta^2}{(1+\eta)^2} \right] \; ;$$
$$y^\dagger = 1 \; ; \quad i = N \; ; \quad j = H \; , \quad (63\mathrm{b})$$

where $\Xi_i = \Xi_N$, $\Xi_j = \Xi_H$, while the contrary holds with regard to Eqs. (60)-(61). Using Eq. (24), Eqs. (46)-(47), Eqs. (58)-(59), Eqs. (62)-(63) the NH macrogas equation of state is obtained from the particularization of Eqs. (30) to the case of interest for the domain $y \ge 1$ which corresponds to $0 \le y \le 1$ for HN macrogases and vice versa.

In absence of truncation radius $\Xi \to +\infty$, $\eta \to +\infty$ and Eqs. (57)-(61) reduce to:

$$\lim_{\Xi_u \to +\infty} F_u(\xi_u) = \frac{8}{1+\xi_u} \; ; \qquad u = N \; , \quad (64)$$

$$\lim_{\Xi_u \to +\infty} (\nu_u)_{\mathrm{mas}} = +\infty \; ; \qquad u = N \; , \quad (65)$$

$$\lim_{\Xi_u \to +\infty} (\nu_u)_{\mathrm{sel}} = 36 \; ; \qquad u = N \; , \quad (66)$$

$$\lim_{\eta \to +\infty} w^{(\mathrm{int})}(\eta) = -\frac{64}{(y^\dagger-1)^3} \left[(y^\dagger)^2 - 1 - 2 y^\dagger \ln y^\dagger \right]$$
$$y^\dagger \ne 1 \; , \quad (67\mathrm{a})$$

$$\lim_{\eta \to +\infty} w^{(\mathrm{int})}(\eta) = -\frac{64}{3} \; ; \qquad y^\dagger = 1 \; , \quad (67\mathrm{b})$$

$$\lim_{\eta \to +\infty} w^{(\mathrm{ext})}(\eta) = -\frac{64}{(y^\dagger-1)^2} \left[\frac{y^\dagger+1}{y^\dagger-1} \ln y^\dagger - 2 \right] \; ;$$
$$y^\dagger \ne 1 \; , \quad (68\mathrm{a})$$

$$\lim_{\eta \to +\infty} w^{(\mathrm{ext})}(\eta) = -\frac{32}{3} \; ; \qquad y^\dagger = 1 \; , \quad (68\mathrm{b})$$
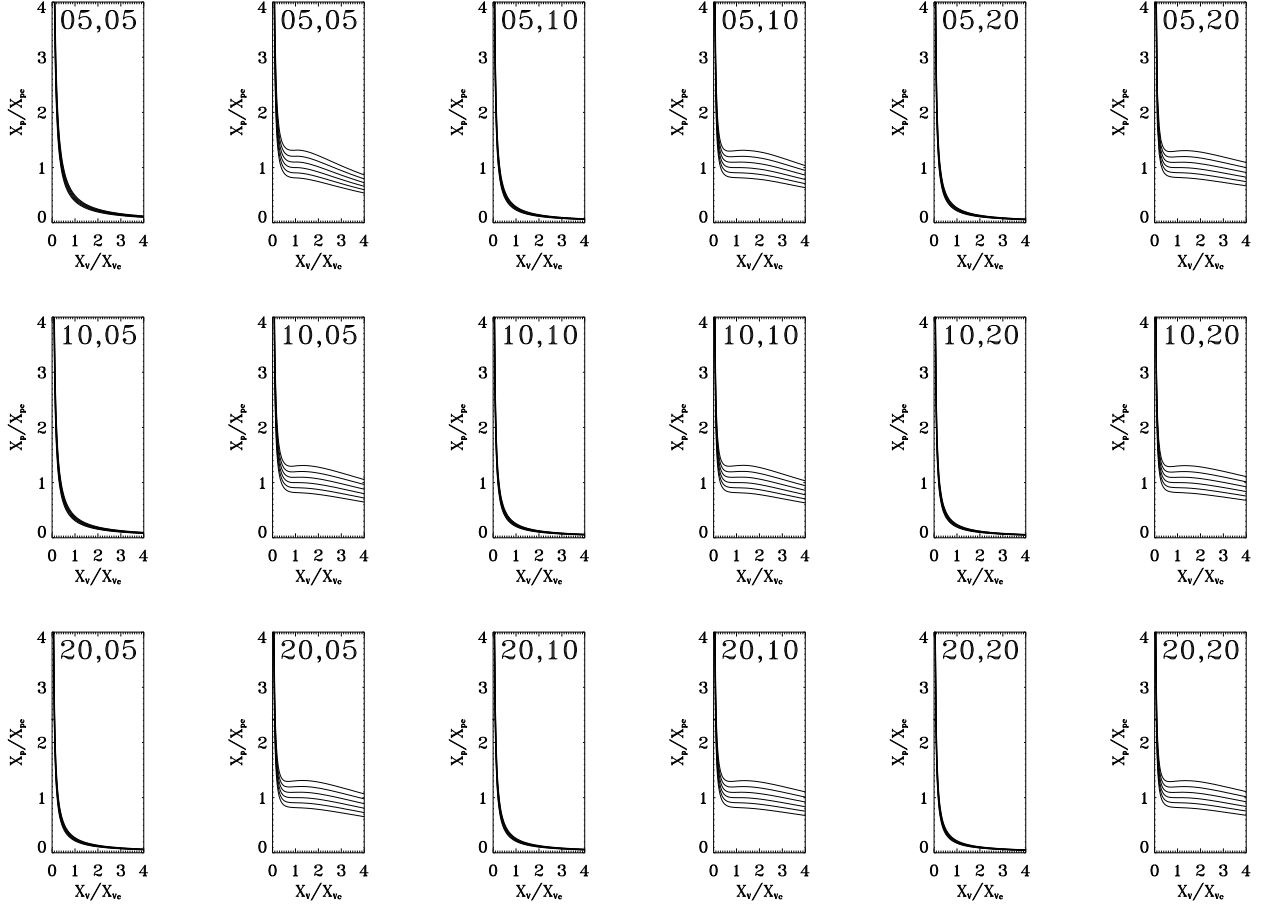
Fig. 10. *Macroisothermal curves ($\check{X}_{\mathrm{p}} = X_{\mathrm{p}}/X_{p_c}$ vs. $\check{X}_{\mathrm{V}} = X_{\mathrm{V}}/X_{V_c}$) related to IHN/INH (left panels) and AHN/ANH (right panels) macrogases respectively for different values of scaled truncation radii (Ξ_i, Ξ_j) labelled on each panel. Macroisothermal curves (from bottom to top) correspond to $\check{X}_{\mathrm{T}} = X_{\mathrm{T}}/X_{T_c} = 0.90$, 0.95, 1.00, 1.05, 1.10, 1.15. The limit (Ξ_i, Ξ_j) $\to$ ($+\infty, +\infty$) makes only little changes.*

where the self potential-energy profile factor remains finite, although the mass profile factor undergoes a logarithmic divergence. Similarly, Eqs. (62)-(63) reduce to:

$$\lim_{\eta \to +\infty} w^{(\mathrm{int})}(\eta) = -\frac{64y^\dagger}{(y^\dagger - 1)^2} \left[\frac{y^\dagger + 1}{y^\dagger - 1} \ln y^\dagger - 2 \right] \ ;$$
$$y^\dagger \neq 1 \ , \tag{69a}$$

$$\lim_{\eta \to +\infty} w^{(\mathrm{int})}(\eta) = -\frac{32}{3} \ ; \qquad y^\dagger = 1 \ , \tag{69b}$$

$$\lim_{\eta \to +\infty} w^{(\mathrm{ext})}(\eta) = -\frac{64}{(y^\dagger - 1)^3} \left[(y^\dagger)^2 - 1 - 2y^\dagger \ln y^\dagger \right]$$
$$y^\dagger \neq 1 \ , \tag{70a}$$

$$\lim_{\eta \to +\infty} w^{(\mathrm{ext})}(\eta) = -\frac{64}{3} \ ; \qquad y^\dagger = 1 \ , \tag{70b}$$

where $\Xi_i = \Xi_N$, $\Xi_j = \Xi_H$ while the contrary holds with regard to Eqs. (67)-(68). Using Eq. (24), Eqs. (46)-(47), Eqs. (51)-(52), and Eqs. (58)-(70) the actual HN (AHN) and NH (ANH) macrogas equation of state in the special situation under discussion, is obtained from the particularization of Eqs. (30) to the case of interest.

The ideal situation, where the interaction terms are omitted, is obtained using Eqs. (32) instead of Eq. (30). More specifically, the ideal HN (IHN) and NH (INH) macrogas equation of state is obtained from the combination of Eq. (30e), Eq. (32b), Eqs. (46)-(47) and Eqs. (58)-(59). The result is:

$$X_{\mathrm{p}} = \frac{1}{3} \frac{4 + \Xi_H}{\Xi_H}$$
$$\times \frac{[(1 + \Xi_N) \ln(1 + \Xi_N) - \Xi_N]^2}{\Xi_N(2 + \Xi_N) - 2(1 + \Xi_N) \ln(1 + \Xi_N)} \frac{X_{\mathrm{T}}}{X_{\mathrm{V}}}, \tag{71}$$

36

which represents a hyperbola with different axes for fixed X_T. In the limit of infinite extension $\Xi \to +\infty$ both the left and right-hand side of Eq. (71) diverge but a different equation of state may be derived starting from Eq. (30d) and Eq. (32a), following a similar procedure. The result is:

$$X_\mathrm{p}^\dagger = \frac{1}{3} \frac{\Xi_H^3(4 + \Xi_H)}{(1 + \Xi_H)^4}$$

$$\times \frac{(1 + \Xi_N)^2}{\Xi_N(2 + \Xi_N) - 2(1 + \Xi_N)\ln(1 + \Xi_N)} \frac{X_\mathrm{T}^\dagger}{X_\mathrm{V}^\dagger}, \quad (72)$$

which also represents a hyperbola with different axes for fixed $X_\mathrm{T}^\dagger$.

Macroisothermal curves ($\not{X}_\mathrm{p} = X_\mathrm{p}/X_{p_c}$ vs. $\not{X}_\mathrm{V} = X_\mathrm{V}/X_{V_c}$) related to IHN/INH (tidal potential energy excluded) and AHN/ANH (tidal potential energy included) macrogases, are plotted in Fig. 10, left and right panels, for different values of scaled truncation radii (Ξ_i, Ξ_j) labelled on each panel, and same values of the reduced macrotemperature $\not{X}_\mathrm{T} = X_\mathrm{T}/X_{T_c} = 0.90, 0.95, 1.00, 1.05, 1.10, 1.15$, from bottom to top.
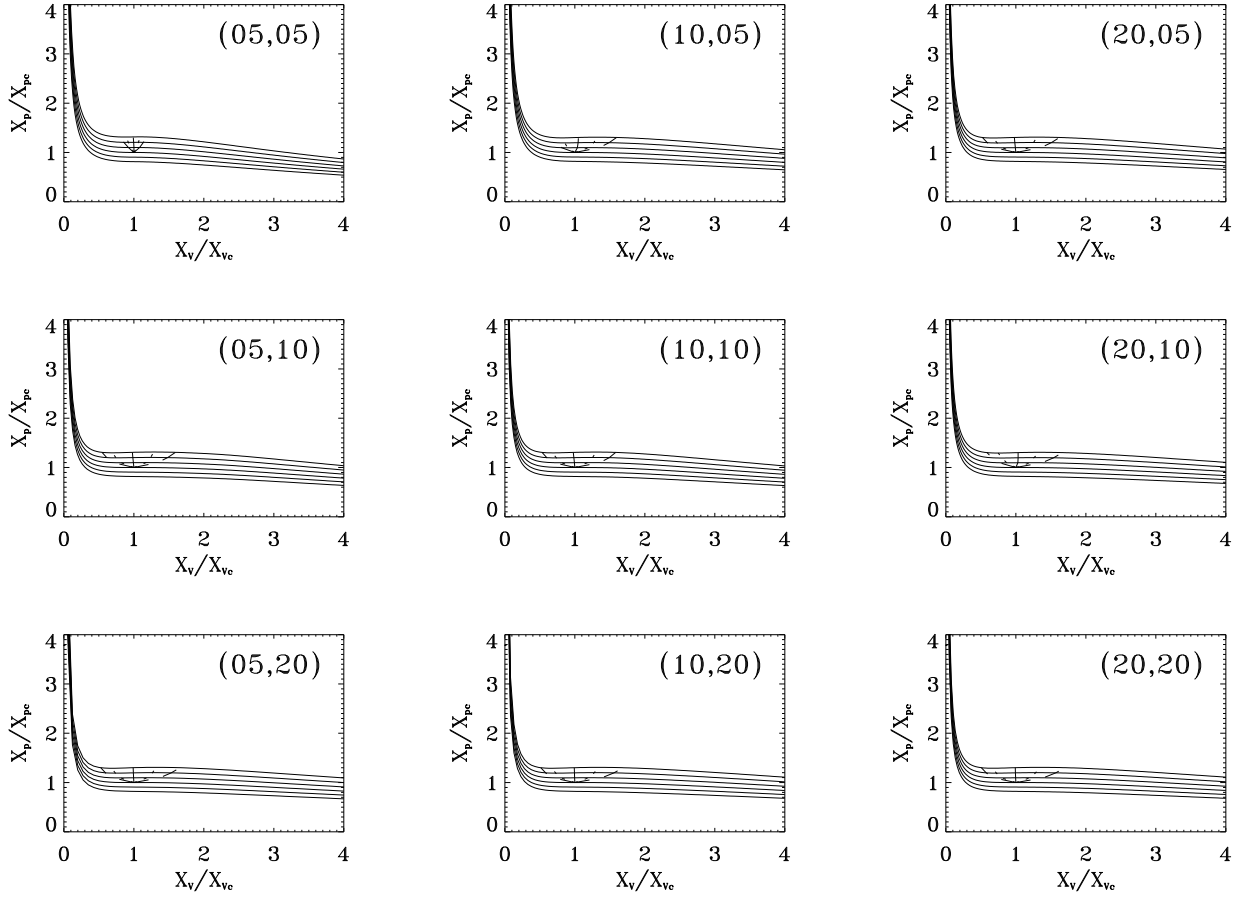

Fig. 11. *AHN/ANH macroisothermal curves ($\not{X}_\mathrm{p} = X_\mathrm{p}/X_{p_c}$ vs. $\not{X}_\mathrm{V} = X_\mathrm{V}/X_{V_c}$) for different choices of scaled truncation radii (Ξ_i, Ξ_j) labelled on each panel. Macroisothermal curves (from bottom to top) correspond to $\not{X}_\mathrm{T} = X_\mathrm{T}/X_{T_c} = 0.90, 0.95, 1.00, 1.05, 1.10, 1.15$. The limit $(\Xi_i, \Xi_j) \to (+\infty, +\infty)$ makes only little changes. RHN/RNH macroisothermal curves, when different from their AHN/ANH counterparts, lie within the larger reversed bell-shaped region in each panel. The loci of intersections between AHN/ANH and RHN/RNH macroisothermal curves are represented as trifid curves, where the left branch corresponds to $\not{X}_{V_\mathrm{A}}$, the right branch to $\not{X}_{V_\mathrm{E}}$, and the middle branch to $\not{X}_{V_\mathrm{C}}$. The critical point is the common origin. The loci of AHN/ANH macroisothermal curve extremum points are represented as dotted curves starting from the critical point, where the left branch corresponds to minimum points and the right branch to maximum points.*

The limit $(\Xi_i, \Xi_j) \to (+\infty, +\infty)$ makes only little changes. Owing to Eq. (22a) and Eq. (31), $X_V^\dagger = X_V y^\dagger/y$ and $X_p^\dagger = X_p(m^\dagger/m)^2$, which implies $\cancel{X}_V^\dagger = \cancel{X}_V$ and $\cancel{X}_p^\dagger = \cancel{X}_p$. The comparison with ideal and VDW gases plotted in Fig. 1, shows a similar but reversed trend. More specifically, extremum points occur above instead of below the critical macroisothermal curve. A complete analogy can be obtained using the transformations, $X_V \to 1/X_V$, $X_p \to 1/X_p$, $X_T \to 1/X_T$.

The existence of a phase transition moving along a selected macroisothermal curve, where the path is a horizontal line instead of a curve including the extremum points, must necessarily be assumed as a working hypothesis due to analogy between VDW isothermal curves and AHN/ANH macroisothermal curves. As in the case of UU macrogases, AHN/ANH macroisothermal curves must be numerically determined following the same procedure outlined in Subsection 3.1. The loci of AHN/ANH macroisothermal curves plotted in Fig. 10 (right panels), are represented in Fig. 11.

The loci of intersections between AHN/ANH and real HN/NH (RHN/RNH) macroisothermal curves are represented in Fig. 11 as trifid curves, where the left branch corresponds to $\cancel{X}_{V_A}$, the right branch to $\cancel{X}_{V_E}$, and the middle branch to $\cancel{X}_{V_C}$. The critical point is the common starting point. The loci of AHN/ANH macroisothermal curve extremum points are represented in Fig. 11 as dotted curves starting from the critical point where the left branch corresponds to minimum points and the right branch to maximum points. The RHN/RNH macroisothermal curves, when different from their AHN/ANH counterparts, lie within the larger bell-shaped regions. The limit $(\Xi_i, \Xi_j) \to (+\infty, +\infty)$ makes only little changes. Values of parameters, $\cancel{X}_T$, $\cancel{X}_{V_A}$, $\cancel{X}_{V_B}$, $\cancel{X}_{V_C}$, $\cancel{X}_{V_D}$, $\cancel{X}_{V_E}$, $\cancel{X}_{p_B}$, $\cancel{X}_{p_C}$, $\cancel{X}_{p_D}$, are listed in Table 3 within the range $1.00 < \cancel{X}_T \le 1.15$ using a step $\Delta \cancel{X}_T = 0.01$ in the limit $(\Xi_i, \Xi_j) \to (+\infty, +\infty)$. The AHN/ANH macroisothermal curves are plotted in Fig. 12 for scaled truncation radii (Ξ_i, Ξ_j) as in Fig. 11, with regard to the special case $\cancel{X}_T = 1.15$. The limit $(\Xi_i, \Xi_j) \to (+\infty, +\infty)$ makes only little changes, as shown by comparison with the dashed curve.

Fig. 12. *AHN/ANH macroisothermal curves ($\cancel{X}_p = X_p/X_{p_c}$ vs. $\cancel{X}_V = X_V/X_{V_c}$) for scaled truncation radii (Ξ_i, Ξ_j) as in Fig. 11, with regard to the special case $\cancel{X}_T = X_T/X_{T_c} = 1.15$. The limit $(\Xi_i, \Xi_j) \to (+\infty, +\infty)$ makes only little changes, as shown by comparison with the dashed curve.*
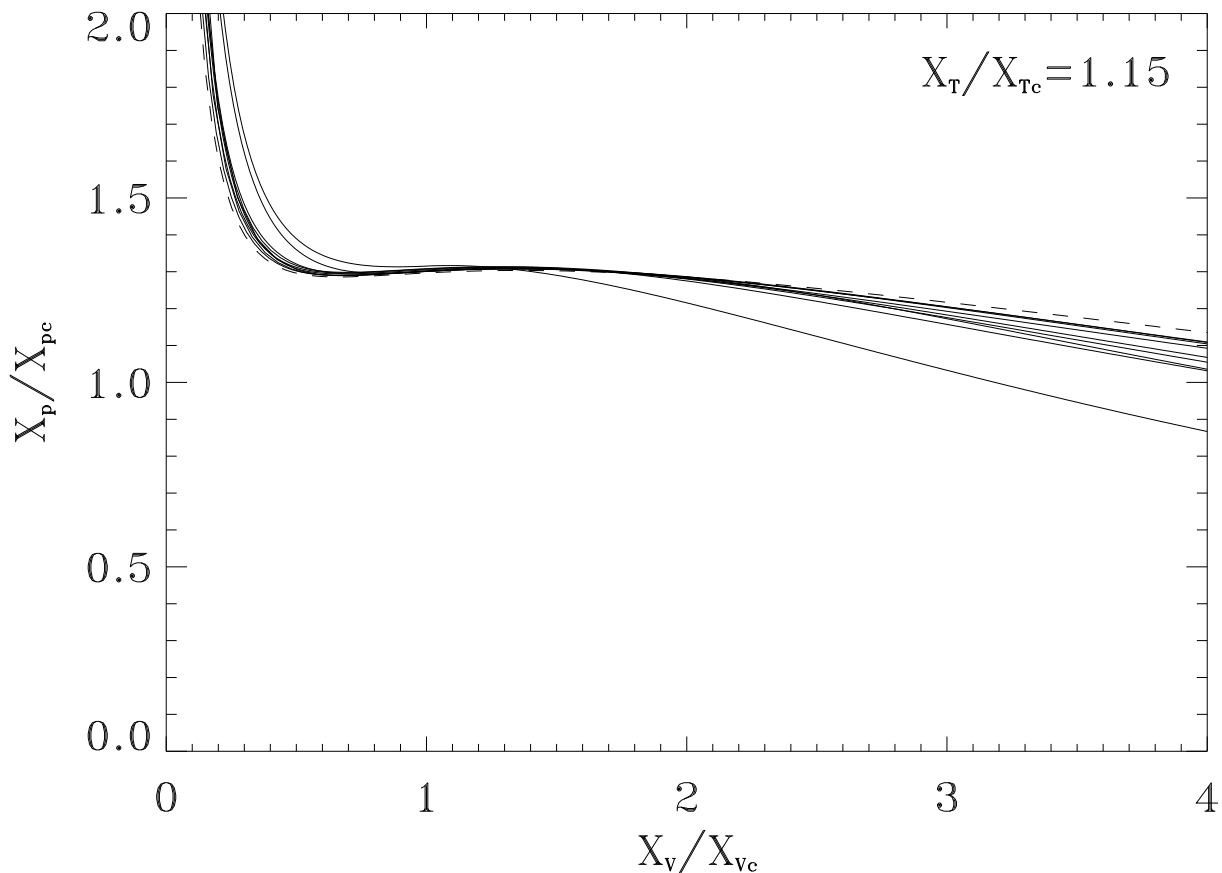
Table 3. Values of parameters X_T, X_{V_A}, X_{V_B}, X_{V_C}, X_{V_D}, X_{V_E}, X_{p_B}, X_{p_C}, X_{p_D} within the range $1.01 \leq X_T \leq 1.15$ using a step $\Delta X_T = 0.01$. All values equal unity at the critical point. Results are related to infinitely extended configurations $(\Xi_i, \Xi_j) \to (+\infty, +\infty)$. Index captions: A, C, E - intersections between AHN/ANH and RHN/RNH macroisothermal curves; B - extremum point of minimum; D - extremum point of maximum. Extremum points are related to AHN/ANH macroisothermal curves while their RHN/RNH counterparts are flat within the range $X_{V_A} \leq X_V \leq X_{V_E}$. For aesthetical reasons, 01 on head columns stands for unity.

X_T	$10X_{V_A}$	$10X_{V_B}$	$10X_{V_C}$	$01X_{V_D}$	$01X_{V_E}$	$01X_{p_B}$	$01X_{p_C}$	$01X_{p_D}$
1.01	8.4036	9.0357	9.9949	1.0976	1.1768	1.1085	1.0186	1.0187
1.02	7.8103	8.6548	9.9935	1.1372	1.2535	1.0370	1.0374	1.0377
1.03	7.3771	8.3678	9.9918	1.1675	1.3139	1.0555	1.0563	1.0570
1.04	7.0273	8.1303	9.9903	1.1929	1.3656	1.0742	1.0754	1.0764
1.05	6.7309	7.9247	9.9888	1.2151	1.4118	1.0929	1.0947	1.0961
1.06	6.4724	7.7420	9.9874	1.2347	1.4540	1.1118	1.1142	1.1159
1.07	6.2427	7.5768	9.9859	1.2527	1.4930	1.1307	1.1338	1.1360
1.08	6.0356	7.4256	9.9844	1.2694	1.5295	1.1498	1.1535	1.1562
1.09	5.8488	7.2872	9.9830	1.2845	1.5637	1.1687	1.1733	1.1765
1.10	5.6738	7.1558	9.9815	1.2991	1.5967	1.1881	1.1936	1.1974
1.11	5.5137	7.0340	9.9797	1.3126	1.6279	1.2074	1.2139	1.2182
1.12	5.3647	6.9194	9.9785	1.3254	1.6577	1.2269	1.2343	1.2392
1.13	5.2256	6.8111	9.9770	1.3376	1.6864	1.2464	1.2549	1.2605
1.14	5.0952	6.7084	9.9754	1.3491	1.7139	1.2661	1.2757	1.2819
1.15	4.9726	6.6108	9.9737	1.3601	1.7406	1.2858	1.2967	1.3035

Table 4. Values of the scaling fractional mass $m^\dagger$, the fractional mass m, the scaling fractional radius $y^\dagger$, the fractional truncation radius y, and the fractional energy ϕ, related to the critical point i.e. the horizontal inflexion point on the critical macroisothermal curve, for selected scaled truncation radii, (Ξ_i, Ξ_j), of HN/NH density profiles. In absence of truncation radius $(\Xi_i, \Xi_j) \to (+\infty, +\infty)$ the results are independent of $y/y^\dagger = \Xi_j/\Xi_i$.

(Ξ_i, Ξ_j)	$m^\dagger$	m	$y^\dagger$	y	φ
(05,05)	02.57	03.54	1.01	1.01	03.66
(05,10)	04.41	09.45	1.04	2.08	09.16
(05,20)	05.14	15.47	1.14	4.57	13.42
(10,05)	05.84	06.77	1.88	0.94	07.33
(10,10)	06.36	11.45	1.38	1.38	11.47
(10,20)	07.24	18.32	1.50	3.00	16.46
(20,05)	09.40	09.93	2.13	0.53	11.30
(20,10)	08.44	13.85	1.92	0.96	14.35
(20,20)	09.10	20.99	1.75	1.75	19.49
(∞,∞)	12.40	$+\infty$	2.06	$\dots$	35.82

Values of parameters $m^\dagger$, m, $y^\dagger$, y, ϕ, related to the critical macroisothermal curve, for selected scaled truncation radii (Ξ_i, Ξ_j) are listed in Table 4.

A better method has been used with respect to an earlier attempt (CV08) yielding improved results with the occurrence of the critical macroisothermal curve in all cases. In absence of truncation radius $(\Xi_i, \Xi_j) \to (+\infty, +\infty)$ small differences appear in the results probably due to (i) the divergence of the fractional mass, $m \to +\infty$, as $\Xi_N \to +\infty$, and (ii) numerical calculations have been performed taking $\Xi \gtrsim 10^{10}$. Related results listed in Table 4 may be considered as weighted means.

4. APPLICATION TO ELLIPTICAL GALAXIES

The luminosity-weighted second moment of the line-of-sight velocity distribution within the half-light radius has recently been determined for samples of early-type galaxies, using integral-field spectroscopy such as SAURON (S IV; S X). Compared to the central velocity dispersion, which was sometimes used before, the above mentioned quantity has the advantage of being only weakly dependent on the details of the aperture used. In addition, it is an approximation to the second velocity moment

Table 5. Data related to a sample ($N = 16$) of elliptical galaxies extracted from larger samples of early-type galaxies investigated within the SAURON project (S IV, $N = 25$; S X, $N = 48$), which are used in the current paper. Column captions: (1) NGC number; (2) effective (half-light) radius, R_e, measured in the I band (S IV); (3) ratio between maximum radius, R_{max}, and effective radius, R_e (S IV); (4) total observed I band galaxy magnitude (S IV); (5) mass-luminosity ratio of the stellar population (S IV); (6) galaxy distance modulus (hats avoid confusion with the fractional mass, m, and the total mass, M) (S IV); (7) luminosity-weighted average ellipticity, $\hat{e}_\perp$, on a plane perpendicular to the line of sight (S X); (8) luminosity-weighted squared mean velocity component, parallel to the line of sight (S X); (9) luminosity-weighted squared velocity dispersion, parallel to the line of sight (S X); (10) ratio between the square root luminosity-weighted squared mean velocity component and dispersion velocity component parallel to the line of sight (S X); (11) kinematic classification (F - fast rotator; S - slow rotator) (S X). For further details refer to the text.

NGC	R_e	$\frac{R_{max}}{R_e}$	I_T	$\frac{M_i}{L}$	$\hat{m} - \hat{M}$	$< \hat{e}_\perp >$	$< \widetilde{v}_\parallel^2 >^{\frac{1}{2}}$	$< \sigma_\parallel^2 >^{\frac{1}{2}}$	$\frac{<\widetilde{v}_\parallel^2>^{\frac{1}{2}}}{<\sigma_\parallel^2>^{\frac{1}{2}}}$	KC
	(arcsec)		(mag)	(I band)	(mag)		(km/s)	(km/s)		
0821	039.0	0.62	09.47	2.60	31.85	0.40	048	182	0.26	F
2974	024.0	1.04	09.43	2.34	31.60	0.37	127	180	0.70	F
3377	038.0	0.53	08.98	1.75	30.19	0.46	057	117	0.49	F
3379	042.0	0.67	08.03	3.08	30.06	0.08	028	198	0.14	F
3608	041.0	0.49	09.40	2.57	31.74	0.18	008	179	0.05	S
4278	032.0	0.82	08.83	3.05	30.97	0.12	044	228	0.19	F
4374	071.0	0.43	07.69	3.08	31.26	0.15	007	282	0.03	S
4458	027.0	0.74	10.68	2.27	31.12	0.12	010	084	0.12	S
4473	027.0	0.92	08.94	2.88	30.92	0.41	041	188	0.22	F
4486	105.0	0.29	07.23	3.33	30.97	0.04	007	306	0.02	S
4552	032.0	0.63	08.54	3.35	30.87	0.04	013	257	0.05	S
4621	046.0	0.56	08.41	3.12	31.25	0.34	052	207	0.23	F
4660	011.0	1.83	09.96	2.96	30.48	0.44	079	163	0.49	F
5813	052.0	0.53	09.12	2.97	32.48	0.15	032	223	0.14	S
5845	004.6	4.45	11.10	2.96	32.01	0.35	081	226	0.36	F
5846	081.0	0.29	08.41	3.33	31.92	0.07	007	240	0.03	S

which appears in the virial equations (e.g. Binney and Tremaine 1987, Chap. 4, §4.3). In other words, it may be conceived as a rms mass-weighted velocity, with a weak dependence on the features of the orbital distribution. For further details refer to the parent papers (S IV; S X).

An application of the current model to SAURON sample objects can be performed along the following steps: (i) Select SAURON data of interest; (ii) Calculate parameters appearing in the virial equations; (iii) Make a correspondence between model galaxies and sample objects; (iv) Represent model galaxies as points on the $(O\hat{X}_V\hat{X}_p)$ plane.

4.1. Data selection

The sample used (CV08, $N = 16$) is made of elliptical galaxies extracted from richer samples of early-type galaxies investigated within the SAURON project (S IV, $N = 25$; S X, $N = 48$). The selection has been restricted to elliptical galaxies common to the above mentioned samples for two main reasons, namely (i) the current model best applies to elliptical galaxies and their hosting haloes, and (ii) some physical parameters of interest are listed in either S IV or S X. The whole data set needed for the appli-

cation is shown in Table 5. For further details refer to the parent papers (S IV, columns 2-6; S X, columns 7-11).

Values to be actually used in the application are related to: the effective (half-light) radius, R_e (S IV); the total observed I band galaxy magnitude I_T (S IV); the mass-luminosity ratio of the stellar population, M_i/L (S IV); the galaxy distance modulus, $\hat{m} - \hat{M}$ (hats avoid confusion with the fractional mass, $m = M_j/M_i$, and the total mass $M = M_i + M_j$) (S IV); the luminosity-weighted average ellipticity $\hat{e}_\perp$ on a plane perpendicular to the line of sight, within either an isophote enclosing an area $\hat{A} = \pi R_e^2$, or the largest isophote fully contained within the SAURON field, whichever is smaller (S X); the luminosity-weighted squared mean velocity component parallel to the line of sight, within either an ellipse of area $\hat{A}$, ellipticity $\hat{e}_\perp$, and related position angle, or the largest similar ellipse fully contained within the SAURON field, whichever is smaller (S X); the luminosity-weighted squared velocity dispersion parallel to the line of sight within either an ellipse of area $\hat{A}$, ellipticity $\hat{e}_\perp$, and related position angle, or the largest similar ellipse fully contained within the SAURON field, whichever is smaller (S X).

Parameters listed to gain further insight even if not used in the application are: the ratio between the maximum radius $R_{\max}$ sampled by the kinematical observations, and effective radius R_e (S IV); the ratio between square root luminosity-weighted squared mean velocity component and dispersion velocity component parallel to the line of sight (S X); the kinematic classification (F - fast rotator; S - slow rotator) (S X).

For further details refer to the parent papers (S IV; S X) and an earlier attempt (Binney 2005).

4.2. Determination of model parameters

With regard to the stellar subsystem, two model parameters can directly be inferred from the data (CV08). More specifically, stellar masses are deduced from luminosities and mass-luminosity ratios (in I band) as $M_i/\mathrm{M}_{10} = (L/\mathrm{L}_\odot)[(M_i/L)/(10^{10}\mathrm{m}_\odot/\mathrm{L}_\odot)]$; $L/\mathrm{L}_\odot = \exp_{10}\{-0.4[I_T - (\hat{m} - \hat{M}) - 4.11]\}$; and scaling radii are calculated from effective radii (in arcsec) and distances, as $r_i^\dagger/\mathrm{kpc} = (R_e/\mathrm{kpc})/1.81$; $R_e/\mathrm{kpc} = [(R_e/\mathrm{arcsec})(d/\mathrm{Mpc})]/206.265$; $d/\mathrm{Mpc} = \exp_{10}[(\hat{m} - \hat{M})/5 - 5]$; the factor 1.81 is related to an assumed H density profile for the inner subsystem, and the factor 206.265 is related to the choice of measure units (CV08). For further details refer to the parent paper (S IV).

Two additional parameters can be inferred by fitting the data with dynamical models. More specifically, the inclination angle i is deduced from the best fitting two-integral Jeans model (S IV), and the anisotropy parameter δ is determined from the solution of the dynamical models supposed to be axisymmetric (S X). In fact, fast rotators show evidence of large anisotropy and axial symmetry while slow rotators appear to be nearly isotropic and moderately triaxial. For further details refer to the parent paper (S X).

The intrinsic axis ratio ϵ is deduced from the computed inclination under the assumption of axisymmetric configurations (S X) using the relation (Binney and Tremaine 1987, Chap. 4, §4.3):

$$1 - \epsilon^2 = \frac{1 - \epsilon_{\mathrm{obs}}^2}{\sin^2 i} \quad , \qquad (73)$$

where ϵ_{obs} is the observed axis ratio related to an inclination angle i between the symmetry axis and the line of sight ($i = 90°$ for edge-on configurations).

The mass-weighted mean square velocity component and dispersion velocity component parallel to the line of sight, for a galaxy observed (obs) at an inclination angle i under the assumption of axisymmetric ($a_1 = a_2$) and isotropic on the equatorial plane ($\sigma_{11} = \sigma_{22}$) configurations (S X), are related to their edge-on (edo) counterparts as (Binney and Tremaine 1987, Chap. 4, §4.3):

$$[<\widetilde{v}_\parallel^2>^{1/2}]_{\mathrm{obs}} = [<\widetilde{v}_\parallel^2>^{1/2}]_{\mathrm{edo}} \sin i \quad , \qquad (74)$$

$$[<\sigma_\parallel^2>^{1/2}]_{\mathrm{obs}} = [<\sigma_\parallel^2>^{1/2}]_{\mathrm{edo}}(1 - \delta\cos^2 i)^{1/2}, \quad (75)$$

and the intrinsic mean rotational velocity and velocity dispersion are expressed as:

$$<\widetilde{v_{\phi\phi}}^2>^{1/2} = \sqrt{2}[<\widetilde{v}_\parallel^2>^{1/2}]_{\mathrm{edo}}$$
$$= \frac{\sqrt{2}}{\sin i}[<\widetilde{v}_\parallel^2>^{1/2}]_{\mathrm{obs}} \quad , \qquad (76)$$

$$<\sigma^2>^{1/2} = (<\sigma_{11}^2> + <\sigma_{22}^2> + <\sigma_{33}^2>)^{1/2}$$
$$= \{2[<\sigma_\parallel^2>]_{\mathrm{edo}} + (1 - \delta)[<\sigma_\parallel^2>]_{\mathrm{edo}}\}^{1/2}$$
$$= (3 - \delta)^{1/2}[<\sigma_\parallel^2>^{1/2}]_{\mathrm{edo}} =$$
$$= \left(\frac{3 - \delta}{1 - \delta\cos^2 i}\right)^{1/2}[<\sigma_\parallel^2>^{1/2}]_{\mathrm{obs}} \quad , \quad (77)$$

in terms of observed quantities, where:

$$\delta = 1 - \frac{<\sigma_{33}^2>}{<\sigma_{11}^2>} = 1 - \frac{<\sigma_{33}^2>}{<\sigma_{22}^2>} \quad , \qquad (78)$$

by definition (e.g. Binney 2005).

4.3. Model galaxies vs. sample objects

The kinetic energy of the stellar subsystem is:

$$(E_i)_{\mathrm{kin}} = \frac{1}{2}M_i\left\{<(\widetilde{v_{\phi\phi}})_i^2> + <\sigma_i^2>\right\} \quad , \qquad (79)$$

and the combination of Eq. (15), Eqs. (20)-(21), Eqs. (23)-(24), and Eq. (79) yields:

$$M_i\left\{<(\widetilde{v_{\phi\phi}})_i^2> + <\sigma_i^2>\right\}$$
$$= \frac{(\nu_i)_{\mathrm{sel}}}{[(\nu_i)_{\mathrm{mas}}]^2}\frac{G(M_i)^2}{(a_i^\dagger)_1}B + \frac{(\nu_{ij})_{\mathrm{tid}}}{[(\nu_i)_{\mathrm{mas}}]^2}\frac{G(M_i)^2}{(a_i\dagger)_1}B \quad , \quad (80)$$

which, after some algebra, takes the form:

$$\frac{<\sigma_i^2>(a_i^\dagger)_1}{GM_i}\frac{1}{B}\left\{\frac{<(\widetilde{v_{\phi\phi}})_i^2>}{<\sigma_i^2>} + 1\right\}$$
$$= \frac{(\nu_i)_{\mathrm{sel}} + (\nu_{ij})_{\mathrm{tid}}}{[(\nu_i)_{\mathrm{mas}}]^2} \quad , \qquad (81)$$

where, for an inner H density profile, the scaling radius $r_i^\dagger = (a_i^\dagger)_1$ may be chosen as:

$$r_i^\dagger = \frac{R_e}{1.81} \; ; \; M_i(r_i^\dagger) = \frac{1}{4}M_i \; ; \; M_i(R_e) = \frac{1}{2}M_i \; , \quad (82)$$

and the shape factor B reads (e.g. Chandrasekhar 1969, Chap. 3 §§17, 22, Caimmi 2009):

$$B = 2\frac{\arcsin\sqrt{1 - \epsilon^2}}{\sqrt{1 - \epsilon^2}}$$
$$= 2\frac{\arcsin\dfrac{\sqrt{1 - (1 - <\hat{e}_\perp>)^2}}{\sin i}}{\dfrac{\sqrt{1 - (1 - <\hat{e}_\perp>)^2}}{\sin i}} \quad , \qquad (83)$$

41

for axisymmetric configurations where the last equality is due to Eq. (73) and the definition of ellipticity is $\hat{e} = 1 - \epsilon$.

The combination of Eqs. (76)-(77), Eq. (79), and Eqs. (81)-(82) yields:

$$\frac{[<\sigma_\parallel^2>]_{\rm obs}}{2GM_i(R_e)} \frac{R_e}{1.81} \frac{1}{B}$$

$$\times \left\{ \frac{2}{\sin^2 i} \frac{[<\widetilde{v}_\parallel^2>]_{\rm obs}}{[<\sigma_\parallel^2>]_{\rm obs}} + \frac{3-\delta}{1-\delta\cos^2 i} \right\} = c_{ij} \quad , \text{ (84a)}$$

$$c_{ij} = \frac{(\nu_i)_{\rm sel} + (\nu_{ij})_{\rm tid}}{[(\nu_i)_{\rm mas}]^2} \quad , \qquad\qquad \text{(84b)}$$

where the left-hand side of Eq. (84a) is expressed in terms of quantities which are deduced from either observations or fitting with dynamic models, and then may be determined for an assigned sample object. Conversely, the right-hand side of Eq. (84a) depends on the selected density profiles, and then may be determined for an assigned model galaxy. In this view, Eq. (84a) may be read as a correspondence between sample objects (left) and model galaxies (right).

The dimensionless energy c_{ij}, defined by Eq. (84b), depends on four variables via Eqs. (20)-(25): the scaled truncation radii, Ξ_i, Ξ_j, the fractional mass $m^\dagger$ (or m), and the fractional radius $y^\dagger$ (or y).

4.4. Model galaxies on the $(O\!\!\!/\,X_V\,X_p)$ plane

For assigned density profiles and scaled truncation radii Ξ_i, Ξ_j two unknowns remain: the fractional mass $m^\dagger$ (or m) and the fractional radius $y^\dagger$ (or y). The combination of Eq. (24a) and Eq. (84b) yields:

$$w^{(\rm ext)}(\eta) = \frac{8}{9} \frac{1}{m^\dagger} \left\{ (\nu_i)_{\rm sel} - c_{ij}[(\nu_i)_{\rm mas}]^2 \right\} \quad , \quad \text{(85)}$$

where the function $w^{(\rm ext)}$ depends on Ξ_i and $y^\dagger$, conformably to Eq. (20c), Eq. (24d), and Eq. (25b). In the case under discussion, Eq. (85) may be conceived as a link between the unknowns $m^\dagger$ and $y^\dagger$. At this stage, one additional relation is needed (CV08).

The mere existence of a fundamental plane (Djorgovski and Davis 1987, Dressler et al. 1987) indicates that structural properties in elliptical galaxies span a narrow range, suggesting that some self-regulating mechanism must be at work during formation and evolution. In particular, projected light profiles from elliptical galaxies exhibit large degree of homogeneity and may well be fitted by the $r^{1/4}$ de Vaucouleurs law. Accordingly, a narrow range may safely be expected also for fractional masses of elliptical galaxies and the assumption $m = \rm const$ appears to be a viable approximation. This is the reason for which the sample used ($N = 16$) is made of only elliptical galaxies extracted from larger samples ($N = 25$; $N = 48$) of early-type galaxies investigated within the SAURON project (S IV; S X).

Then, the fractional radius $y^\dagger$ (or y) remains as the sole unknown which can be determined by solving Eq. (85) with numerical techniques. If no solution exists, no model galaxy corresponds to the selected sample object or, in other words, the related density profiles provide no fit to the data and some input value has to be changed.

Values of parameters needed for representing model galaxies on the $(O\!\!\!/\,X_V\,X_p)$ plane are listed in Table 5: the galaxy stellar mass M_i; the galaxy scaling radius $r_i^\dagger$; the inclination angle i, of the best fitting two-integral Jeans model (S IV); the anisotropy parameter δ, determined from the solution of the dynamic models, supposed to be axisymmetric ($a_1 = a_2$) and isotropic on the equatorial plane ($\sigma_{11} = \sigma_{22}$) (S X); the intrinsic axis ratio ϵ, deduced from the computed inclination, under the assumption of axisymmetric configurations (S X); the dimensionless energy c_{ij}, defined by Eqs. (84). The kinematic classification is listed again to get more insight.

The galaxy stellar mass within the effective radius is calculated as:

$$\frac{M_i}{\rm M_{10}} = \frac{L}{\rm L_\odot} \frac{M_i/L}{10^{10}\rm m_\odot/L_\odot} \quad , \qquad\qquad \text{(86a)}$$

$$\frac{L}{\rm L_\odot} = \exp_{10}\{-0.4[I_T - (\hat{m} - \hat{M}) - 4.11]\} \quad \text{(86b)}$$

and the galaxy effective radius is calculated as:

$$\frac{R_e}{\rm kpc} = \frac{R_e}{\rm arcsec} \frac{1}{206.265} \frac{d}{\rm Mpc} \quad , \qquad \text{(87a)}$$

$$\frac{d}{\rm Mpc} = \exp_{10}\left[\frac{\hat{m} - \hat{M}}{5} - 5 \right] \quad , \qquad \text{(87b)}$$

where the factor 206.265 is related to the choice of measure units. For further details refer to an earlier attempt (CV08).

The values of the reduced variables X_V, X_p, X_T are determined via Eq. (27) and Eq. (30e). Both HH and HN macrogases have been considered for the following values of parameters. Scaled truncation radii (both finite or infinite): $(\Xi_i, \Xi_j) = (k_i, k_j)$; $k_i = 5, 10, 20, +\infty$; $k_j = 5, 10, 20, +\infty$. Fractional masses: $m = 10, 20$. Under the working hypothesis of an analogy between VDW gases and macrogases, the $(O\!\!\!/\,X_V\,X_p)$ plane may be divided into three parts: (i) a reversed bell-shaped region where two phases, gas and stars, coexist and the lower point coincides with the critical point (hereafter quoted as the GS region); (ii) a region limited by the left boundary of the reversed bell-shaped region and the rising side of the critical macroisothermal curve, both branching off from the critical point where only stars are present (hereafter quoted as the S region); (iii) a region limited by the right boundary of the reversed bell-shaped region and the rising side of the critical macroisothermal curve, both branching off from the critical point, and the coordinate axes, where only

Table 6. Parameters calculated from the data listed in Table 5 for a sample ($N = 16$) of elliptical galaxies extracted from larger samples of early-type galaxies investigated within the SAURON project (S IV, $N = 25$; S X, $N = 48$) which are used in the current paper. Column captions: (1) NGC number; (2) Galaxy stellar mass deduced from luminosities and mass-luminosity ratios (in I band) (S IV); (3) Galaxy scaling radius (CV08); (4) Inclination angle of the best fitting two-integral Jeans model (S IV); (5) Anisotropy parameter, determined from the solution of the dynamic models, supposed to be axisymmetric (S X); (6) Intrinsic axis ratio, deduced from the computed inclination, under the assumption of axisymmetric configurations (S X); (7) Dimensionless energy; (8) Kinematic classification (F - fast rotator; S - slow rotator) (S X). For further details refer to the text.

NGC	M_i (M_{10})	$r_i^{\dagger}$ (kpc)	i (°)	δ_i	ϵ_i	c_{ij}	KC
0821	10.26	2.45	90	0.20	0.60	0.23	F
2974	07.61	1.34	57	0.24	0.38	0.23	F
3377	02.35	1.11	90	0.25	0.54	0.20	F
3379	08.80	1.16	90	0.03	0.92	0.18	F
3608	09.77	2.45	90	0.13	0.82	0.25	S
4278	09.64	1.34	45	0.18	0.74	0.25	F
4374	36.35	3.40	90	0.08	0.85	0.24	S
4458	01.50	1.21	90	0.09	0.88	0.19	S
4473	07.86	1.10	73	0.34	0.54	0.14	F
4486	45.97	4.40	90	0.00	0.96	0.31	S
4552	12.62	1.28	90	0.02	0.96	0.23	S
4621	18.80	2.19	90	0.18	0.66	0.15	F
4660	02.11	0.37	70	0.30	0.47	0.15	F
5813	28.89	4.36	90	0.08	0.85	0.25	S
5845	03.02	0.31	90	0.15	0.65	0.17	F
5846	37.19	5.25	90	0.01	0.93	0.28	S

gas is present (hereafter quoted as the G region). If the density profiles are only slightly affected in time, the evolution of a galaxy on the $(\mathsf{O}\mathchar'26\mkern-10mu\chi_\mathrm{V}\mathchar'26\mkern-10mu\chi_\mathrm{p})$ plane is represented by a track starting from the G region and ending within the GS or the S region. The critical point is the sole which is common to the three regions.

The position of a model galaxy on the $(\mathsf{O}\mathchar'26\mkern-10mu\chi_\mathrm{V}\mathchar'26\mkern-10mu\chi_\mathrm{p})$ plane is affected by errors of different kind, due to: (1) scatter around mean values listed in Table 5; (2) scatter in fitting observed to model density profiles; (3) uncertainty on the determination of the critical point. The third contribution may safely be neglected with respect to the other ones. Values related to the first contribution are not completely found in literature (to the knowledge of the author). The second contribution could be determined using fitting procedures, provided light distributions are available and light traces stellar mass in elliptical galaxies. In summary, error calculation on the position of sample objects on the $(\mathsf{O}\mathchar'26\mkern-10mu\chi_\mathrm{V}\mathchar'26\mkern-10mu\chi_\mathrm{p})$ plane would be cumbersome and, perhaps, of little meaning.

A notable simplification can be attained if model galaxies instead of sample objects are considered in dealing with only errors of the first kind mentioned above. For a fixed fractional mass m, the uncertainty on $\mathchar'26\mkern-10mu\chi_\mathrm{p} = (m/m_\mathrm{c})^2$ is negligible with respect to $\mathchar'26\mkern-10mu\chi_\mathrm{V} = y_\mathrm{c}/y$ which is determined by solving Eq. (84a) for assigned density profiles. The combination of Eqs. (82)-(83), and Eq. (84b) yields an expression of the dimensionless energy c_{ij}, in terms of

observables listed in Table 5, as:

$$c_{ij} = \frac{1}{1163.335} \frac{1}{G} \frac{\zeta_4}{\zeta_5} \exp_{10}[0.4\zeta_6 - 0.2\zeta_7 - 6.644]$$

$$\times \frac{[1 - (1 - \zeta_1)^2]^{1/2}/\sin i}{\arcsin\{[1 - (1 - \zeta_1)^2]^{1/2}/\sin i\}}$$

$$\times \left\{ \frac{2\zeta_2^2}{\sin^2 i} + \frac{(3 - \delta)\zeta_3^2}{1 - \delta \cos^2 i} \right\}, \qquad (88a)$$

$$\zeta_1 = <\hat{e}_\perp> \quad ; \quad \zeta_2 = \left[<\widetilde{v}_\parallel^2>^{1/2}\right]_{\mathrm{obs}};$$

$$\zeta_3 = \left[<\sigma_\parallel^2>^{1/2}\right]_{\mathrm{obs}}; \quad \zeta_4 = \frac{R_e}{\mathrm{arcsec}} \quad ;$$

$$\zeta_5 = \frac{M_i/L_i}{10^{10}\mathrm{m}_\odot/\mathrm{L}_\odot} \ ; \ \zeta_6 = I_T \ ; \ \zeta_7 = \hat{m} - \hat{M} \ , \quad (88b)$$

where some symbols have been changed to gain simplicity. An inspection of Eq. (88a) shows that the dimensionless energy c_{ij} is monotonically increasing with increasing ζ_4, ζ_6, ζ_2, ζ_3, and decreasing ζ_5, ζ_7; and vice versa. Establishing the trend with the remaining variables ζ_1, i, δ demands further considerations.

The function $B(\epsilon)$ defined by Eq. (83), is monotonically decreasing in the domain $0 \leq \epsilon \leq 1$ where $\pi = B(0) \geq B(\epsilon) \geq B(1) = 2$. Accordingly, $B(\epsilon)$ is monotonically decreasing with decreasing $\zeta_1 = <\hat{e}_\perp>$ and/or decreasing i, and vice versa.

43

With regard to the anisotropy parameter δ, the following identity holds:

$$\frac{3 - \delta}{1 - \delta \cos^2 i} = \left[\cos^2 i + \frac{\sin^2 i - 2\cos^2 i}{3 - \delta}\right]^{-1} \quad , \quad (89)$$

and the special inclination angle i_0, which makes null the fraction within brackets, is the solution of the equation:

$$\sin^2 i_0 - 2\cos^2 i_0 = 3\sin^2 i_0 - 2 = 0 \quad , \qquad (90)$$

the result is:

$$\sin i_0 = \sqrt{\frac{2}{3}} \; ; \quad i_0 = 0.955\,316\,6 = 54.735\,61° \; . \quad (91)$$

Accordingly, the fraction on the left-hand side of Eq. (89) is monotonically decreasing for increasing δ in the range $i_0 < i \leq \pi/2$ and is monotonically increasing for increasing δ in the range $0 \leq i < i_0$ while no dependence on δ occurs in the special case

$i = i_0$. Finally, Eq. (84a), Eq. (89), and Eq. (90) show that the dimensionless energy c_{ij}, is monotonically increasing or decreasing for increasing δ depending on whether $0 \leq i < i_0$ or $i_0 < i \leq \pi/2$, respectively, and vice versa, while no dependence on δ occurs in the special case $i = i_0$.

The above results may be reduced to a single relation as:

$$c_{ij} \mp \Delta c_{ij}$$
$$= \frac{1}{1163.335} \frac{1}{G} \frac{\zeta_4 \mp \Delta\zeta_4}{\zeta_5 \pm \Delta\zeta_5}$$
$$\times \exp_{10}[0.4(\zeta_6 \mp \Delta\zeta_6) - 0.2(\zeta_7 \pm \Delta\zeta_7) - 6.644]$$
$$\times \frac{\{1 - [1 - (\zeta_1 \pm \Delta\zeta_1)]^2\}^{1/2}/\sin(i \pm \Delta i)}{\arcsin\{\{1 - [1 - (\zeta_1 \pm \Delta\zeta_1)]^2\}^{1/2}/\sin(i \pm \Delta i)\}}$$
$$\times \left\{\frac{2(\zeta_2 \mp \Delta\zeta_2)^2}{\sin^2(i \pm \Delta i)} + \right.$$
$$\left. + \frac{\{3 - [\delta \pm \mathrm{sgn}(i - i_0)\Delta\delta]\}(\zeta_3 \mp \Delta\zeta_3)^2}{1 - [\delta \pm \mathrm{sgn}(i - i_0)\Delta\delta]\cos^2(i \pm \Delta i)}\right\} , \quad (92)$$
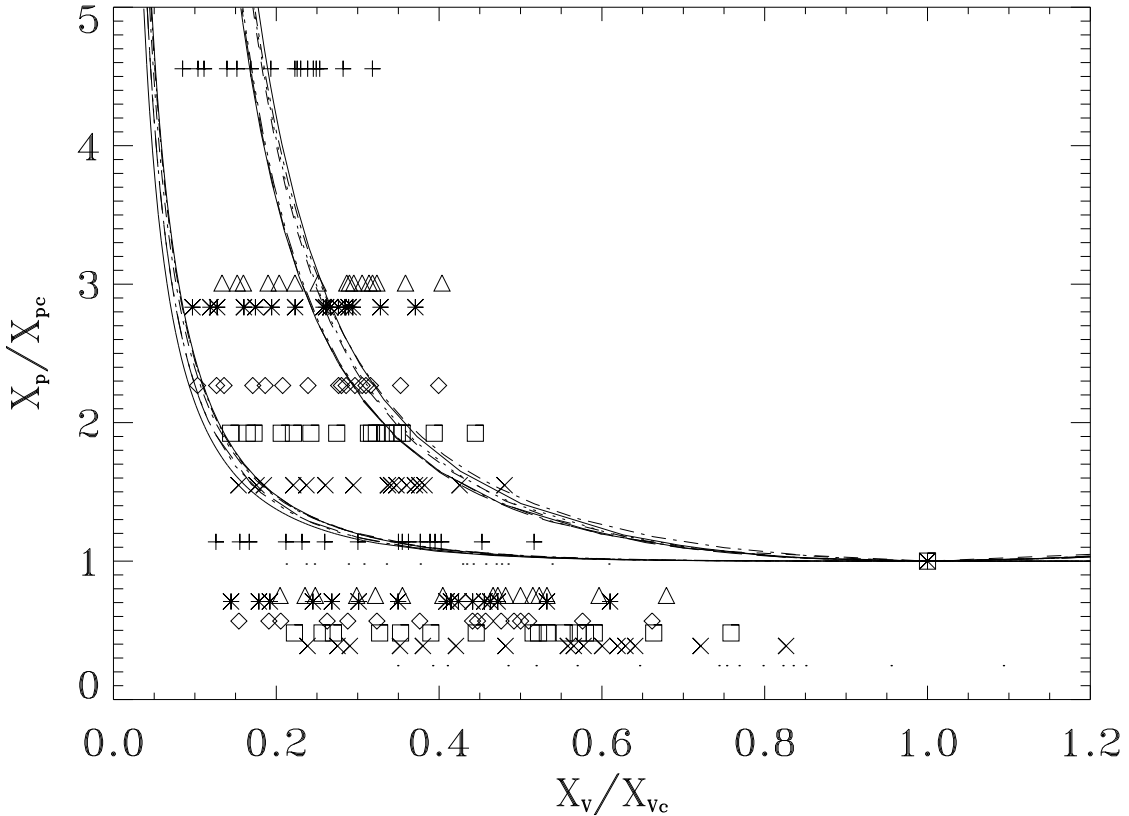

Fig. 13. *Elliptical galaxies listed in Tables 5 and 6, modelled as HH macrogases for different choices of scaled truncation radii Ξ_i, Ξ_j, and fractional mass m. The critical macroisothermal curve (left) and the boundary of the GS region (right) are also plotted for each case. Symbol caption and line style: $(\Xi_i, \Xi_j) = (10,5)$ - crosses, full; $(10,10)$ - asterisks, dotted; $(10,20)$ - diamonds, dashed; $(20,5)$ - triangles, dot-dashed; $(20,10)$ - squares, long-short-dashed; $(20,20)$ - St. Andrew's crosses, long-dashed; $(+\infty, +\infty)$ - dots, full. Lower and upper symbols of the same kind are related to $m = 10, 20$, respectively. The composite symbol marks the critical point. Cases where $\Xi_i = 5$ make two galaxies unable to be modelled, and for this reason are not considered.*
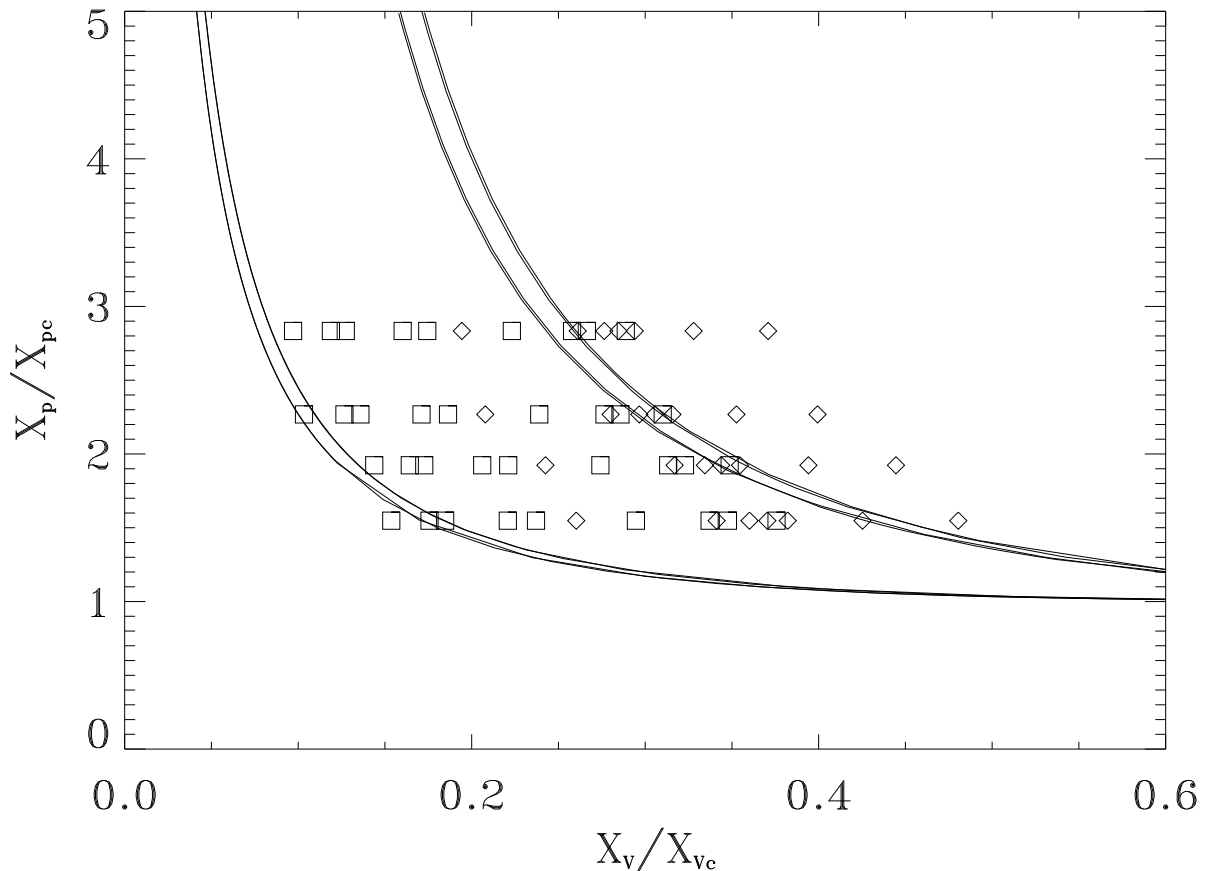
Fig. 14. *Same as in Fig. 13 for scaled truncation radii* $(\Xi_i, \Xi_j) = (10, 10), (10, 20), (20, 10), (20, 20)$ *from top to bottom, and fractional mass* $m = 20$ *where model galaxies are distinguished according to whether their parent sample object is classified as fast (squares) or slow (diamonds) rotator.*

where upper and lower signs correspond to the lower and upper c_{ij} value, respectively, and sgn is the sign function defined as $\mathrm{sgn}(x) = x/|x|$, $x \neq 0$; $\mathrm{sgn}(0) = 0$. It is worth emphasizing that Eq. (92) makes an exact formulation of the uncertainty on the dimensionless energy c_{ij} as defined by Eq. (84a). On the contrary, standard linear and quadratic error propagation formulae apply to any kind of functions allowing Taylor series development, but are approximate instead of being exact.

To the knowledge of the author, the part of errors on the right-hand side of Eq. (92) is not available in literature. For the inclination angle i and the anisotropy parameter δ the reason is in that they depend on a reference dynamic model (S IV; S X) and cannot be specified. The following values are found: $\Delta\zeta_4/\zeta_4 = 0.17$ (S IV), 0.20 (S X); $\Delta\zeta_6/\zeta_6 = 0.13$ (S IV); $\Delta\zeta_5/\zeta_5 = 0.10$, strongly dependent on the assumptions made (S IV); $\Delta\zeta_7 = 0.09 - 0.33$, with a value listed for each sample object (S IV). In this view, it seems better starting from assigned values of the dimensionless energy relative error $\Delta c_{ij}/c_{ij}$ and numerically evaluate the related uncertainty on the position of a selected model galaxy on the $(\mathrm{O}\mathcal{X}_\mathrm{V}\mathcal{X}_\mathrm{p})$ plane, to visualize the trend.

4.5. Results

With regard to HH macrogases, model galaxies corresponding to sample objects listed in Tables 5 and 6 are represented on the $(\mathrm{O}\mathcal{X}_\mathrm{V}\mathcal{X}_\mathrm{p})$ plane of Fig. 13 for different choices of scaled truncation radii Ξ_i, Ξ_j and fractional mass m. The critical macroisothermal curve (left) and the boundary of the GS region (right) are also plotted for each case.

The critical point is marked by a composite symbol. Two sample objects cannot be modelled for low inner scaled truncation radii ($\Xi_i = 5$) and, for this reason, related cases are not considered. Lower and upper symbols of the same kind correspond to $m = 10, 20$, respectively.

Under the working hypothesis of an analogy between VDW gases and macrogases, modelled elliptical galaxies are expected to lie in the S region or slightly outside the S region within the GS region at most. An inspection of Fig. 13 shows the following:
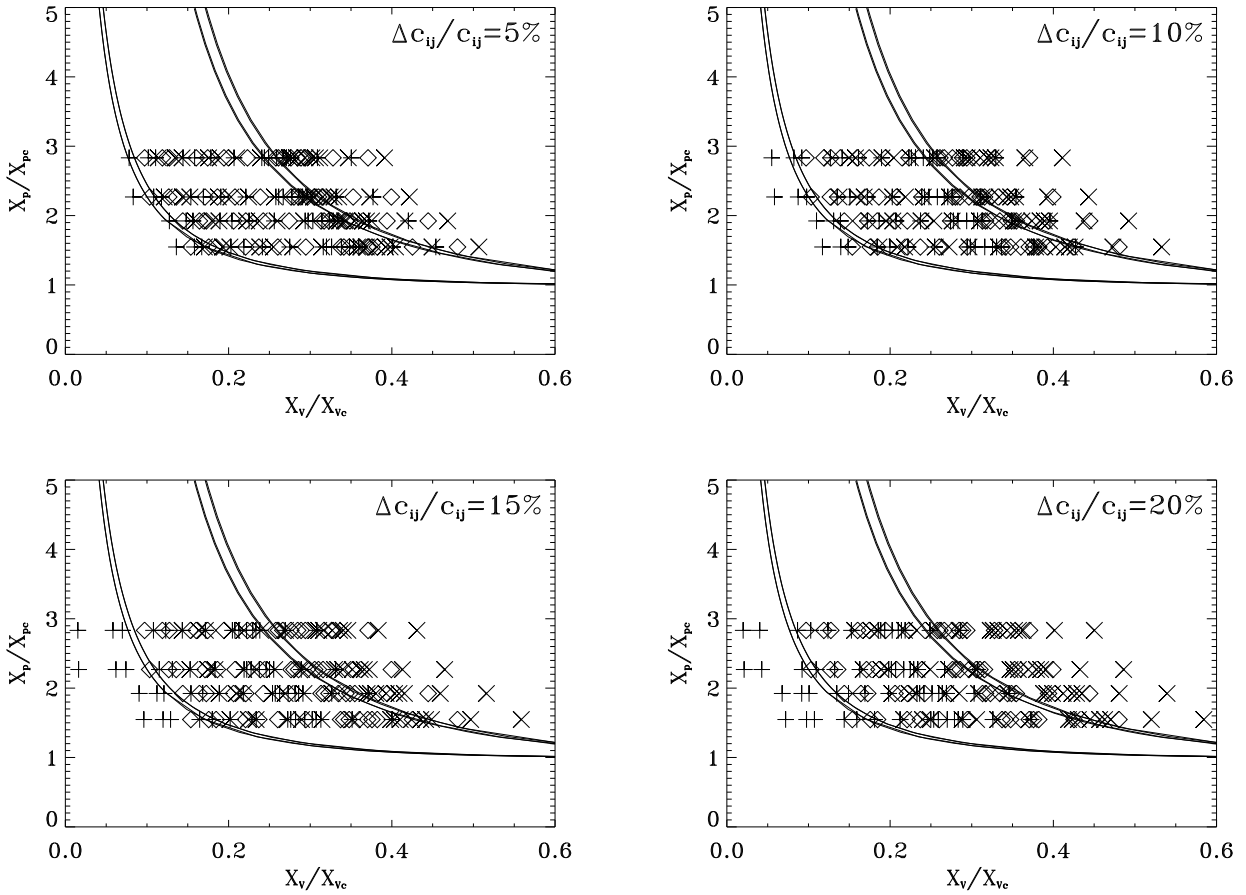
Fig. 15. *Same as in Fig. 13 for different choices of scaled truncation radii* $(\Xi_i, \Xi_j) = (10, 10)$, $(10, 20)$, $(20, 10)$, $(20, 20)$, *from top to bottom, and fractional masses* $m = 20$ *where dimensionless energies* c_{ij}, *defined by Eq. (84a), are lowered to* $c_{ij} - \Delta c_{ij}$ *(Greek crosses) and increased to* $c_{ij} + \Delta c_{ij}$ *(St. Andrew's crosses) with respect to their original values (diamonds), by a factor equal to 5%, 10%, 15%, 20%, respectively. In the last case, a sample object (NGC 4473) cannot be modelled for lowered values* $c_{ij} - \Delta c_{ij}$, *and* $(\Xi_i, \Xi_j) = (10, 10)$, $(10, 20)$.

(1) model galaxies with low fractional mass ($m = 10$) and/or no truncation radii ($\Xi \to +\infty$) lie below the critical macroisothermal curve in the G region, and for this reason cannot be accepted; (2) about one half of model galaxies with low outer scaled radii ($\Xi_j = 5$) lie well inside the GS region and, for this reason, cannot be accepted; (3) more than one half of model galaxies with larger scaled radii ($\Xi_i = 10, 20$; $\Xi_j = 10, 20$) lie within the S region and, for this reason, are accepted.

With regard to viable cases, the plot of Fig. 13 is repeated in Fig. 14, where model galaxies are distinguished according to whether their parent sample object is a fast (squares) or a slow (diamonds) rotator.

The related scaled truncation radii (from top to bottom) are $(\Xi_i, \Xi_j) = (10, 10)$, $(10, 20)$, $(20, 10)$, $(20, 20)$ and the fractional mass is $m = 20$. The curves are as in Fig. 13.

Restricting to viable cases, the plot of Fig. 13 is repeated in Fig. 15 where the effect of assigned errors in dimensionless energy $\Delta c_{ij}/c_{ij} = 5\%$, 10%, 15%, 20%, labelled on each panel, on model galaxies, is represented.

More specifically, the position of model galaxies is marked by diamonds, and the change due to lowered ($c_{ij} - \Delta c_{ij}$) and increased ($c_{ij} + \Delta c_{ij}$) dimensionless energy, is marked by Greek and St. Andrew's crosses, respectively. Scaled truncation radii are, from top to bottom, $(\Xi_i, \Xi_j) = (10, 10)$, $(10, 20)$, $(20, 10)$, $(20, 20)$, and the fractional mass is $m = 20$ in all cases. In the special cases $(\Xi_i, \Xi_j) = (10, 10)$, $(10, 20)$, and $\Delta c_{ij}/c_{ij} = 20\%$, a sample object (NGC 4473) cannot be modelled for lowered dimensionless energies $c_{ij} - \Delta c_{ij}$. In general, lowered and increased dimensionless energies c_{ij} make model galaxies shift to the left and to the right, respectively, from their
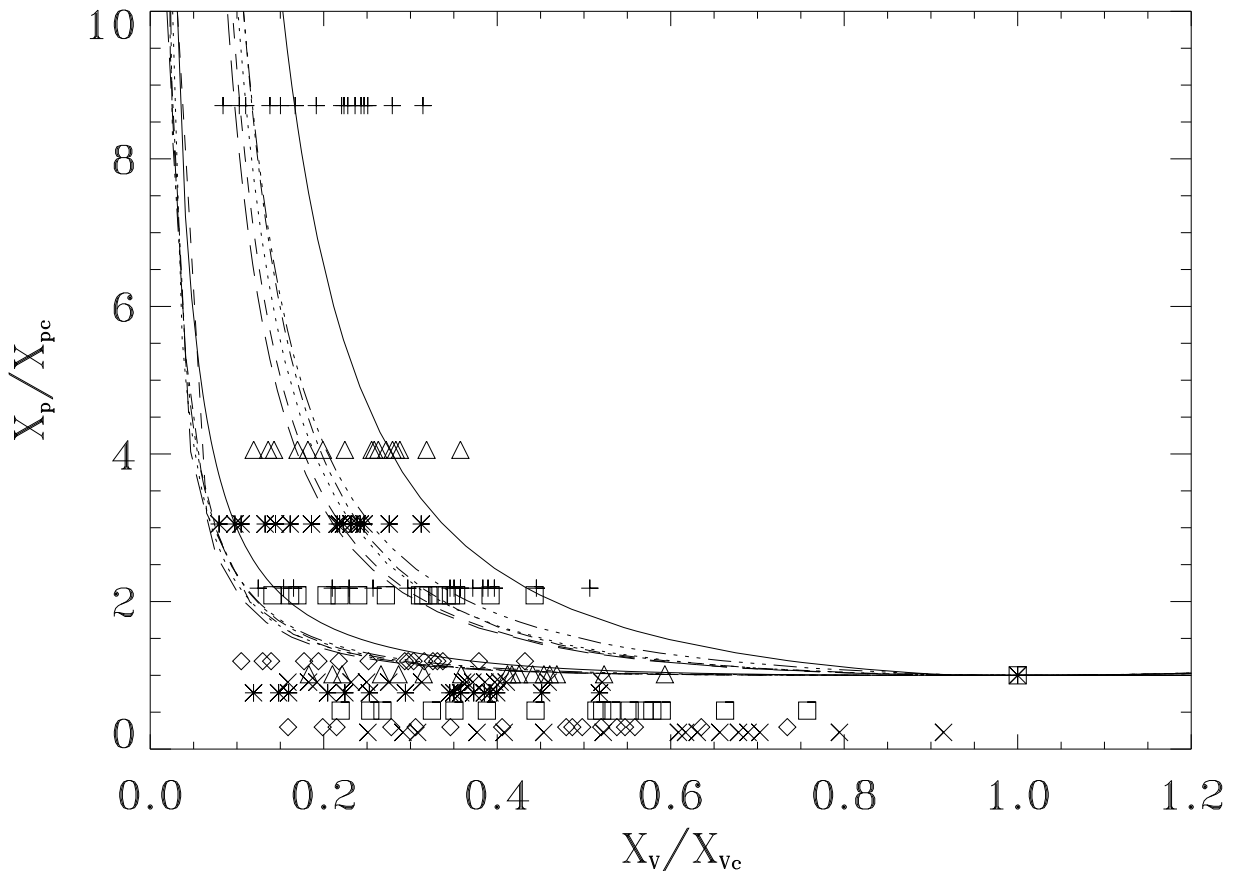
Fig. 16. *Elliptical galaxies listed in Tables 5 and 6, modelled as HN/NH macrogases for different choices of scaled truncation radii Ξ_i, Ξ_j and fractional mass m. The critical macroisothermal curve (left) and the boundary of the GS region (right) are also plotted for each case. Symbol caption and line style: $(\Xi_i, \Xi_j) = (10, 5)$ - crosses, full; $(10, 10)$ - asterisks, dotted; $(10, 20)$ - diamonds, dashed; $(20, 5)$ - triangles, dot-dashed; $(20, 10)$ - squares, long-short-dashed; $(20, 20)$ - St. Andrew's crosses, long-dashed. Lower and upper symbols of the same kind are related to $m = 10, 20$, respectively. The composite symbol marks the critical point. Cases where $\Xi_i = 5$ make two galaxies unable to be modelled and, for this reason, are not considered. The same holds, to a larger extent, for cases $(\Xi_i, \Xi_j) \to (+\infty, +\infty)$ due to an infinite mass of the NFW density profile.*

position in the $(O X_V X_p)$ plane. Accordingly, a fraction of model galaxies enter the G region and the GS region, respectively, and the fit could be improved by changing the input parameters Ξ_i, Ξ_j and m.

With regard to HN/NH macrogases, model galaxies, corresponding to sample objects listed in Tables 5 and 6 are represented in the $(O X_V X_p)$ plane of Fig. 16 for different choices of scaled truncation radii Ξ_i, Ξ_j and fractional mass m. The critical macroisothermal curve (left) and the boundary of the GS region (right) are also plotted for each case.

The critical point is marked by a composite symbol. Two sample objects cannot be modelled for low inner scaled truncation radii ($\Xi_i = 5$) and, for this reason, related cases are not considered. The same holds, to a larger extent, for cases $(\Xi_i, \Xi_j) \to (+\infty, +\infty)$ due to an infinite mass of the

NFW density profile. Lower and upper symbols of the same kind correspond to $m = 10, 20$, respectively.

Under the working hypothesis of an analogy between VDW gases and macrogases, modelled elliptical galaxies are expected to lie in the S region or slightly outside the S region, within the GS region at most. An inspection of Fig. 16 shows the following: (1) model galaxies with low fractional mass ($m = 10$) and/or large outer scaled truncation radius ($\Xi_j = 20$) lie (at least partially) below the critical macroisothermal curve in the G region and, for this reason, the related cases cannot be accepted; (2) more than one half of model galaxies with large fractional mass ($m = 20$) and/or low outer scaled truncation radius ($\Xi_j = 5$) lie well inside the GS region and, for this reason, the related cases cannot
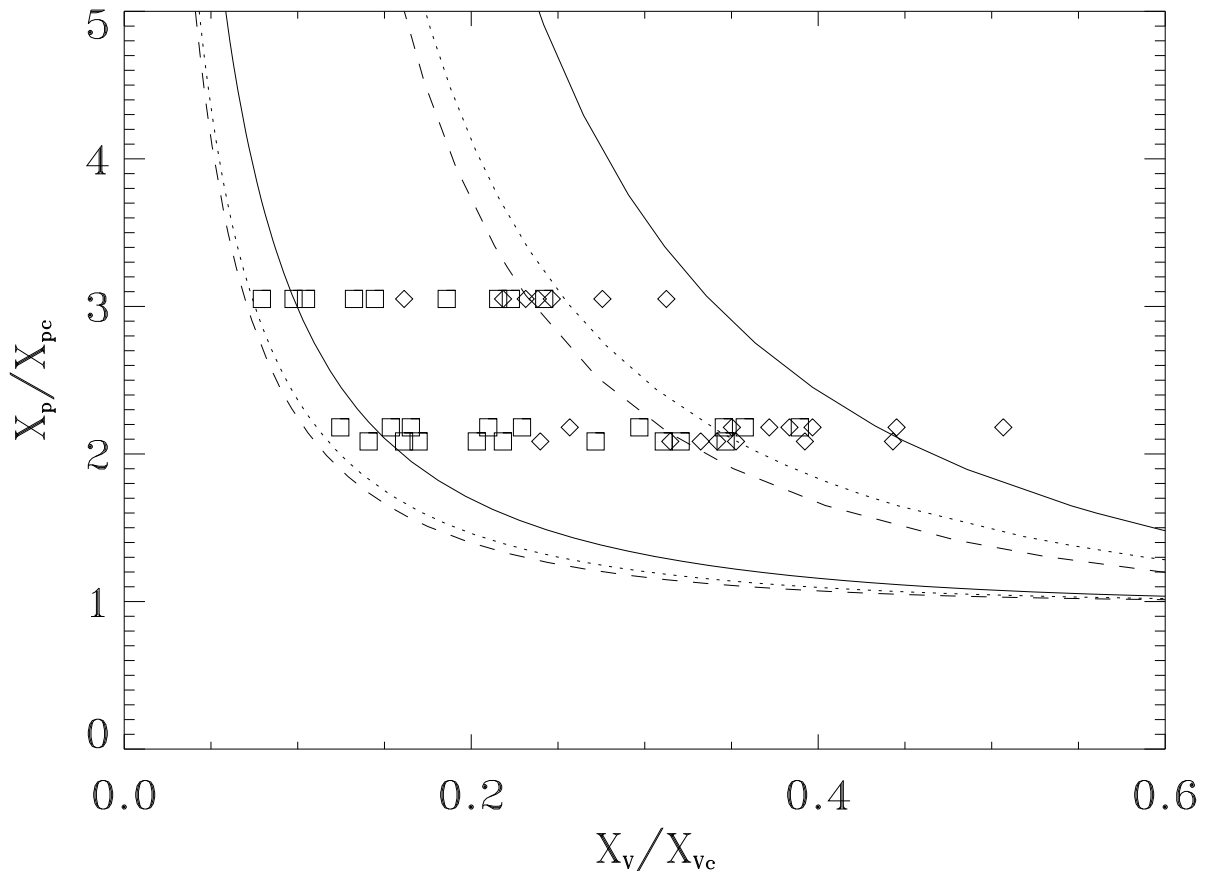
Fig. 17. *Same as in Fig. 16 for scaled truncation radii* $(\Xi_i, \Xi_j) = (10, 10)$, $(10, 5)$, $(20, 10)$ *from top to bottom, and fractional mass* $m = 20$, $\Xi_j = 10$, *and* $m = 10$, $\Xi_j = 5$, *where model galaxies are distinguished according to whether their parent sample object is classified as fast (squares) or slow (diamonds) rotator.*

be accepted; (3) more than one half of model galaxies with large fractional mass ($m = 20$) and outer scaled radius ($\Xi_j = 10$), or low fractional mass ($m = 10$) and outer scaled radius ($\Xi_j = 5$) lie within the S region and, for this reason, the related cases are accepted.

With regard to viable cases, the plot of Fig. 16 is repeated in Fig. 17, where model galaxies are distinguished according to whether their parent sample object is a fast (squares) or a slow (diamonds) rotator.

The related scaled truncation radii (from top to bottom) are $(\Xi_i, \Xi_j) = (10, 10)$, $(10, 5)$, $(20, 10)$, and the fractional mass is $m = 20$ for $\Xi_j = 10$, and $m = 10$ for $\Xi_j = 5$. The curves are as in Fig. 16.

Restricting to viable cases, the plot of Fig. 16 is repeated in Fig. 18 where the effect of assigned errors in dimensionless energy $\Delta c_{ij}/c_{ij} = 5\%$, 10%, 15%, 20%, labelled on each panel, on model galaxies, is represented.

More specifically, the position of model galaxies is marked by diamonds and the change due to lowered $(c_{ij} - \Delta c_{ij})$ and increased $(c_{ij} + \Delta c_{ij})$ dimensionless energy is marked by Greek and St. Andrew's

crosses respectively. Scaled truncation radii and fractional masses are $(\Xi_i, \Xi_j, m) = (10, 10, 20)$, $(10, 5, 10)$, $(20, 10, 20)$, from top to bottom.

In the special case $(\Xi_i, \Xi_j, m) = (10, 5, 10)$ and $\Delta c_{ij}/c_{ij} = 20\%$, a sample object (NGC 4486) is out of scale on the right for increased dimensionless energies, $c_{ij} + \Delta c_{ij}$. In the special cases $(\Xi_i, \Xi_j, m) = (10, 5, 10)$, $(10, 10, 20)$, and $\Delta c_{ij}/c_{ij} = 20\%$, a sample object (NGC 4473) cannot be modelled for lowered dimensionless energies $c_{ij} - \Delta c_{ij}$. In general, lowered and increased dimensionless energies c_{ij} make model galaxies shift to the left and to the right, respectively, from their position in the $(O\,X_V\,X_p)$ plane. Accordingly, a fraction of model galaxies enter the G region and the GS region respectively, and the fit could be improved by changing the input parameters Ξ_i, Ξ_j and m.

4.6. Discussion

Current cosmological models imply that large-scale celestial bodies such as galaxies and clusters of galaxies are embedded within nonbaryonic dark
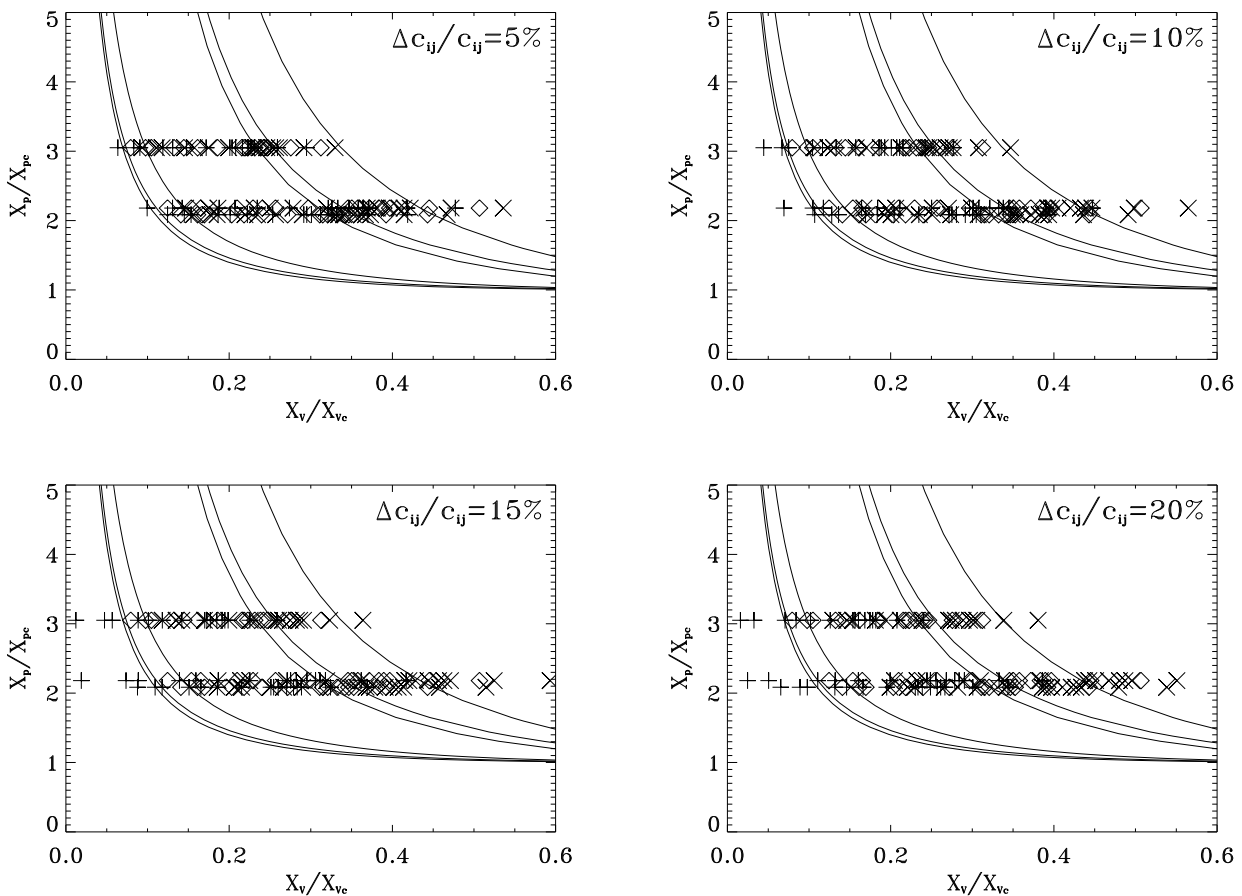
Fig. 18. *Same as in Fig. 16 for different choices of scaled truncation radii and fractional masses,* $(\Xi_i, \Xi_j, m) = (10, 10, 20), (10, 5, 10), (20, 10, 20)$, *from top to bottom, where dimensionless energies, c_{ij}, defined by Eq. (84a), are lowered to $c_{ij} - \Delta c_{ij}$ (Greek crosses) and increased to $c_{ij} + \Delta c_{ij}$ (St. Andrew's crosses) with respect to their original values (diamonds), by a factor equal to 5%, 10%, 15%, 20%, respectively. In the last case, a sample object (NGC 4473) cannot be modelled for lowered values, $c_{ij} - \Delta c_{ij}$, and $(\Xi_i, \Xi_j, m) = (10, 5, 10), (10, 10, 20)$, and a sample object (NGC 4486) is out of scale on the right for increased values, $c_{ij} + \Delta c_{ij}$, and $(\Xi_i, \Xi_j, m) = (10, 5, 10)$.*

haloes, and the two subsystems interact only via gravitation. Accordingly, large-scale celestial bodies can be modelled as macrogases where macrovolume, macropressure, and macrotemperature can be defined, and a counterpart of the VDW theory for ordinary gases can be developed. Sufficiently steep density profiles, as in HH and HN/NH macrogases, show a similar trend with respect to VDW gases: the macroisothermal curves are nonmonotonic with two extremum points (one maximum and one minimum) above a critical macrotemperature, and are monotonic below a critical macrotemperature. The critical macroisothermal curve is characterized by a single extremum point where the maximum and the minimum coincide yielding a horizontal inflexion point. On the other hand, sufficiently mild density profiles, such as in UU and PP (CV08) macrogases, show only nonmonotonic macroisothermal curves with two ex-

tremum points (one maximum and one minimum) where no critical macroisothermal curve exists.

A generic macrogas equation of state is formulated in terms of dimensionless variables normalized to critical values (or conveniently chosen in absence of the critical point). Similar to what has been done in dealing with the reduced VDW equation for ordinary gases (e.g. LL67, Chap. VIII, §85), the states of two large-scale celestial bodies with equal $\bar{X}_V$, $\bar{X}_p$, $\bar{X}_T$, or y, m, ϕ, for assigned scaled truncation radii Ξ_i, Ξ_j, and belonging to the same family of macrogases, may be defined as corresponding states. The mere existence of a macrogas equation of state yields the following result:

Law of corresponding states. Given two large-scale celestial bodies belonging to the same family of macrogases with assigned

scaled truncation radii Ξ_i, Ξ_j, the equality of two out of three reduced variables $\mathcal{X}_\mathrm{V}$, $\mathcal{X}_\mathrm{p}$, $\mathcal{X}_\mathrm{T}$, or y, m, ϕ, implies the equality between the remaining related reduced variables i.e. the two macrogases are in corresponding states.

The law of corresponding states cannot be extended to macrogases with different scaled truncation radii as shown in Fig. 9 and Fig. 12. A possible explanation may be the following. Contrary to ordinary gases, bounded by rigid walls which have no influence on the equation of state, macrogases are confined by "gravitational" walls appearing in the equation of state via the potential energy terms which, in turn, depend on the scaled truncation radii.

Ordinary gases exhibit monotonic isothermal curves where the central part of the related VDW isothermal curve, including the extremum points, is replaced by a horizontal line and a phase transition occurs therein. With regard to macrogases, the existence of a phase transition and monotonic macroisothermal curves of the kind considered, must necessarily be assumed as a working hypothesis by analogy with VDW gases. The phase transition must be conceived between gas and stars, and the $(O\mathcal{X}_\mathrm{V}\mathcal{X}_\mathrm{p})$ plane may be divided into three parts: (i) the G region, where only gas exists; (ii) the S region, where only stars exist; (iii) the GS region, where both gas and stars exist. In this view, model elliptical galaxies are expected to lie within the S region or slightly outside the boundary between the S and the GS region at most.

It is the case for different models related to both HH and HN/NH macrogases where acceptable values of scaled truncation radii and fractional masses are used as shown in Fig. 13 and Fig. 16. The assumption of universal fractional mass for sample objects is not a limit of the model, which equally holds for assigning different fractional masses to different sample objects.

It can be seen from Fig. 14 and Fig. 17 that fast rotators lie within the S region while slow rotators are close (from both sides) to the boundary between the S and the GS region. This dichotomy could be interpreted by the different nature of the two classes of sample objects. More specifically, fast rotators seem consistent with elliptical galaxies with disky isophotes, which experienced minor mergers and accreted a significant amount of gas (S X) suddenly turned into stars. On the other hand, systematically more massive (with the exception of NGC 4458 and, marginally, NGC 3608, see Table 6) slow rotators may be related to elliptical galaxies with boxy isophotes, which experienced major gas-rich mergers, or sequences of mergers, and regulation by the feedback of a powerful central active galactic nucleus (S X), in some cases allowing gas survival as e.g., diffuse, still undetected interstellar medium.

Accordingly, in the $(O\mathcal{X}_\mathrm{V}\mathcal{X}_\mathrm{p})$ plane, fast rotators and a fraction of slow rotators are expected to lie within the S region, and the remaining part of slow rotators to be placed in the GS region, as shown in Fig. 14 and Fig. 17. The following trend is also exhibited: fast rotators are systematically to the left with respect to slow rotators, with the exception of NGC 4458, which is the sole sample slow rotator with low mass, possibly due to having experienced minor instead of major mergers. In this view, NGC 4458 should be considered as a peculiar fast rotator where low rotation rate could be due to special configurations e.g. still undetected counter-rotating components as observed in the disk of NGC 4450 (e.g. S X).

The reduced variable $\mathcal{X}_\mathrm{V} = X_\mathrm{V}/X_{\mathrm{V}_c}$, via Eq. (22b) and Eq. (30e), is proportional to the fractional truncation radius $1/y = R_i/R_j$. The above mentioned dichotomy, exhibited by fast and slow rotators in the $(O\mathcal{X}_\mathrm{V}\mathcal{X}_\mathrm{p})$ plane, implies a larger fractional truncation radius $y = R_j/R_i$ for fast rotators with respect to slow rotators. This result could be interpreted as due to different formation mechanisms: minor mergers would produce larger contraction of the baryonic matter while major mergers would make (possibly via active galactic nuclei) smaller contraction of the baryonic matter yielding a larger or smaller fractional radius, respectively.

5. CONCLUSION

In the current attempt, two-component large-scale celestial bodies where the subsystems interact only via gravitation, are conceived as macrogases bounded by "gravitational" walls. The macrogas equation of state is formulated in terms of macrovolume, macropressure, and macrotemperature, which are dimensionless variables. For sufficiently steep density profiles, which fit to observed elliptical galaxies (or more generally, spheroid components) and to simulated nonbaryonic dark matter haloes, macroisothermal curves on the $(O\mathcal{X}_\mathrm{V}\mathcal{X}_\mathrm{p})$ plane show an analogy with VDW isothermal curves exhibited by VDW gases. More specifically, a critical macroisothermal curve exists, below and above which the macroisothermal curves are monotonic and nonmonotonic (with two extremum points, one maximum and one minimum) respectively. The critical macroisothermal curve is characterized by a single extremum point (a horizontal inflexion point) which is the critical point.

Contrary to ordinary gases, macrogases cannot be tested in laboratory and, for this reason, a working hypothesis is inescapable. By analogy with ordinary gases, real macroisothermal curves are supposed to occur instead of their theoretical counterparts (deduced from the macrogas equation of state), where the central part, containing the extremum points, is replaced by a horizontal line along which a phase transition takes place. The intersection between a selected theoretical macroisothermal curve and its real counterpart yields two regions of equal area. The phase transition is assumed to be gas-stars instead of vapour-liquid as in ordinary gases. Accordingly, the first quadrant of the $(O\mathcal{X}_\mathrm{V}\mathcal{X}_\mathrm{p})$ plane is divided into three parts, namely: (i) the G region, where only gas exists; (ii) the S region, where only stars exist; (iii) the GS region, where both gas and stars exist.

For selected density profiles and scaled truncation radii Ξ_i Ξ_j, the macrogas equation of state depends on three parameters $\not{X}_{\mathrm{V}}$, $\not{X}_{\mathrm{p}}$, $\not{X}_{\mathrm{T}}$ or the fractional truncation radius y, the fractional mass m, and the fractional energy ϕ. If elliptical galaxies and their hosting nonbaryonic dark haloes are conceived as macrogases, a selected model is accepted only if a whole set of sample objects (from which radii, masses, and rsm velocities can be determined) lies within the S region or slightly outside the boundary between the S and the GS region at most. The sample used (CV08, $N = 16$) is extracted from larger samples of early-type galaxies investigated within the SAURON project (SIV, $N = 25$; SX, $N = 48$). The position of model galaxies in the $(\mathrm{O}\not{X}_{\mathrm{V}}\not{X}_{\mathrm{p}})$ plane is determined through the following steps: (i) Select SAURON data of interest; (ii) Calculate the parameters appearing in the virial equations; (iii) Make a correspondance between model galaxies and sample objects; (iv) Represent model galaxies in the $(\mathrm{O}\not{X}_{\mathrm{V}}\not{X}_{\mathrm{p}})$ plane.

The main results found in the present investigation may be summarized as follows.

(1) A new numerical algorithm has been used for determining the critical point of selected HH and HN/NH macrogases, improving earlier results (CV08). In particular, the critical point exists for all the cases considered.

(2) A principle of corresponding states rigorously holds for selected density profiles and scaled truncation radii and, to a first extent only, for selected density profiles.

(3) The following models (on a total of 20) can be accepted in the above mentioned sense: $(\Xi_i, \Xi_j, m) = (10, 10, 20)$, $(10, 20, 20)$, $(20, 10, 20)$, $(20, 20, 20)$, with regard to HH macrogases, and $(\Xi_i, \Xi_j, m) = (10, 5, 10)$, $(10, 10, 20)$, $(20, 10, 20)$, for HN/NH macrogases. The values of model parameters may be changed by the occurrence of systematic errors.

(4) Fast rotators exhibit larger fractional truncation radii with respect to slow rotators, which makes the former lie within the S region and the latter close (from both sides) to the boundary between the S and the GS region, with regard to acceptable models. This dichotomy could be interpreted in terms of a different evolution related to fast and slow rotators, where gas is currently absent in the former and can be present (even if still undetected) in the latter.

REFERENCES

Binney, J.: 2005, *Mon. Not. R. Astron. Soc.*, **363**, 937.

Binney, J., Tremaine, S.: 1987, Galactic Dynamics, Princeton University Press, Princeton.

Burrows, A.: 2000, *Nature*, **403**, 727.

Caimmi, R.: 1986, *Astron. Astrophys.*, **159**, 147.

Caimmi, R.: 2007, *Serb. Astron. J.*, **174**, 13.

Caimmi, R.: 2009, *New Astron.*, **14**, 254.

Caimmi, R., Secco, L., Brosche, P.: 1984, *Astron. Astrophys.*, **139**, 411.

Caimmi, R., Secco, L.: 1990, *Astron. Astrophys.*, **237**, 336. (CS90).

Caimmi, R., Secco, L.: 1992, *Astrophys. J.*, **395**, 119.

Caimmi, R., Valentinuzzi, T.: 2008, *Serb. Astron. J.*, **177**, 15. (CV08)

Cappellari, M., Bacon, R., Bureau, M. et al.: 2006, *Mon. Not. R. Astron. Soc.*, **366**, 1126. (SIV).

Cappellari, M., Emsellem, E., Bacon, R. et al.: 2007, *Mon. Not. R. Astron. Soc.*, **379**, 418. (SX).

Chandrasekhar, S.: 1939, An Introduction to the Study of the Stellar Structure, University of Chicago Press.

Chandrasekhar, S.: 1969, Ellipsoidal Figures of Equilibrium, Yale University Press, New Haven.

Ciotti, L.: 1996, *Astrophys. J.*, **471**, 68.

Ciotti, L., Pellegrini, S.: 1992, *Mon. Not. R. Astron. Soc.*, **255**, 561.

Djorgovski, S. G., Davis, M.: 1987, *Astrophys. J.*, **313**, 59.

D'Onofrio, M., Valentinuzzi, T., Secco, L. et al.: 2006, *New Astron. Rev.*, **50**, 447.

Dressler, A., Lynden-Bell, D., Burstein, D. et al.: 1987, *Astrophys. J.*, **313**, 42.

Hernquist, L.: 1990, *Astrophys. J.*, **356**, 359.

Landau, L., Lifchitz, E.: 1966, Mecanique, Mir, Moscow.

Landau, L., Lifchitz, E.: 1967, *Physique Statistique*, Mir, Moscow. (LL67),

Lowenstein, M., White, R. E., III: 1999, *Astrophys. J.*, **518**, 50.

Navarro, J. F., Frenk, C. S., White, S. D. M.: 1995, *Mon. Not. R. Astron. Soc.*, **275**, 720.

Navarro, J. F., Frenk, C. S., White, S. D. M.: 1996, *Astrophys. J.*, **462**, 563.

Navarro, J. F., Frenk, C. S., White, S. D. M.: 1997, *Astrophys. J.* **490**, 493.

Roberts, P. H.: 1962, *Astrophys. J.*, **136**, 1108.

Rostagni, A.: 1957, Meccanica e Termodinamica, ed. Libreria Universitaria di G. Randi, Padova.

Spiegel, M. R.: 1968, Mathematical Handbook, Schaum's Outline Series, McGraw-Hill, Inc., New York.

Vandervoort, P. O.: 1980, *Astrophys. J.*, **240**, 478.

van der Waals, J. D.: 1873, Over de Continuiteit van den Gas-en Vloeistoftoestand (Doctoral Thesis).

APPENDIX

A1. TIDAL POTENTIAL ENERGY PROFILE FACTORS

The tidal potential energy for homeoidally striated ellipsoids related to similar and similarly placed boundaries, depends on the reference fractional mass $m^\dagger$, the fractional scaling radius $y^\dagger$, and the functions $w^{(\mathrm{int})}(\eta)$, $w^{(\mathrm{ext})}(\eta)$, $\eta = \Xi_i/y^\dagger = \Xi_j/y$, expressed by Eqs. (25). Let the two subsystems be denoted as A and B regardless of what is the outer and what is the inner. Conformingly, Eqs. (22) read:

$$\frac{\Xi_B}{\Xi_A} = \frac{y_{BA}}{y_{BA}^\dagger} \ ; \quad \eta_{BA} = \frac{\Xi_A}{y_{BA}^\dagger} = \frac{\Xi_B}{y_{BA}} \ ;$$

$$y_{BA}^\dagger = \frac{r_B^\dagger}{r_A^\dagger} \ ; \quad y_{BA} = \frac{R_B}{R_A} \geq 1 \ ;$$

$$\xi_A = y_{BA}^\dagger \xi_B \ ; \quad m_{BA}^\dagger = \frac{M_B^\dagger}{M_A^\dagger} \ ; \quad m_{BA} = \frac{M_B}{M_A} \ , \quad (93\mathrm{a})$$

$$\frac{\Xi_A}{\Xi_B} = \frac{y_{AB}}{y_{AB}^\dagger} \ ; \quad \eta_{AB} = \frac{\Xi_B}{y_{AB}^\dagger} = \frac{\Xi_A}{y_{AB}} \ ;$$

$$y_{AB}^\dagger = \frac{r_A^\dagger}{r_B^\dagger} \ ; \quad y_{AB} = \frac{R_A}{R_B} \geq 1 \ ;$$

$$\xi_B = y_{AB}^\dagger \xi_A \ ; \quad m_{AB}^\dagger = \frac{M_A^\dagger}{M_B^\dagger} \ ; \quad m_{AB} = \frac{M_A}{M_B} \ , \quad (93\mathrm{b})$$

according to whether $R_B \geq R_A$ or $R_A \geq R_B$ respectively.

In dealing with sequences of configurations where the scaled truncation radii Ξ_A and Ξ_B are kept unchanged, the combination of Eqs. (93a)-(93b) yields:

$$y_{BA}^\dagger y_{AB}^\dagger = y_{BA} y_{AB} \qquad (94)$$

for any pair of configurations belonging to opposite sides of the sequence with respect to $y_{BA} = y_{AB} = 1$.

In the special case of equal scaled density profiles $F_A = F_B = F$, and equal scaled truncation radii $\Xi_A = \Xi_B = \Xi$, Eqs. (25) reduce to:

$$w^{(\mathrm{int})}(\Xi, y_{BA}^\dagger) = \int_0^{\Xi/y_{BA}^\dagger} F(\xi) \frac{dF(y_{BA}^\dagger \xi)}{d\xi} \xi \, d\xi \ ;$$

$$y_{BA}^\dagger = y_{BA} \geq 1 \ , \qquad (95\mathrm{a})$$

$$w^{(\mathrm{ext})}(\Xi, y_{BA}^\dagger) = \int_0^{\Xi/y_{BA}^\dagger} F(y_{BA}^\dagger \xi) \frac{dF(\xi)}{d\xi} \xi \, d\xi \ ;$$

$$y_{BA}^\dagger = y_{BA} \geq 1 \ , \qquad (95\mathrm{b})$$

$$w^{(\mathrm{int})}(\Xi, y_{AB}^\dagger) = \int_0^{\Xi/y_{AB}^\dagger} F(\xi) \frac{dF(y_{AB}^\dagger \xi)}{d\xi} \xi \, d\xi \ ;$$

$$y_{AB}^\dagger = y_{AB} \geq 1 \ , \qquad (95\mathrm{c})$$

$$w^{(\mathrm{ext})}(\Xi, y_{AB}^\dagger) = \int_0^{\Xi/y_{AB}^\dagger} F(y_{AB}^\dagger \xi) \frac{dF(\xi)}{d\xi} \xi \, d\xi \ ;$$

$$y_{AB}^\dagger = y_{AB} \geq 1 \ . \qquad (95\mathrm{d})$$

In the special case where the fractional scaling radius coincides for both configurations $y_{BA}^\dagger = y_{AB}^\dagger$, the combination of Eq. (95a) and Eq. (95c) Eq. (95b) and Eq. (95d), yields:

$$w^{(\mathrm{int})}(\Xi, y_{BA}^\dagger) = w^{(\mathrm{int})}(\Xi, y_{AB}^\dagger); \ y_{BA}^\dagger = y_{AB}^\dagger, \quad (96\mathrm{a})$$

$$w^{(\mathrm{ext})}(\Xi, y_{BA}^\dagger) = w^{(\mathrm{ext})}(\Xi, y_{AB}^\dagger); \ y_{BA}^\dagger = y_{AB}^\dagger, \quad (96\mathrm{b})$$

regardless of the scaled truncation radius Ξ.

If, on the other hand, $\Xi_A \neq \Xi_B$, the upper integration limits are $\Xi_A/y_{BA}^\dagger$ and $\Xi_B/y_{AB}^\dagger$ for Eq. (95a) and Eq. (95b), Eq. (95c) and Eq. (95d) respectively. Then, $y_{BA}^\dagger = y_{AB}^\dagger$ implies equal integrands but different upper integration limits while $\Xi_A/y_{BA}^\dagger = \Xi_B/y_{AB}^\dagger$ implies equal upper integration limits but different integrands with regard to Eq. (95a) and Eq. (95c), Eq. (95b) and Eq. (95d) respectively. Accordingly, Eq. (96a) and Eq. (96b) no longer hold in the case under discussion unless $\Xi_A \to +\infty$, $\Xi_B \to +\infty$, which erases the dependence on Ξ_A or Ξ_B, regardless of the value of $\lim_{(\Xi_A, \Xi_B) \to +\infty}(\Xi_B/\Xi_A)$.

More specifically, Eqs. (95), where $\Xi = \Xi_A, \Xi_B$, $y^\dagger = y_{BA}^\dagger, y_{AB}^\dagger$, reduce to:

$$w_\infty^{(\mathrm{int})}(y^\dagger) = \lim_{\Xi \to +\infty} w^{(\mathrm{int})}(\Xi, y^\dagger) =$$

$$= \int_0^{+\infty} F(\xi) \frac{dF(y^\dagger \xi)}{d\xi} \xi \, d\xi \ ;$$

$$y^\dagger = y \geq 1 \ , \qquad (97\mathrm{a})$$

$$w_\infty^{(\mathrm{ext})}(y^\dagger) = \lim_{\Xi \to +\infty} w^{(\mathrm{ext})}(\Xi, y^\dagger)$$

$$= \int_0^{+\infty} F(y^\dagger \xi) \frac{dF(\xi)}{d\xi} \xi \, d\xi \ ;$$

$$y^\dagger = y \geq 1 \ . \qquad (97\mathrm{b})$$

Replacing $y^\dagger$ by $1/y^\dagger$ yields:

$$w_\infty^{(\mathrm{int})}\left(\frac{1}{y^\dagger}\right) = \int_0^{+\infty} F(\xi) \frac{dF(\xi/y^\dagger)}{d\xi} \xi \, d\xi \ ;$$

$$y^\dagger = y \geq 1 \ , \qquad (98\mathrm{a})$$

$$w_\infty^{(\mathrm{ext})}\left(\frac{1}{y^\dagger}\right) = \int_0^{+\infty} F\left(\frac{\xi}{y^\dagger}\right) \frac{dF(\xi)}{d\xi} \xi \, d\xi \ ;$$

$$y^\dagger = y \geq 1 \ , \qquad (98\mathrm{b})$$

which, choosing $\xi/y^\dagger$ as integration variable, and keeping in mind that integrals are independent of

integration variables, is equivalent to:

$$w_\infty^{(\mathrm{int})}\left(\frac{1}{y^\dagger}\right) = y^\dagger \int_0^{+\infty} F(y^\dagger \xi)\frac{dF(\xi)}{d\xi}\xi\,d\xi \;\; ;$$

$$y^\dagger = y \geq 1 \;\; , \qquad (99a)$$

$$w_\infty^{(\mathrm{ext})}\left(\frac{1}{y^\dagger}\right) = y^\dagger \int_0^{+\infty} F(\xi)\frac{dF(y^\dagger \xi)}{d\xi}\xi\,d\xi \;\; ;$$

$$y^\dagger = y \geq 1 \;\; , \qquad (99b)$$

and the combination of Eq. (97a) and Eq. (99b), Eq. (97b) and Eq. (99a); produces

$$w_\infty^{(\mathrm{int})}\left(\frac{1}{y^\dagger}\right) = y^\dagger w_\infty^{(\mathrm{ext})}(y^\dagger) \;\; , \qquad (100a)$$

$$w_\infty^{(\mathrm{ext})}\left(\frac{1}{y^\dagger}\right) = y^\dagger w_\infty^{(\mathrm{int})}(y^\dagger) \;\; , \qquad (100b)$$

where, on the other hand, $1/y^\dagger = 1/y \leq 1$ is outside the domain, and the role of the two components should be interchanged therein, according to Eq. (95c) and Eq. (95d), which makes the above result only mathematically relevant.

Turning to the special case $F_A = F_B = F$, $\Xi_A = \Xi_B = \Xi$, the last implying $(\nu_A)_{\mathrm{sel}} = (\nu_B)_{\mathrm{sel}} = \nu_{\mathrm{sel}}$, and taking, in addition, $y^\dagger_{BA} = y^\dagger_{AB} = 1$, Eqs. (95) reduce to:

$$w^{(\mathrm{int})}(\Xi, 1) = w^{(\mathrm{ext})}(\Xi, 1) = w(\Xi, 1) \qquad (101)$$

and the fractional virial potential energy, expressed by Eq. (27a), reduces to:

$$\phi = m^\dagger \frac{m^\dagger \nu_{\mathrm{sel}} - (9/8)w(\Xi,1)}{\nu_{\mathrm{sel}} - (9/8)m^\dagger w(\Xi,1)} \;\; ; \;\; y^\dagger = 1 \;\; , \quad (102a)$$

$$\nu_{\mathrm{sel}} = \frac{9}{16}\int_0^\Xi F^2(\xi)\,d\xi \;\; , \qquad (102b)$$

$$w(\Xi, 1) = \int_0^\Xi F(\xi)\frac{dF}{d\xi}\xi\,d\xi \;\; , \qquad (102c)$$

$$F(\Xi) = 0 \;\; , \qquad (102d)$$

where Eq. (102b) and Eq. (102d) follow from the definition of ν_{sel} and $F(\xi)$ respectively. For further details refer to earlier attempts (e.g. Roberts 1962, Caimmi and Secco 1992, CV08).

Integration by parts of Eq. (102c) and combining with Eq. (102b) and Eq. (102d), yields:

$$w(\Xi, 1) = -\frac{8}{9}\nu_{\mathrm{sel}} \;\; . \qquad (103)$$

Finally, substituting Eq. (103) into Eq. (102a) produces:

$$\phi = m^\dagger \;\; ; \qquad y^\dagger = 1 \;\; , \qquad (104)$$

which is a general result for subsystems with equal scaled density profiles, $F_A(\xi) = F_B(\xi) = F(\xi)$, $0 \leq \xi \leq \Xi$.

A2. DIMENSIONAL MACROGAS EQUATION OF STATE

Let macrogases be defined as large-scale collisionless fluids with the following properties: (i) Particles are identical mass points; (ii) Particle number is extremely large; (iii) Particle motions obey Newton laws of mechanics; (iv) Particle collisions are absent; (v) Particle interactions obey Newton law of gravitation.

Under the assumption of homeoidally striated density profiles, by use of Eq. (21), the virial theorem reads:

$$2E_{\mathrm{kin}} - \nu_{\mathrm{sel}}\frac{G(M^\dagger)^2}{a_1^\dagger}B = 0 \;\; . \qquad (105)$$

Let the macrovolume, V_{M}, the macropressure, p_{M}, the macrotemperature, T_{M}, and the mass weighted rms velocity, σ_{M}, be defined as:

$$V_{\mathrm{M}} = \frac{4\pi}{3}a_1 a_2 a_3 \;\; , \qquad (106)$$

$$p_{\mathrm{M}} = \frac{GM^2}{a_1^2 a_2 a_3} \;\; , \qquad (107)$$

$$kT_{\mathrm{M}} = \frac{2}{3}\frac{1}{N}E_{\mathrm{kin}} \;\; , \qquad (108)$$

$$\sigma_{\mathrm{M}} = \left(\frac{2E_{\mathrm{kin}}}{M}\right)^{1/2} \;\; , \qquad (109)$$

where N is the total number of particles, k the Boltzmann's constant, and the index M means macrogas. In particular, Eq. (108) discloses that the macrotemperature T_{M} coincides with the temperature of an ideal gas with particle number N and translational kinetic energy E_{kin}.

Typical values for galaxies are $M = 3\cdot10^{11}\mathrm{m}_\odot$, $N = 3\cdot10^{11}$, $\sigma_{\mathrm{M}} = 100\sqrt{3}\,\mathrm{km\,s}^{-1}$, which yields via Eq. (108) and Eq. (109): $kT_{\mathrm{M}} = M\sigma_{\mathrm{M}}^2/(3N) = 10^{14}\cdot1.99\cdot10^{33}\mathrm{erg} = 1.99\cdot10^{47}\mathrm{erg}$, and $T_{\mathrm{M}} = 1.99\cdot10^{47}/(1.38\cdot10^{-16})\mathrm{K} = 1.44\cdot10^{63}\mathrm{K} = 1440\,\mathrm{K}_{\mathrm{M}}$, where where $\mathrm{K}_{\mathrm{M}} = 10^{60}\mathrm{K}$ is the macrodegree, assumed as macrotemperature unit.

The combination of Eqs. (19)-(21) and Eqs. (105)-(109) yields:

$$\frac{p_{\mathrm{M}}V_{\mathrm{M}}}{NkT_{\mathrm{M}}} = 4\pi\frac{GM}{a_1\sigma_{\mathrm{M}}^2} = 4\pi\frac{(\nu_{\mathrm{mas}})^2}{\Xi\nu_{\mathrm{sel}}B} \;\; , \qquad (110)$$

which may be conceived as a compressibility factor.

In presence of a similar, similarly placed, homeoidally striated density profile, by use of Eqs. (21)-(23), the virial theorem for the subsystem under consideration reads:

$$2(E_u)_{\mathrm{kin}} - \frac{G(M_u^\dagger)^2}{(a_u^\dagger)_1}(\nu_u)_{\mathrm{sel}}\left[1 + \frac{(\nu_{uv})_{\mathrm{tid}}}{(\nu_u)_{\mathrm{sel}}}\right]B \;\; , \quad (111)$$

and the macrogas equation of state is:

$$(p_u)_{\mathrm{M}}(V_u)_{\mathrm{M}} = \frac{4\pi[(\nu_u)_{\mathrm{mas}}]^2}{\Xi_u(\nu_u)_{\mathrm{sel}}B}\left[1 + \frac{(\nu_{uv})_{\mathrm{tid}}}{(\nu_u)_{\mathrm{sel}}}\right]^{-1}$$
$$\times N_u k(T_u)_{\mathrm{M}}; \; u = i,j; \; v = j,i, \quad (112)$$

where i and j denote the inner and the outer subsystem, respectively. The compressibility factor is:

$$\frac{(p_u)_{\mathrm{M}}(V_u)_{\mathrm{M}}}{N_u k(T_u)_{\mathrm{M}}} = 4\pi\frac{GM_u}{(a_u)_1[(\sigma_u)_{\mathrm{M}}]^2}$$
$$= 4\pi\frac{[(\nu_u)_{\mathrm{mas}}]^2}{\Xi_u(\nu_u)_{\mathrm{sel}}B}\left[1 + \frac{(\nu_{uv})_{\mathrm{tid}}}{(\nu_u)_{\mathrm{sel}}}\right]^{-1};$$
$$u = i,j, \quad v = j,i, \quad (113)$$

in all cases. The effect of the tidal potential is expressed by the sum within square brakets. If the two subsystems were infinitely distant from each other, $(\nu_{uv})_{\mathrm{tid}} = 0$ and the above results reduce to their one-component counterparts.

In this view, one-component macrogases should be conceived as "ideal" and two-component macrogases as "VDW", the related equations of state resembling ideal and VDW gas equation of state, respectively. In fact, the mass ratio $m = M_j/M_i$, and the axis ratio $y = (a_j)_1/(a_i)_1 = (a_j)_2/(a_i)_2 = (a_j)_3/(a_i)_3$ appear in the explicit expression of $(\nu_{uv})_{\mathrm{tid}}$. Owing to Eqs. (106)-(107), the following relations hold:

$$\frac{(V_j)_{\mathrm{M}}}{(V_i)_{\mathrm{M}}} = \frac{(a_j)_1(a_j)_2(a_j)_3}{(a_i)_1(a_i)_2(a_i)_3} = y^3 \;, \quad (114)$$

$$\frac{(p_j)_{\mathrm{M}}}{(p_i)_{\mathrm{M}}} = \frac{(M_j)^2}{(M_i)^2}\frac{(a_i)_1^2(a_i)_2(a_i)_3}{(a_j)_1^2(a_j)_2(a_j)_3} = \frac{m^2}{y^4} \;, \quad (115)$$

$$\frac{N_j(T_j)_{\mathrm{M}}}{N_i(T_i)_{\mathrm{M}}} = \frac{(E_j)_{\mathrm{kin}}}{(E_i)_{\mathrm{kin}}} = \phi \;, \quad (116)$$

which show that the profile factor $(\nu_{uv})_{\mathrm{tid}}$ depends on the fractional macrovolume and the fractional macropressure via m and y.

The combination of Eq. (108), Eq. (112), Eq. (114), and Eq. (115) yields:

$$\frac{m^2}{y} = \frac{\Xi_i}{\Xi_j}\left[\frac{(\nu_j)_{\mathrm{mas}}}{(\nu_i)_{\mathrm{mas}}}\right]^2\frac{(\nu_i)_{\mathrm{sel}} + (\nu_{ij})_{\mathrm{tid}}}{(\nu_j)_{\mathrm{sel}} + (\nu_{ji})_{\mathrm{tid}}}\phi \;, \quad (117)$$

which, using Eqs. (25), may be cast into the equivalent form:

$$X_{\mathrm{p}}X_{\mathrm{V}}\frac{1 - \dfrac{9}{8}\dfrac{\Xi_i}{\Xi_j}\dfrac{(\nu_j)_{\mathrm{mas}}}{(\nu_i)_{\mathrm{mas}}}\dfrac{1}{(\nu_j)_{\mathrm{sel}}}\dfrac{w^{(\mathrm{int})}(X_{\mathrm{V}}, \Xi_j)}{X_{\mathrm{p}}^{1/2}X_{\mathrm{V}}^{1/3}}}{1 - \dfrac{9}{8}\dfrac{(\nu_i)_{\mathrm{mas}}}{(\nu_j)_{\mathrm{mas}}}\dfrac{1}{(\nu_i)_{\mathrm{sel}}}X_{\mathrm{p}}^{1/2}X_{\mathrm{V}}^{2/3}w^{(\mathrm{ext})}(X_{\mathrm{V}}, \Xi_j)}$$
$$= K(\Xi_i, \Xi_j)X_{\mathrm{T}} \;, \quad (118\mathrm{a})$$

$$K(\Xi_i, \Xi_j) = \frac{\Xi_i}{\Xi_j}\left[\frac{(\nu_j)_{\mathrm{mas}}}{(\nu_i)_{\mathrm{mas}}}\right]^2\frac{(\nu_i)_{\mathrm{sel}}}{(\nu_j)_{\mathrm{sel}}} \;, \quad (118\mathrm{b})$$

$$X_{\mathrm{p}} = \frac{(p_j)_{\mathrm{M}}}{(p_i)_{\mathrm{M}}} = \frac{m^2}{y^4} \;; \quad X_{\mathrm{V}} = \frac{(V_j)_{\mathrm{M}}}{(V_i)_{\mathrm{M}}} = y^3 \;;$$

$$X_{\mathrm{T}} = \frac{N_j(T_j)_{\mathrm{M}}}{N_i(T_i)_{\mathrm{M}}} = \phi \;, \quad (118\mathrm{c})$$

that is the macrogas fractional equation of state. A simpler and more intuitive choice, adopted in the text, is $X_{\mathrm{p}} = m^2$, $X_{\mathrm{V}} = 1/y$, but the connection with the fractional macropressure and fractional macrovolume is lost in this case.

ПРИНЦИП ОДГОВАРАЈУЋИХ СТАЊА ЗА ДВОКОМПОНЕНТНЕ САМОГРАВИТИРАЈУЋЕ ФЛУИДЕ

R. Caimmi

Dipartimento di Astronomia, Università di Padova
Vicolo Osservatorio 2, I-35122 Padova, Italy

E–mail: *roberto.caimmi@unipd.it*

Макрогасови су дефинисани као двокомпоненти астрономски објекти великих размера у којима подсистеми међусобно интерагују само путем гравитационе силе. Формулисана је једначина стања макрогаса, која је затим упоређена са ван дер Валсовом (ВДВ) једначином стања за обичне гасове. По аналогији, претпостављено је да се реалне макроизотермалне криве код макрогасова јављају као реалне изотермалне криве код обичних гасова, тамо где се фазни прелаз (пара-течност посматран у случају обичних и гас-звезде претпостављен у случају макрогасова) дешава дуж хоризонталне линије у равни макрозапремина-макропритисак $(OX_V X_p)$. Пресеци реалне и теоријске макроизотермалне криве (изведене на основу једначине стања) дефинишу две области једнаких површина, као у случају обичних гасова који се покоравају ВДВ једначини стања. Развијен је нумерички алгоритам за одређивање следећих тачака на одабраној теоријској макроизотермалној кривој у $(OX_V X_p)$ равни: три тачке пресека са одговарајућом реалном макроизотермалном кривом и два екстремума (по један максимум и минимум). Детаљно су проучене различите врсте макрогасова: UU, где су U профили густине равни, као један прост пример; HH, где су H профили густине дати законом Hernquist-a (1990) који задовољавајуће фитује посматране сфероидне компоненте галаксија; HN/NH, где су N профили густине дати Navarro-Frenk-White (1995, 1996, 1997) законом који задовољавајуће фитује симулиране халое сачињене од небарионске тамне материје. У зависности од тога да ли је профил густине довољно благ (UU) или довољно стрм (HH, HN/NH) јављају се различити трендови теоријске макроизотермалне криве у равни $(OX_V X_p)$. У првом случају не постоји критична макроизотермална крива испод или изнад које је тренд монотон. У другом случају постоји критична макроизотер-

мална крива, као и код ВДВ гасова, где се критична тачка може дефинисати као тачка хоризонталне инфлексије. У сваком случају, по аналогији са ВДВ гасовима, први квадрант $(OX_V X_p)$ равни може се поделити на три дела: (i) област G, где постоји само гас; (ii) област S, где постоје само звезде; (iii) област GS, где постоје и гас и звезде. Модел HH и HN/NH макрогасова примењен је на подскуп $(N = 16)$ елиптичних галаксија издвојених из скупа $(N = 25, N = 48)$ галаксија раног типа проучаваних у оквиру пројекта SAURON (Cappellari et al. 2006, 2007). Под поједностављеном претпоставком постојања универзалног односа маса два подсистема, m, разматрани су различити модели које карактеришу различити "скраћени" радијуси, односно концентрације, Ξ_i, Ξ_j, и одређени положаји објеката у $(OX_V X_p)$ равни. Очекује се да макрогасови који одговарају елиптичним галаксијама леже унутар области S или, најдаље, мало изван границе области S и GS. У складу с тим, одбачени су сви модели у којима објекти леже далеко изван области S или ван $(OX_V X_p)$ равни. За сваки макрогас разматрано је двадесет модела са различитим вредностима за параметре (Ξ_i, Ξ_j, m) где су $\Xi_i, \Xi_j = 5, 10, 20, +\infty$ (Ξ_i и Ξ_j су коначни или бесконачни) и $m = 10, 20$. Прихватљиви модели су (10, 10, 20), (10, 20, 20), (20, 10, 20), (20, 20, 20), за HH макрогасове, и (10, 5, 10), (10, 10, 20), (20, 10, 20), за HN/NH макрогасове. Типично, брзи ротатори су нађени унутар области S, док се спори ротатори налазе у близини границе (с обе стране) између области S и GS. Размотрен је и укупан ефекат неодређености посматраних величина на положај објеката у равни $(OX_V X_p)$. На крају, формулисан је принцип одговарајућих стања макрогасова са одређеним профилом густине и скалираним "скраћеним" радијусом.